





Photonic Integrated Components for Optical Coherence Tomography

Fotonische geïntegreerde componenten voor optische coherentietomografie

Günay Yurtsever

Promotor: prof. dr. ir. R. Baets

Proefschrift ingediend tot het behalen van de graad van  
Doctor in de Ingenieurswetenschappen: Elektrotechniek

Vakgroep Informatietechnologie

Voorzitter: prof. dr. ir. D. De Zutter

Faculteit Ingenieurswetenschappen en Architectuur

Academiejaar 2014 - 2015



ISBN 978-90-8578-808-9  
NUR 959, 954  
Wettelijk depot: D/2015/10.500/52

Promotor:

Prof. dr. ir. Roel Baets

Examencommissie:

Prof. dr. ir. Rik Van de Walle (voorzitter)	Universiteit Gent
Prof. dr. ir. Roel Baets (promotor)	Universiteit Gent
Prof. dr. ir. Wim Bogaerts	Universiteit Gent
Prof. dr. ir. Patrick Segers	Universiteit Gent
Dr. ir. Danae Delbeke	Universiteit Gent
Prof. dr. Ton G. van Leeuwen	Academisch Medisch Centrum Universiteit van Amsterdam
Dr. ir. Didier Beghuin	Lambda-X sa

Universiteit Gent

Faculteit Ingenieurswetenschappen en Architectuur

Vakgroep Informatietechnologie

Sint-Pietersnieuwstraat 41, B-9000 Gent, België

Tel.: +32-9-264.33.16

Fax.: +32-9-264.35.93





*To my family,*



# Acknowledgements

It must be the curiosity about how things work and the joy of learning that put me through this fun and fulfilling journey. The journey of my PhD was full of excitement, challenges and learning experiences. The interactions with professors, colleagues, friends and family have been very valuable and I would like thank you all for being with me through my journey.

I would like to start with my adviser Roel, who provided me an opportunity to do research in this world-class group. I am indebted for his trust and support to quite independently carry out my research. I learned from him how to macro manage research activities with a positive attitude. The photonics dinners in his garden and later in the botanic garden were always special evenings.

Thanks to my committee members who showed interest in my research and willingness to serve on my thesis committee despite their busy schedules; Prof. Rik Van de Walle, Prof. Roel Baets, Prof. Wim Bogaerts, Prof. Ton van Leeuwen, Prof. Patrick Segers, Dr. Danae Delbeke and Dr. Didier Beghuin.

Writing a clear thesis can only be possible with friends who would proof read carefully; Alfonso, Andrea, Andreas, Andrew, Antonio, Artur, Bendix, Daan, Herbert, Jan-Willem, Jesper, Kasper, Michael and Sören. The writing of this thesis was possible with your kind help.

Every employee wants a great working atmosphere, professors of the photonics research group have created it here; Dries for keeping the cleanroom in shape, Geert for improving the conditions of the measurement rooms and being an example of a sportsman, Gunther for showing how to be cool in all circumstances, Nicolas for demonstrating that a professor can build a setup with his students, Peter for being available for all my questions and taking us to lunches, Roel for being a terrific boss, Wim for being an example of a man of many hats and the humor engine of the group.

Fellow colleagues/friends, you made time fly very fast with your enjoyable conversations; Abdul, Adil, Alban, Ananth, Andrea, Andrew, Antonio, Ashim, Bart, Bendix, Bram, Diedrik, Francois, Geert Morren,

Jan-Willem, Jeroen, Jesper, Kasia, Manu, Michael, Muhammad, Pieter, Rodica, Rajesh, Raphaël, Rodica, Sanja, Sarvagya, Shahram, Stevan Stankovic, Thijs, Thomas, Tom, Youssef for being there.

How can you do research alone without helpful people around; Pieter for coding my first mask. Writing proper software is always a plus in science and engineering; Andrew, Antonio, Manu and Michael for helping me with programming. Mask design is a significant part in every student in the group; Amit, Youssef and Jin for all help with mask design and the submission process. Processing in the cleanroom is black magic; Steven for the first-time-right processing, Liesbet for the beautiful FIB pictures, Kasia for the photodetector and SU8 processing. Optics without custom mechanical components is unthinkable; Luc and Peter for the fine workmanship.

Administrative and IT support and organizations in the group was seamless, thanks to Bert, Dave, Ilse Van Royen, Ilse Meersman, Kristien and Mike. Each photonics day event with different social activities was memorable.

Sometimes you also need help with non-work related stuff; Liu Liu, Shahram, Sukumar for the first house move; Alban, Adil, Ananth and Karel for the second house move. When we talk about house; Geert Morren for teaching me about housing and renovation costs in Belgium.

Exercise is very important for a healthy body and mind; Yannick, Thijs, Sam, Peter De Heyn, Pieter for being motivating friends on Strava. Alban for being a swimming buddy. Shibnath and Bert for showing me that getting rid of belly fat is possible. While exercising is fun, eating is even more fun. My Introduction to Belgian Cooking 101 course buddies, I enjoyed very much cooking and eating together with you; Bart, Elewout, Eva, Koen, Marie, Shankar, Thijs. It has many benefits to be in a multi-cultural group; Andrea and Ilaria for showing us how to cook Italian pizza.

Learning and speaking Dutch in Belgium made my life easier; Andreas, Daan, Frédéric, Raphaël, Sara, Thomas for the Dutch lunches. Learning other languages is valuable; Amin and Leila for improving my Azeri Turkish vocabulary and Anton for Russian conversations.

Working together is more enjoyable than working alone; Yanlu for sharing the OCT/LDV setup, Shankar and Herbert for working together on the tapers, Andrea for giving life to my sleeping-beauty like spectrometer. I almost never worked in the lab alone in the late evenings and weekends; Aditya, Ashwyn, Bin, Hui, Linghua, Liu Liu, Pijush, Samir, Weiqiang for being in the lab during such times.

Working with industrial partners taught me to approach problems pragmatically. It was a valuable experience to work in the Art Press II project; Didier, Laurent, Koenraad and Patrick.

It is tough when you work in a niche field like optical coherence tomography (OCT); specifically if there is no one else working on the topic not only in the group, but even in Belgium. Luckily, in middle of my PhD, I met Imran who was also working on her PhD in almost the same topic at the University of Twente. Brain storming with you and sharing research experiences via Skype was very valuable.

Working on a multi-disciplinary research topic requires help from outside of the group. While trying to make ultra-small OCT imaging devices, I was always eager to have hands-on experience with state-of-the-art OCT setups. Thanks to Prof. Wolfgang Drexler from Medical University Vienna, I had an opportunity to get beautiful OCT images with my chips using an OCT setup in his lab. I had a very good time in his pioneering OCT lab thanks to Aneesh, Behrooz and Boris.

My first working chips would not be there without the waveguide technology of LioniX and their help in the design process; Arne and Marcel from LioniX and Sesilia from PhoeniX.

Demonstrating OCT images with my tiny chips was addictive and I wanted to do it one more time. I needed to do in an OCT lab with the necessary expertise and equipment. However, driving to Vienna was quite long. Luckily, Prof. Ton van Leeuwen visited our lab just on time, and let me to come to his lab to do experiments in Amsterdam. Ton for his generosity, kindness and modesty, Nicolas for his endless energy, Dirk for his interest in the grating idea, Jeroen for his excellent manuscript corrections.

I also enjoyed seeing research ideas from the group transforming into products and prove to taxpayers that their money goes back to the economy. Dirk, Jonathan, Joost and William for their success with Caliopa; Joris, Martin, Pierre, Pieter and Wim for starting Luceda Photonics. Danae and Bart Geers for enthusiastically looking for new applications of our research.

You learn a lot from your advisor. However, being an advisor also teaches you a lot; Navin, Mathieu and Semere working for your master theses with me.

No matter how fun research is, without socializing it may not be sustainable. Peter Vandersteegen for taking us to have a cup of chocolate or ice cream. Elewout, Cristina, Wout, Marie, Pauline, Karel and Kristof for organizing the best goodbye presents. Ashim and Jesper for showing

me cool dans moves. Roel for taking us to Vooruit after group meetings. CMST buddies Aykut, Pankaj and Jelle for fun lunchtime conversations.

Smiling is infectious, you catch it like the flu; Abdoulghafar, Alfonso, Amin, Ashim, Cristina, Chen, Khai, Lieven, Jan-Willem, Joris Roels, Nannicha, Parastesh, Sanja, Shahram and Yannick for having big smiley faces.

If you have kids, you always want to talk about them and ask other parents for their stories; Liesbet for teaching me the "kabouters" trick, Bendix for sharing the stories of our children.

It takes time to get used to living in another country. There comes help from friends from your homeland and their partners; Aykut, Nursen, Esra, Pieter, Erkin, Kerem, Katelijne, Onur, Daria, Tayfun, Irmak, Murat and Özcan for your friendship and creating a small Turkey in Belgium.

However, my journey did not start in Gent. With a Star Wars like maneuver, I would like to go the beginning of my graduate studies; to Drexel University in Philadelphia. Prof. Banu Onaral for proving me the opportunity to start doing research, and your mother-like care of your team. Prof. Kambiz Pourrezaei for being a friend-like co-advisor and ability to generate proposal ideas from almost everything. Prof. Ata Akin giving me the opportunity to do internship there and the supervision in the first months. The Turkish graduate student community made life there so much fun. Alper, Hasan, Kurtuluş and Meltem for the fun research together; Ali Bulman, Ali Vedat, Burak, Murat and Serkan for Friday evening gatherings around 2nd and Market Streets. Evren, Esra and Gül for being the best house-mates, I felt very lucky to live together with you. Evren, for surviving the flipping over of our row-boat in Schuylkill River in December.

My next destination was University of Pennsylvania; Prof. Britton Change for being an extra-ordinary scientist and the unforgettable sailings in Barnegat and Florida Bays. Is there an another science professor with an olympic gold medal? Your memory will always be with me. Shoko for the delicious Japanese food and hospitality. Prof. Warren Warren for providing me the opportunity to do cutting-edge research in a state-of-the-art lab and every time immediately understanding what I mean. Tong for teaching me all practical things about optics and support. Martin for demonstrating research with German discipline and effectiveness.

I was destined to travel. When Warren Lab decided to move to Duke University, American friends said to me that life is better in the south.

Indeed, living in the sunny North Carolina was fantastic. Students joining from Warren's Princeton Lab made me a member of bigger research family. Henry for sharing an apartment in our heavenly community, Dan for having feasts at different restaurants, Chunqiang for his wise advices, Thomas for teaching me biochemistry, Ivan for finalizing the hole refilling experiment. Kathy for all the house parties and the delicious food. Duke also had a large Turkish graduate student community, which made me feel home. Oğuz and Mahmut for sharing your apartment and the delicious cooking. Abdullah, Murat, Erdem, Ergün, and Tolga for your friendship.

Having friends with whom you never loose contact is priceless. Erhan, Koray, Umut Akdemir, Umut Demirçin, Serdar, Sinan, Tolga and Yakup thanks for your support and the re-unions. Alpay, Alper, Barış, Emre, Semra, Ulaş for always keeping in touch.

In Belgium, I did not feel like I was away from my family as I am lucky have a warm-hearted family-in-law here. Sevgili Zehra anne, Kasım baba, Hüseyin ve Tuğba, sizlerle Beçika'da kendimi evimde hissediyorum, sevginiz ve hep yanımda olduğunuz için teşekkürler.

I am indebted to my mom and dad for their never ending love. They did their best to provide good education for their children. I would not have had the same interest for learning if I was born in another family. I am also lucky to have a brother like Güner, who have been always supportive of me. Sevgili annem ve babam, bu kadar çok okuyup, öğrenmem sizin sayenizdedir, sonsuz sevginiz ve beni böyle yetiştirdiğiniz için size minnettarım.

I was lucky to have farmer grandparents, thanks to whom I grew up in nature. My grandparents Ahmet and Sadriye, Ibrahim and Fatma for taking care of me during summer vacations and letting me experience the simple and beautiful rural life.

For me happy life comes trough a happy family. My lovely wife Ayla and my sweet daughters Aylin and Nilay, you are the joy of my life. I have been blessed to meet my wife Ayla 12 years ago under the Eiffel Tower and have two lovely daughters together. Your unconditional love and support has been indispensable through all these years. With your companionship life is more fulfilling and enjoyable. I know that with trust and love, we will stand beside each other through both wonderful and difficult times. My precious daughters Aylin and Nilay, seeing you smile, grow and learn has been so joyful. Our love towards you is endless and we hope to raise you curious with hunger to learn.

*Günay Yurtsever*  
*Gent, June 2015*

## Table of Contents

<b>Acknowledgements</b>	<b>iii</b>
<b>Nederlandse samenvatting</b>	<b>xxiii</b>
<b>English summary</b>	<b>xxxiii</b>
<b>1 Introduction</b>	<b>1</b>
1.1 Optical coherence tomography and its applications . . . . .	2
1.2 Types of OCT implementations . . . . .	6
1.2.1 Time-domain OCT . . . . .	6
1.2.2 Full-field OCT . . . . .	9
1.2.3 Fourier-domain OCT . . . . .	10
1.3 Developments in FD-OCT . . . . .	15
1.3.1 Developments in spectral-domain OCT . . . . .	15
1.3.2 Developments in swept-source OCT . . . . .	16
1.3.3 Alternative developments in high speed FD-OCT . . . . .	18
1.4 Miniaturization of OCT . . . . .	19
1.4.1 MEMS for OCT . . . . .	19
1.4.2 Integrated photonics for OCT . . . . .	21
1.4.3 Companies commercializing integrated photonics for OCT . . . . .	22
1.5 Challenges and outline . . . . .	24
1.6 Publications . . . . .	26
<b>2 Theory of optical coherence tomography</b>	<b>37</b>
2.1 Fourier-domain OCT . . . . .	37
2.2 Resolution . . . . .	43
2.3 Imaging range . . . . .	45
2.4 Sensitivity . . . . .	46
2.5 Linear sampling in k-space . . . . .	48
2.6 Signal fall-off . . . . .	49
2.7 Dispersion . . . . .	50
2.8 Conclusion . . . . .	53
<b>3 Ultra-compact silicon photonic integrated interferometer with an on-chip reference arm for swept-source optical coherence tomography</b>	<b>59</b>
3.1 Integrated photonics and miniaturization of OCT . . . . .	60

3.2	Silicon photonics . . . . .	62
3.2.1	Fabrication of waveguides . . . . .	63
3.2.2	Basic integrated photonic components in SOI . . . . .	65
3.3	Design of the photonic integrated interferometer and the SS-OCT setup . . . . .	69
3.3.1	Waveguide design . . . . .	70
3.3.2	Adiabatic coupler design . . . . .	71
3.3.3	The SS-OCT system with the integrated interferometer . . . . .	73
3.4	Axial resolution and sensitivity characterization . . . . .	75
3.5	OCT imaging of tissue phantom . . . . .	78
3.6	Discussion . . . . .	79
<b>4</b>	<b>Si<sub>3</sub>N<sub>4</sub>/SiO<sub>2</sub> photonic integrated interferometer with an on-chip reference arm for spectral-domain optical coherence tomography</b>	<b>87</b>
4.1	Design of the photonic integrated circuit and the OCT setup . . . . .	88
4.1.1	Waveguide design . . . . .	88
4.1.2	The OCT setup with the photonic integrated interferometer . . . . .	93
4.2	Device characterization and <i>in vivo</i> human skin imaging . . . . .	96
4.2.1	Axial resolution and sensitivity . . . . .	96
4.2.2	<i>In vivo</i> human finger skin imaging . . . . .	98
4.3	Discussion . . . . .	100
4.4	Conclusion . . . . .	103
<b>5</b>	<b>Integrated spectrometer based on cascaded ring resonators and arrayed waveguide gratings</b>	<b>107</b>
5.1	Introduction . . . . .	108
5.1.1	AWG . . . . .	108
5.1.2	Ring resonator . . . . .	110
5.1.3	Cascaded spectrometers . . . . .	111
5.2	Design . . . . .	113
5.3	Fabrication and characterization . . . . .	116
5.3.1	Fabrication . . . . .	116
5.3.2	Characterization . . . . .	116
5.4	Discussion . . . . .	122
5.5	Conclusion . . . . .	122
<b>6</b>	<b>Conclusions and perspectives</b>	<b>129</b>

---

6.1	Conclusions . . . . .	129
6.2	Perspectives . . . . .	132
<b>A</b>	<b>Appendix A</b>	<b>139</b>
<b>B</b>	<b>Appendix B</b>	<b>145</b>



## List of Figures

1.1	Penetration depth and resolution of prevailing imaging modalities. . . . .	3
1.2	Commercial OCT devices and OCT images. . . . .	5
1.3	3D and 2D cross-sectional OCT images of an LCD panel with defects. . . . .	6
1.4	Schematic diagram of time-domain OCT. . . . .	7
1.5	Illustration of TD-OCT signal for a sample with two discrete-reflectors. . . . .	8
1.6	Generation of cross-sectional and volumetric OCT images. . . . .	8
1.7	Schematic diagram of full-field OCT. . . . .	9
1.8	Schematic diagram of Fourier-domain OCTs. . . . .	11
1.9	Illustration of FD-OCT signal for a sample with two discrete-reflectors. . . . .	13
1.10	Imaging depth and bandwidth required for the OCT light-source to maintain a resolution of $10\ \mu\text{m}$ as a function of wavelength . . . . .	15
1.11	Comparison of cross-sectional <i>in vivo</i> human retina OCT images. . . . .	17
1.12	NITID imaging device for dermatology, from DermaLumics. . . . .	23
1.13	OCTANE-860 spectrometer from Tornado Spectral Systems. . . . .	24
2.1	Schematic diagram of spectral-domain OCT . . . . .	38
2.2	Diagram of the sample and reference arms. . . . .	39
2.3	Dependence of axial resolution in OCT on light source bandwidth. . . . .	45
2.4	Imaging range in FD-OCT as a function of sampling period in wavelength. . . . .	47
2.5	Measuring sensitivity in an OCT system. . . . .	48
2.6	Effect of $2^{\text{nd}}$ order dispersion mismatch in OCT. . . . .	52
3.1	Patterning of a substrate using projection photolithography. . . . .	64
3.2	Fabrication process overview of a waveguide in SOI. . . . .	64
3.3	Cross-sectional view of SOI processes offered by ePIXfab passive components runs. . . . .	65
3.4	Mode profiles of the fundamental TE modes of SOI waveguides at $1300\ \text{nm}$ . . . . .	66
3.5	Mode evolutions in directional and adiabatic couplers. . . . .	68

3.6	Illustration of a grating coupler. . . . .	69
3.7	Effective refractive index as a function of waveguide width for a SiO <sub>2</sub> clad SOI waveguide at 1265 nm. . . . .	70
3.8	Simulation of GVD for shallow-etched rib waveguide for different waveguide widths at 1312 nm. . . . .	71
3.9	SEM image of the fabricated adiabatic coupler. . . . .	72
3.10	Simulation of mode propagation in the straight section of the 2 × 2 adiabatic coupler. . . . .	72
3.11	The SS-OCT setup with the chip. . . . .	74
3.12	Measured and simulated coupling ratios of the adiabatic coupler. . . . .	75
3.13	The interference fringe and its Fourier transform with and without dispersion compensation. . . . .	77
3.14	Photograph of the layered tissue phantom. . . . .	78
3.15	OCT cross-sectional image (average of 100 B-scans) of a layered tissue phantom . . . . .	79
4.1	Illustration of a box shaped Si <sub>3</sub> N <sub>4</sub> waveguide embedded in SiO <sub>2</sub> on Si-carrier. . . . .	88
4.2	Process flow (cross-section) of the box-shaped TriPlex™ waveguides. . . . .	89
4.3	Calculated effective indices of the TE and TM modes of a box waveguide versus waveguide width at 1250 nm. . . . .	91
4.4	Scanning electron microscope image of Si <sub>3</sub> N <sub>4</sub> waveguide cross-section. . . . .	91
4.5	Simulated TE <sub>00</sub> and TM <sub>00</sub> modes electric field profiles. . . . .	92
4.6	Screenshot of the mask used to fabricate the interferometer and a microscope image of a y-splitter that is used in the interferometer. . . . .	93
4.7	The OCT setup with the integrated interferometer chip . . . . .	94
4.8	OCT cross section (sum projection of 100 B-scans) of a fingertip. . . . .	99
4.9	OCT cross-section (sum projection of 28 B-scans) and en-face views of a finger midjoint. . . . .	99
4.10	Simulation of GVD for fundamental TE and TM modes with respect to change in Si <sub>3</sub> N <sub>4</sub> layer thickness. . . . .	101
5.1	Illustration of an AWG. . . . .	109
5.2	Illustration of a ring resonator. . . . .	111
5.3	Figures from the spectrometer study by Kyotoku et al. . . . .	112

---

5.4	Schematic of the spectrometer consisting of 13 cascaded ring resonators and 13 AWGs. . . . .	114
5.5	Simulated transmission spectra of an individual ring resonator and a 16 channel AWG. . . . .	114
5.6	A microscope image of the fabricated spectrometer. . . . .	117
5.7	Measured transmission spectra of a ring resonator and an AWG test structures. . . . .	118
5.8	Spectrometer measurement set-up. . . . .	119
5.9	Ring resonator global pass-port response. . . . .	120
5.10	Superposition of 208 transmission spectra of the spectrometer. . . . .	121



# List of Tables

1.1	MEMS-based swept-source lasers . . . . .	20
3.1	Sensitivities and losses related to the integrated OCT with silicon waveguides. . . . .	78
4.1	Sensitivities and losses related to the integrated OCT with Si <sub>3</sub> N <sub>4</sub> waveguides. . . . .	97



# List of Acronyms

## **0-9**

2D	Two dimensional
3D	Three dimensional

## **A**

AC	Autocorrelation
ADC	Analog to digital converter
AWG	Arrayed waveguide grating

## **C**

CCD	Charge-coupled device
CMOS	Complementary metal oxide semiconductor
CT	Computed tomography

## **D**

DC	Direct current
----	----------------

**E**

EIC                      Electronic integrated circuit

**F**

FD-OCT                Fourier-domain optical coherence tomography  
FSR                      Free spectral range  
FWHM                  Full width at half maximum

**L**

LPCVD                 Low-pressure chemical vapor deposition

**M**

MEMS                  Micro-electromechanical system  
MPW                    Multi-project wafer  
MRI                     Magnetic resonance imaging  
MZI                     Mach-Zehnder Interferometer

**O**

OD                      Optical density  
OCT                     Optical coherence tomography

**P**

PIC                     Photonic integrated circuit

---

PECVD                      Plasma-enhanced chemical vapor deposition

**S**

SD-OCT                    Spectral-domain optical coherence tomography  
SEM                        Scanning electron microscope  
SLED                       Superluminescent light emitting diode  
SMF                        Single-mode fiber  
SNR                        Signal-to-noise ratio  
SOI                         Silicon-on-insulator  
SS-OCT                    Swept-source optical coherence tomography

**T**

TE                         Transverse electric  
TM                         Transverse magnetic

**U**

UV                         Ultraviolet

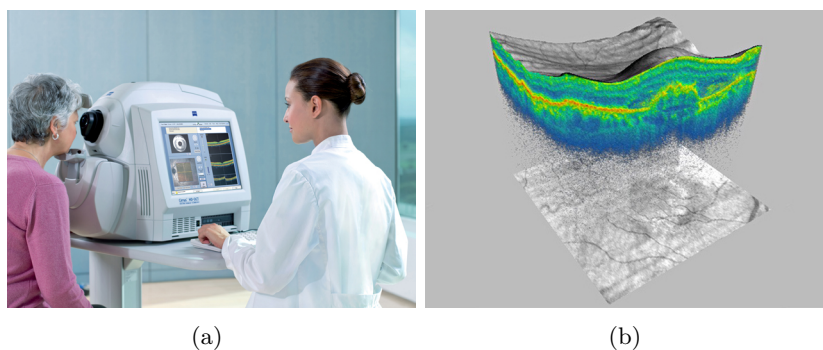


# Nederlandse samenvatting

Medische beeldvormingstechnieken spelen een cruciale rol in de gezondheidszorg. Optische coherentie-tomografie (OCT) is een relatief recente medische beeldvormingstechniek die dwarsdoorsnede beelden van weefsel kan maken. OCT wordt hoofdzakelijk gebruikt in de oogheelkunde voor retinale beeldvorming. Deze nuttige technologie kan breder worden ingezet in kleine klinische centra en in ontwikkelingslanden als de huidige prijs ( $> \text{€}50.000$ ) verder zou dalen. Met kosteneffectieve waferschaal productietechnieken, kunnen optische onderdelen in OCT geïntegreerd worden op een enkel substraat, om zo de prijs aanzienlijk te verminderen. In het kader van dit proefschrift, werden fotonisch geïntegreerde interferometers voor OCT ontworpen en gefabriceerd. Door het gebruiken van deze interferometers, samen met externe lichtbronnen en detectoren, waren we in staat OCT beelden van een weefselfantoom (een object dat optische eigenschappen van weefsel heeft) en *in vivo* menselijke huid te verkrijgen. Hieronder geven we een kort overzicht van het werk in dit proefschrift.

OCT is een niet-invasieve optische beeldvormingstechnologie die onderhuidse beelden van biologisch weefsel kan maken in zowel twee als drie dimensies. OCT wordt veel gebruikt in de oogheelkunde, waarbij structurele beelden worden bekomen van de retinale lagen die niet kunnen worden verkregen door een andere beeldvormende methode. OCT is ook veelbelovend bij een groot aantal andere medische toepassingen, variërend van screening en diagnose van huidziekten, tot hulp bij chirurgische ingrepen.

OCT is vergelijkbaar met echografie, maar er wordt licht gebruikt in plaats van geluid. Het licht is gericht op de patiënt, het teruggekaatste licht wordt opgevangen door het optische systeem en een afbeelding wordt geproduceerd om de interne structuur van het weefsel te visualiseren. Met OCT kan men beelden in hogere resolutie maken dan met echografie. Anderzijds, kan men met echografie dieper doordringen in het weefsel, waardoor echografie kan gebruikt worden om de diepere



**Figuur 1:** Gebruik van OCT in oogheelkunde. a) Retina van een patiënt gescand met een commerciële OCT (Zeiss Cirrus HD-OCT). b) 3D OCT beeld van een retina ( $6\text{ mm} \times 6\text{ mm}$ ).

structuur van het weefsel te visualiseren tegenover OCT.

Een OCT systeem is een interferometer die een referentiearm en een objectarm heeft. De objectarm stuurt het licht naar het weefsel en verzamelt het teruggekaatste licht uit het weefsel. Het teruggekaatste licht wordt gecombineerd met het licht van de referentiearm en het interferentie signaal wordt omgezet in een elektrisch signaal met een fotodetector. Door het scannen van de lichtstraal over het weefsel worden 2D dwarsdoorsnede en 3D volumetrische beelden verkregen. Een commerciële OCT voor retinale beeldvorming en 3D OCT beelden van de retina worden getoond in Figuur 1.

Huidige OCT's worden geïmplementeerd als Fourierdomein OCT (FD-OCT). In FD-OCT wordt voor elke positie van de gescande lichtstraal het spectrum van de interferentie gemeten en de Fouriertransformatie berekend om een dieptescan (A-scan) te verkrijgen. Vervolgens worden alle scans gecombineerd om een 2D dwarsdoorsnede of 3D volumetrische afbeeldingen te maken. Een FD-OCT systeem kan op twee manieren worden uitgevoerd: 1) Spectraaldomein OCT (SD-OCT) - via een breedbandige lichtbron en een spectrometer bij de detectie arm. 2) Swept-source OCT (SS-OCT) - met behulp van een afstembare laser met een breed afstembereik en een fotodetector in de detectie arm.

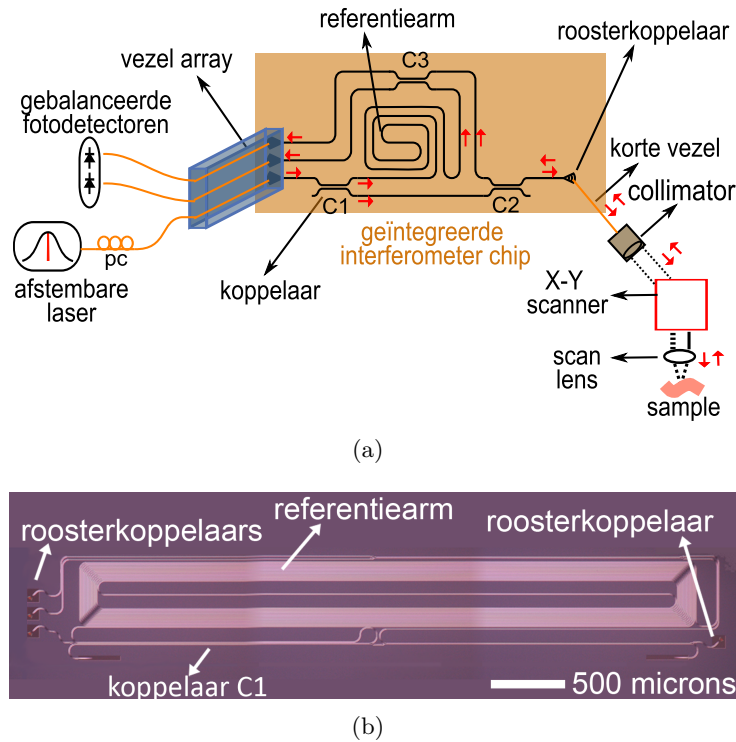
Hoewel OCT in veel ziekenhuizen over de hele wereld wordt gebruikt, zijn de kosten en complexiteit nog steeds onbetaalbaar voor brede toepassing in bestaande en nieuwe gebieden. Huidige implementaties van OCT systemen worden vaak gemaakt op basis van glasvezel en discrete

optische componenten. Fotonische integratie van discrete optische componenten op wafer-niveau heeft aangetoond voordelig te zijn wat betreft kosten, omvang, stabiliteit en energie-efficiëntie voor optische netwerktechnologie. Beeldvormingstechnieken zoals OCT zouden ook kunnen profiteren van een dergelijke fotonische integratie.

Fotonische geïntegreerde schakelingen (PIC; van het Engelse photonic integrated circuit) zijn analoog aan elektronische geïntegreerde schakelingen (EIC; van het Engelse electronic integrated circuit) zodat ook hier meerdere functies op een enkel monolithisch substraat uitgevoerd kunnen worden. De fabricage methoden van PICs zijn vergelijkbaar met EIC's, waarbij componenten worden gevormd op een wafer met lithografie. Deze patronen worden verder geëtst, gedeponerd of gewijzigd door diffusie of dopering. Het basiselement van geïntegreerde fotonica is de golfgeleider. Overige componenten zijn meestal gebouwd door de invoering van wijzigingen in eenvoudige golfgeleiderstructuur zoals het veranderen van de geometrie en het wijzigen of actief manipuleren van de fysische eigenschappen van de golfgeleider. Fotonische geïntegreerde componenten zoals splitters, filters, modulators, versterkers, lasers en fotodetectoren zijn reeds gedemonstreerd in verschillende materiaalsystemen.

In dit proefschrift hebben we onderzocht hoe OCT systemen kunnen profiteren van fotonische integratie. In het bijzonder hebben we ons gericht op het aantonen van de haalbaarheid van geïntegreerde fotonische interferometers voor OCT met on-chip referentiearmen. We evalueerden twee materiaalplatformen: 1)  $\text{Si}_3\text{N}_4$  en  $\text{SiO}_2$  golfgeleidertechnologie, genaamd TriPleX<sup>TM</sup> platform, ontwikkeld door LioniX BV (Enschede, Nederland). 2) silicium-op-isolator (SOI) met 220 nm dik silicium, bovenop 2  $\mu\text{m}$  dikke oxide. Naast de interferometers onderzochten we een spectrometerarchitectuur gebaseerd op meerdere beklede arrayed waveguide gratings (AWGs) en ringresonatoren op SOI.

Met behulp van SOI golfgeleiders, hebben we een geïntegreerde interferometer gefabriceerd voor SS-OCT. Dankzij hoog indexcontrast golfgeleiders, zorgt SOI voor hoge optische opsluiting en verminderde bochtstralen die kleinere PIC's mogelijk maken. De voetafdruk van onze geïntegreerde interferometer is slechts 5 mm  $\times$  0.75 mm. Het OCT systeem met de chip wordt in Figuur 2a getoond. Het ontwerp bestaat uit golfgeleiders, splitters, een referentiearm met een fysieke lengte van 13 cm (50.44 cm optische lengte) en roosterkoppelaars. De roosterkoppelaars worden gebruikt om het licht in en uit de chip te koppelen. Het geïntegreerde fotonische circuit werd gebruikt als interferometer van een



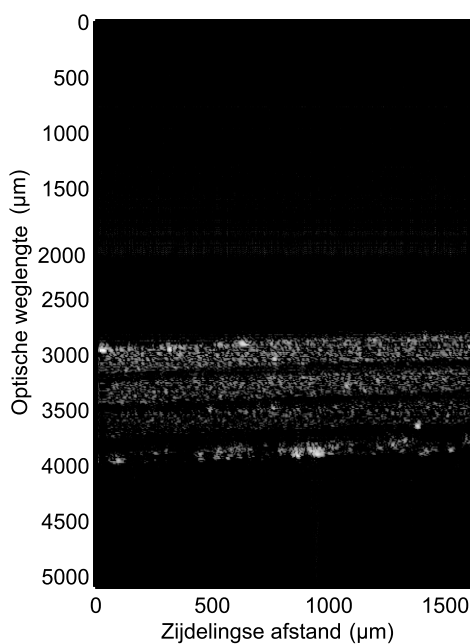
**Figuur 2:** (a) Illustratie van de SS-OCT setup met de silicium fotonische geïntegreerde interferometer, PC: polarisatie controller, C1, C2, C3:  $2 \times 2$  koppelaars. De richting van het licht wordt aangegeven met rode pijlen. (b) Microscopiebeeld van de gefabriceerde fotonische geïntegreerde interferometer.

SS-OCT systeem.

Licht uit een afstembare laser, gecentreerd bij 1312 nm, is in de chip gekoppeld met een vezel array. Koppeling in en uit de chip wordt bereikt met gekantelde roosterkoppelaars met verminderde terug-reflectie, die toegang geven tot golfgeleiders door verticale koppeling. Het input licht is TE-gepolariseerd, aangezien de roosterkoppelaar gemaakt is voor TE-licht. Na het invoeren van de chip, wordt het licht gesplitst in referentie- en objectarmen via koppelaar C1. In de objectarm wordt het licht weer gesplitst door koppelaar C2 en uit de chip gestuurd met een roosterkoppelaar. Het licht dat de chip verlaat is gekoppeld met een korte vezel waaraan een collimator is bevestigd. Het licht van de collimator gaat naar een X-Y galvanometer scanner met een scan lens. Teruggekaatst licht in de objectarm komt terug naar de chip en wordt gecombineerd

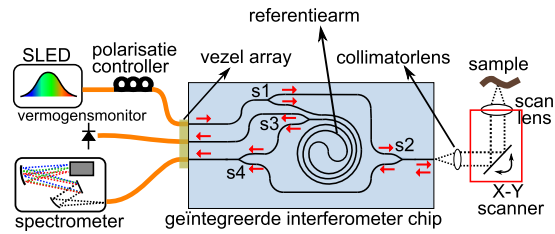
met het licht van de referentiearm koppelaar C3. Het licht aan beide uitgang-armen van koppelaar C3 verlaat de chip via roosterkoppelaars. Deze sturen het licht via een vezel array naar gebalanceerde fotodetectoren. Een microscoopbeeld van de gefabriceerde chip wordt gegeven in Figuur 2b.

De axiale resolutie van het systeem is beperkt door de bandbreedte van de roosterkoppelaars (3 dB bandbreedte: 45 nm). Na de 3e orde dispersiecompensatie in software verkregen we 25.5  $\mu\text{m}$  axiale resolutie, terwijl de theoretische resolutie 24.4  $\mu\text{m}$  is. De gevoeligheid van het systeem wordt gemeten als 62 dB met 115  $\mu\text{W}$  op het sample. Met deze opstelling hebben we een OCT beeld van een gelaagd weefselfantoom aangetoond, zoals weergegeven in Figuur 3.

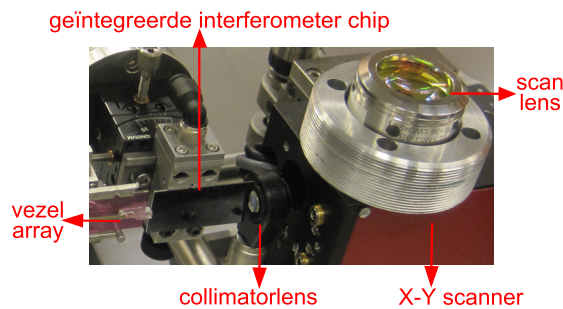


**Figuur 3:** OCT doorsnede (gemiddeld 100 B-scans) van een gelaagd weefselfantoom.

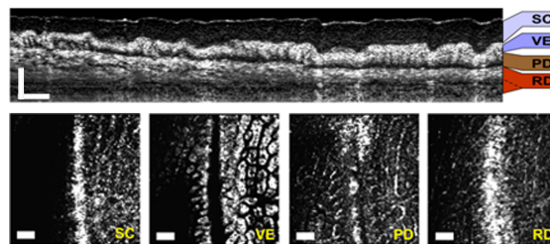
We demonstreerden ook een soortgelijke fotonische geïntegreerde interferometer voor SD-OCT met behulp van TriPleX<sup>TM</sup> golfgeleiders. Een diagram van de OCT opstelling met de geïntegreerde optische schakeling is weergegeven in 4a. De interferometer chip bestaat uit golfgeleiders, vier splitters en een 190 mm lange referentiearm met een voetafdruk van 10 mm  $\times$  33 mm. Het wordt gebruikt als de kern van een



(a)



(b)



(c)

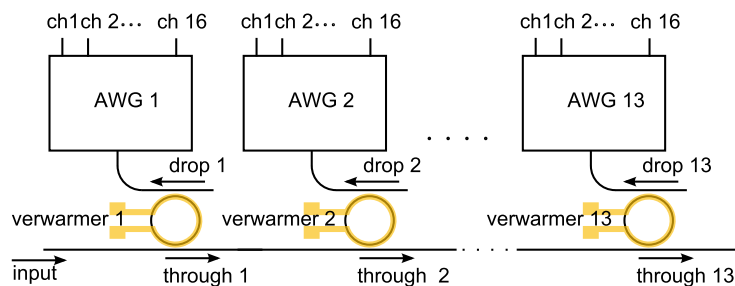
**Figuur 4:** a) Schematisch ontwerp van de OCT met de geïntegreerde interferometer chip. De richting van het licht wordt aangegeven met rode pijlen. b) Afbeelding van de setup, waarbij de vezel array, de geïntegreerde interferometer chip en de scanlens worden geïllustreerd. c) *In vivo*, OCT doorsnede en een *en-face* uitzicht (bovenaanzicht) van het middengewricht van de menselijke vinger. De schaal van het dwarsdoorsnede beeld komt overeen met  $500\ \mu\text{m}$  lengte, terwijl de schaal van de *en-face* beelden overeenkomen met een lengte van  $1\ \text{mm}$ . SC: stratum corneum, VE: levende epidermis (viable epidermis), PD: papillaire dermis, RD: reticulaire dermis.

SD-OCT, bestaande uit een superluminescente diode (SLED), gecentreerd bij  $1320\ \text{nm}$  met  $100\ \text{nm}$  bandbreedte, een spectrometer met  $1024$

kanalen en een x-y scanner. In dit systeem wordt licht van de SLED butt-gekoppeld met de geïntegreerde interferometer; een deel van het licht gericht op de on-chip referentiearm en een deel van het licht uit de chip via de objectarm naar een galvanometrische x-y scanner. Het licht dat terugkeert van de referentie- en de objectarmen wordt samengebracht en verzonden naar de spectrometer. Een foto van de opstelling is weergegeven in Figuur 4b.

We karakteriseerden de axiale resolutie en de gevoeligheid van het systeem door het meten van de reflectie van een spiegel. De gemeten axiale resolutie van het systeem was  $12\ \mu\text{m}$ , welke dicht bij de theoretische resolutie van  $10\ \mu\text{m}$  is. Om een dergelijke resolutie te bereiken, was een 10de orde dispersiecorrectie in de software nodig. De gevoeligheid van het systeem werd gemeten bij  $0.25\ \text{mm}$  diepte als  $65\ \text{dB}$  met  $0.1\ \text{mW}$  op het sample. Om het systeem te evalueren, hebben we het midden-gewricht van een menselijke vinger in vivo afgebeeld. Dwarsdoorsnede en *en-face* zicht OCT beelden, verkregen uit de vinger, zijn weergegeven in Figuur 4c. Verschillende lagen van de huid, zoals het stratum corneum (SC), levende epidermis (VE), papillaire dermis (PD) en reticulaire dermis (RD) kunnen worden onderscheiden in het beeld.

De bovenstaande resultaten zijn de eerste OCT beelden met behulp van een geïntegreerde interferometer met een on-chip referentiearm, die voldoende lang zijn voor een geslaagde x-y scanner. Deze studies zijn bemoedigend voor een on-chip OCT. De gevoeligheid in beide systemen met fotonische geïntegreerde interferometers kan verder worden verbeterd door het verlies aan de koppeling tussen vezels en chip te verminderen. Door het gebruik van een efficiëntere koppeling met geoptimaliseerde spotafmeting-converters kan de gevoeligheid van de on-chip

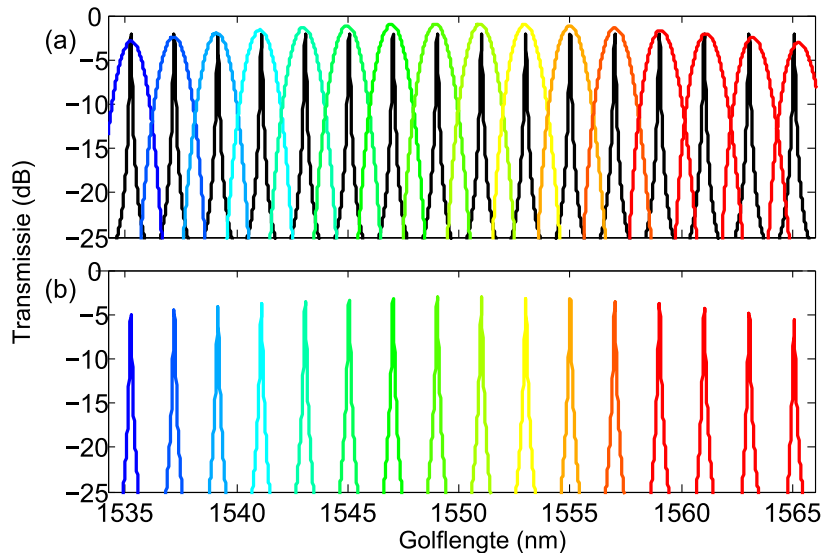


**Figuur 5:** Schema van de spectrometer die bestaan uit 13 cascade paren ringresonator en AWG, ch: kanaal.

OCT's teruggebracht worden tot het niveau ( $> 80$  dB) dat wordt verkregen met op glasvezel gebaseerde OCT systemen.

Naast de interferometers onderzochten we de mogelijkheden voor hoge resolutie, multi-channel spectrometers op SOI. Dergelijke spectrometers kunnen mogelijk worden gebruikt in SD-OCT-systemen. Met behulp van enkel AWGs of vlakke concave roosters is het fabriceren van sub-nanometer resolutie spectrometers met een groot aantal kanalen op SOI uitdagend, door aan fabricage gerelateerde fasefouten. Om deze beperking te overwinnen onderzochten we een spectrometerarchitectuur, gebaseerd op cascade AWGs en ringresonatoren. Een illustratie van de voorgestelde spectrometer wordt gegeven in Figuur 5. De spectrometer bestaat uit 13 AWG en 13 ringresonator paren. Voor elke AWG is er een ringresonator die werkt als voorfilter. Elke AWG heeft 16 kanalen en deze configuratie resulteert in een totaal van 208 ( $13 \times 16$ ) kanalen.

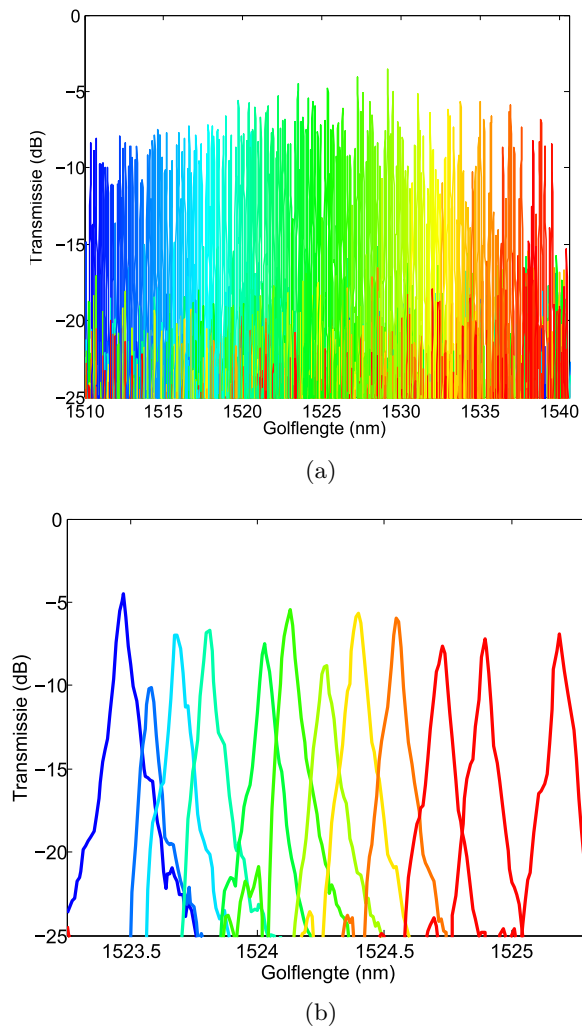
Als we kijken naar een AWG-ringresonator paar in Figuur 5; de ringresonator pre-filtert het licht en uit de droppoort stuurt een kamachtig spectrum naar de AWG. Als de kanaalscheiding van de AWG's en de ringresonatoren' vrije spectrale bereik (FSR; van het Engelse free spectral range)) op elkaar zijn afgestemd, zal elk AWG kanaal een piek van de kam bevatten. Gesimuleerde transmissiespectra van een AWG en



**Figuur 6:** a) Transmissiespectra van een individuele AWG en ringresonator. b) Transmissiespectrum van een cascade AWG en ringresonator.

een ringresonator worden gegeven in Figuur 6a, de AWG kanalen worden gegeven in kleur, de ringresonatortransmissie in het zwart. De FSR van de ringresonator komt overeen met de kanaalscheiding van de AWG. Het gecombineerde transmissiespectrum van een cascade ringresonator en een AWG is gegeven in Figuur 6b.

In ons ontwerp is de kanaalscheiding van elke AWG 1.95 nm. De FSR van de ringresonatoren is aangepast aan de kanaalafstand van de AWGs



**Figuur 7:** a) Transmissiespectrum van de 208 kanaal spectrometer. (b) Transmissiespectrum van het midden van de kanalen om meer details te zien.

en is ook 1.95 nm. De resonantiepieken van de ringresonatoren zijn thermisch afgestemd, met behulp van metalen verwarmers, gefabriceerd op de ringresonatoren. De thermische tuning wordt zodanig aangepast dat de kam van een ringresonator enigszins verschoven is ten opzichte van de kam der voorgaande ringresonator. Met deze parameters krijgen we met  $1,95/13 = 0.15$  nm spectrometer kanaalscheiding. De halfwaardebreedte (FWHM; van het Engelse full width at half maximum) van de ringresonator pieken is 0.06 nm.

Door thermische tuning van de ringresonatoren, stellen we het transmissiespectrum in op de spectrometer. Figuur 7a toont de transmissiespectra voor alle kanalen. De transmissie is genormaliseerd voor fiber-to-chip koppelingsverliezen. In Figuur 7b, zijn de centrale kanalen afzonderlijk weergegeven om meer details te zien.

In dit proefschrift onderzochten we passieve geïntegreerde fotonische componenten voor OCT. Voor de eerste keer toonden we afbeeldingen van de menselijke huid en weefselfantoom met OCT met geïntegreerde interferometers met on-chip lange referentiearmen. Om door te gaan met meer complexe fotonische geïntegreerde schakelingen voor OCT is optimalisatie nodig betreffende de verliezen van vezels-chip koppeling. We toonden ook de resultaten van het gebruik van een hoge-resolutie, multi-channel spectrometer op SOI. Verdere optimalisatie van de fabricagetoleranties moet ultracompacte spectrometers mogelijk maken. Verder onderzoek naar integratietechnieken van actieve componenten zoals lichtbronnen en detectoren, bovenop passieve structuren, vergelijkbaar met demonstraties in dit proefschrift, kan een weg openen naar volledig geïntegreerde OCT systemen.

# English summary

Medical imaging methods have a crucial role in health care. Optical coherence tomography (OCT) is a relatively recent medical imaging modality which is capable of providing cross-sectional images of tissue. It is mainly used in ophthalmology to image the retina. This useful technology can be more widely deployed in small clinical centers and developing countries if its current price (  $> \text{€}50.000$  ) can be further reduced. Using cost effective, wafer-scale microfabrication techniques, similar to the ones used in integrated electronics industry, optical components used in OCT may also be integrated on a single substrate to significantly decrease its price. In the scope of this thesis, photonic integrated interferometers for OCT were designed and fabricated. Using these interferometers together with external light sources and detectors, we were able to obtain OCT images of a tissue phantom (an object with optical properties of tissue) and *in vivo* human skin. Below, we provide a brief summary of the work done in this thesis.

OCT is a non-invasive optical imaging modality that can acquire subsurface images of biological samples in both two and three dimensions. OCT is being widely used in ophthalmology, where it provides structural images of the retinal layers that cannot be obtained by any other imaging method. OCT promises to have a powerful impact on many other medical applications ranging from screening and diagnosis of skin diseases to providing guidance in surgical operations.

OCT is very similar to ultrasound imaging; however, it uses light instead of sound. Light is directed at the patient, and the backscattered light is captured by the optical system. Then, an image is produced that shows the internal details of the tissue of interest. OCT provides images with higher resolution than ultrasound; however, ultrasound can be used to image deeper into tissue than OCT.

An OCT system is basically an interferometer that has a reference arm and a sample arm. The sample arm delivers light to the tissue, and collects the light backscattered from it. The backscattered light

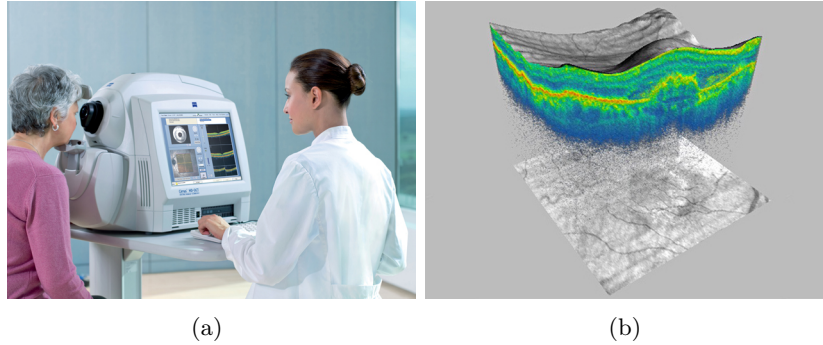


**Figure 1:** OCT is widely used in ophthalmology. a) A patient's retina is being imaged with a commercial OCT (Zeiss Cirrus HD-OCT). b) 3D OCT image of a retina (6 mm  $\times$  6 mm).

is combined with the light from the reference arm and the resulting interference spectrum is captured by a computer. By scanning the light beam over the tissue, 2D cross-sectional and 3D volumetric images are obtained. A commercial OCT device for retinal imaging and a 3D OCT retina image are shown in Figure 1.

Current state-of-the-art OCTs are implemented as Fourier domain OCT (FD-OCT). In FD-OCT, for each position of the scanned beam, the spectrum of the interference is measured and its Fourier transform is calculated to obtain a depth scan (A-scan). Afterwards, all scans are combined to obtain 2D cross-sectional and 3D volumetric images. An FD-OCT system can be implemented in two different ways: 1) Spectral-domain OCT (SD-OCT) – using a broadband light source and a spectrometer in the detection arm. 2) Swept-source OCT (SS-OCT) - using a swept-source laser (tunable laser) with a broad tuning range and a photodetector in the detection arm.

While OCT is being used in many hospitals around the world, costs and complexity are still prohibitive for widespread application in existing and novel areas. Current implementations of OCT systems are commonly based on fiber and free-space optical components. Photonic integration of optical components on a wafer-level has shown advantages in cost, size, stability and power efficiency for telecommunication applications. Optical imaging applications like OCT might also benefit from photonic integration technology.

Photonic integrated circuits (PICs) are analogous to electronic inte-

grated circuits (EICs) in a way that they implement multiple functions on a single monolithic substrate. The fabrication methods of PICs are similar to EICs, where devices are patterned on a wafer using lithography. These patterns are further etched, deposited or altered by diffusion or doping. The basic element of integrated photonics is the waveguide. Other components are usually built by introducing modifications to the simple waveguide structure such as changing the geometry and altering or actively manipulating the physical properties of the waveguide. Photonic integrated devices such as splitters, filters, modulators, amplifiers, lasers, and detectors have been demonstrated in different material systems.

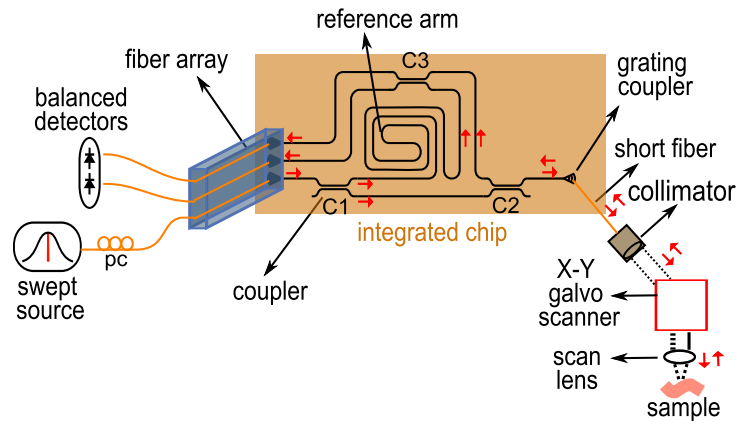
In this thesis, we explored how OCT can benefit from photonic integration. More specifically, we focused on demonstrating integrated photonic interferometers for OCT with on-chip reference arms. We evaluated two material platforms: 1) Silicon-on-insulator (SOI) with 220 nm thick silicon on top of 2  $\mu\text{m}$  thick  $\text{SiO}_2$ . 2)  $\text{Si}_3\text{N}_4$  and  $\text{SiO}_2$  waveguide technology called TriPleX<sup>TM</sup> platform, which was developed by LioniX BV (Enschede, The Netherlands). In addition to the interferometers, we investigated a spectrometer architecture based on multiple arrayed waveguide gratings (AWGs) and ring resonators on SOI.

Using SOI waveguides, we fabricated an integrated interferometer for SS-OCT. SOI waveguides have high refractive-index-contrast between the core and the cladding. This results in high optical confinement, reduced bend radii and enables smaller photonic integrated circuits. The footprint of our integrated interferometer is only 5 mm  $\times$  0.75 mm. The OCT system with the chip is illustrated in Figure 2a. The design consists of waveguides, splitters, a 13 cm physical length (50.44 cm optical length) reference arm and grating couplers. The grating couplers are used to couple the light in and out of the chip. The integrated photonic circuit was used as the interferometer of an SS-OCT system.

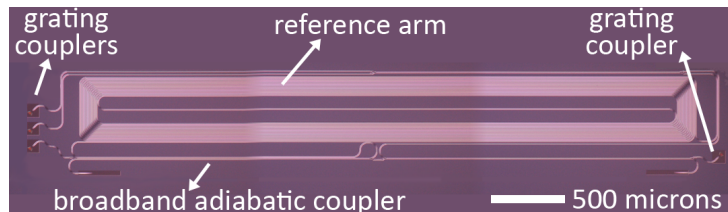
As shown in Figure 2a, light from a swept-source centered at 1312 nm is coupled to the chip using a fiber array. Coupling in and out of the chip is achieved with tilted grating couplers with reduced back reflection, which provide access to the waveguides through vertical coupling. The polarization of the input light is adjusted to the TE-polarization since the grating coupler was designed for TE-light. After entering the chip, the light is split into the reference and sample arms via coupler C1. In the sample arm, the light is split again by coupler C2 and it is sent out of the chip with a grating coupler. The light exiting the chip is coupled to a short piece of fiber, which is attached to a collimator. The

light from the collimator goes to a galvanometric (galvo) x-y scanner with a scan lens. Back reflected light in the sample arm comes back to the chip and combines with the light from the reference arm at coupler C3. The interfered light at both output arms of coupler C3 leaves the chip via grating couplers. The fibers in the fiber array are aligned with these grating couplers and send the light to a balanced photodetector. A microscope image of the fabricated chip is given in Figure 2b.

We characterized the axial resolution and the sensitivity of the system by measuring reflection from a mirror placed in the sample arm. The axial resolution of the system was limited by the bandwidth of the grating couplers (3 dB bandwidth: 45 nm). After 3<sup>rd</sup> order dispersion compensation in software, we obtained 25.5  $\mu\text{m}$  axial resolution, while the theoretical resolution was 24.4  $\mu\text{m}$ . The sensitivity of the system was



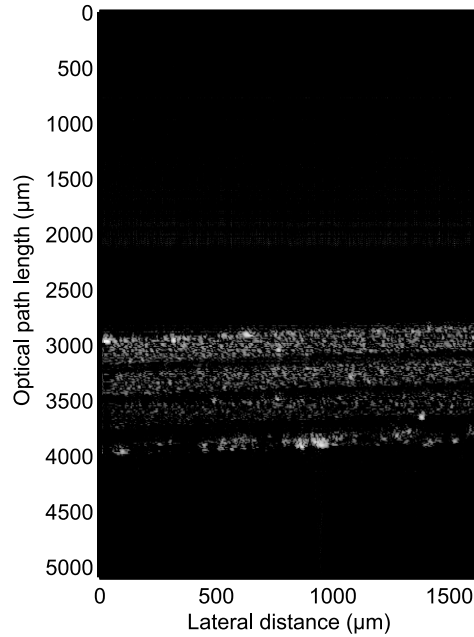
(a)



(b)

**Figure 2:** (a) Illustration of the SS-OCT setup with the silicon photonic integrated interferometer, pc: polarization controller, C1, C2, C3:  $2 \times 2$  couplers. The direction of the light is indicated by red arrows. (b) Microscope image of the fabricated photonic integrated interferometer.

measured to be 62 dB with 115  $\mu\text{W}$  on the sample. Using the setup we demonstrated an OCT image of a layered tissue phantom, as shown in Figure 3.



(a)

**Figure 3:** OCT cross section (average of 100 cross-sectional images) of a layered tissue phantom.

We also fabricated a similar integrated interferometer using TriPleX<sup>TM</sup> waveguides, which have lower loss and dispersion compared to SOI waveguides. A diagram of the OCT setup with the photonic integrated circuit is shown in Figure 4a. The interferometer chip consists of four splitters and a 190 mm long reference arm with a footprint of 10 mm  $\times$  33 mm. It is used as the core of a SD-OCT system consisting of a superluminescent diode (SLED) centered at 1320 nm with 100 nm bandwidth, a spectrometer with 1024 channels, and an x-y scanner. In this system, light from the SLED is butt-coupled to the integrated interferometer, part of the light is directed to the on-chip reference arm, and part of the light is sent out of the chip via the sample arm to a galvanometric x-y scanner. The light returning from the reference and the sample arms are combined and sent to the spectrometer. A photograph

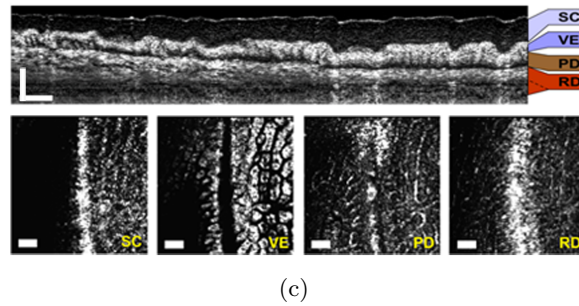
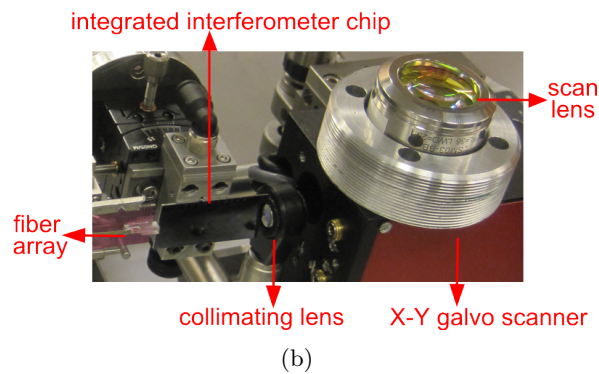
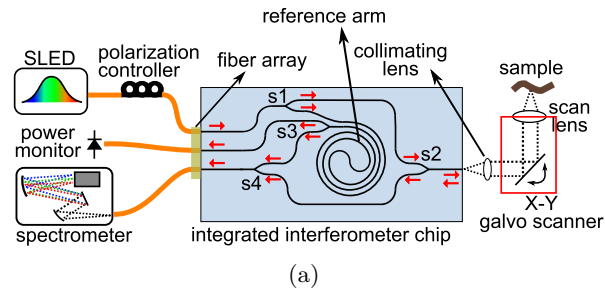


**Figure 4:** a) Schematic layout of the OCT setup with the integrated interferometer chip. The direction of the light is indicated by red arrows. b) Image from the setup, where the fiber array, the integrated interferometer chip, the x-y galvo scanner and the scan lens are seen. c) *In vivo*, OCT cross section and en-face (top) views of human finger mid-joint. The scale bars of the cross-sectional image represent a length of  $500\ \mu\text{m}$ , while the scale bars of the en-face images represent a length of  $1\ \text{mm}$ . SC: stratum corneum, VE: viable epidermis, PD: papillary dermis, RD: reticular dermis.

from the setup is given in Figure 4b.

The measured axial resolution of the system was  $12\ \mu\text{m}$ , which is close

to the  $10\ \mu\text{m}$  theoretical resolution. To achieve such resolution,  $10^{\text{th}}$  order dispersion correction in software was necessary. The sensitivity of the system was measured to be 65 dB with 0.1 mW on the sample. To evaluate the system, we imaged a human finger mid-joint *in vivo*. Cross-sectional and en-face views of OCT images obtained from the finger mid-joint are shown in Figure 4c. Different layers of skin such as the stratum corneum (SC), viable epidermis (VE), papillary dermis (PD) and reticular dermis (RD) can be differentiated in the image.

The results above are the first OCT images using an integrated interferometer with an on-chip reference arm that is sufficiently long to accommodate an x-y scanner. These studies are encouraging towards an on-chip OCT as the sensitivity in both systems with photonic integrated interferometers could be further improved by reducing the insertion losses in fiber to chip coupling. Using more efficient coupling with optimized spot size converters can bring the sensitivity of chip based OCTs to a level ( $> 80\ \text{dB}$ ) obtained by fiber-based OCT systems.

In addition to the interferometers, we investigated the possibilities for high-resolution, multi-channel spectrometers on SOI. Such spectrometers can be potentially used in SD-OCT systems. Using only arrayed waveguide gratings (AWGs) or planar concave gratings (PCGs), fabricating sub-nanometer resolution spectrometers with a large number of channels on SOI is challenging due to fabrication related phase errors. To overcome this limitation, we explored a spectrometer architecture based on cascaded ring resonators and AWGs. An illustration of the proposed spectrometer is given in Figure 5. The spectrometer consists of the 13 AWGs and 13 ring resonators. In front of each AWG, there

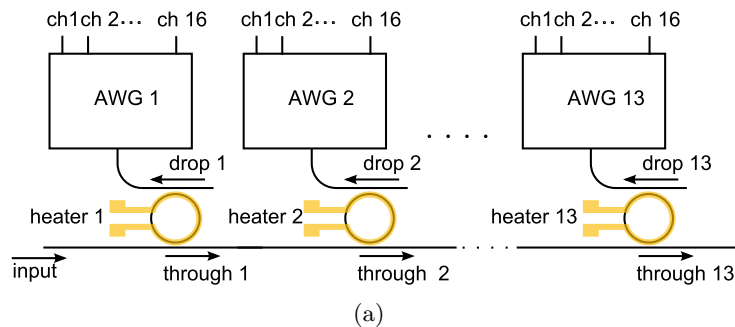


**Figure 5:** Schematic of the spectrometer consisting of 13 cascaded ring resonator and AWG pairs.

is a ring resonator that acts as a pre-filter. Each AWG has 16 channels which results in a spectrometer with a total of 208 ( $13 \times 16$ ) channels.

Let us consider a ring resonator that is placed at the input of an AWG as one of the ring resonator and AWG pairs in Figure 5. In this configuration, the ring resonator pre-filters the light and a comb-like spectrum is sent to the AWG. If the AWG channel spacing and ring resonator free-spectral range are matched, each AWG channel will output a peak from the comb. Simulated transmission spectra of an AWG and a ring resonator are given in Figure 6a; the AWG channels are indicated in color, the ring resonator transmission curve is plotted in black. The free spectral range (FSR) of the ring resonator matches the channel spacing of the AWG. The combined transmission spectrum of a cascaded ring resonator and an AWG is given in Figure 6b.

In our design, the channel spacing of each AWG is 1.95 nm. The FSR of the ring resonators is matched to the channel spacing of the AWGs and is also 1.95 nm. Due to fabrication related imperfections, ring resonator peak positions are not properly matched with the AWG channels. To fix this problem, the resonance peaks of the ring resonators are thermally tuned using metallic heaters deposited above the ring resonators. The

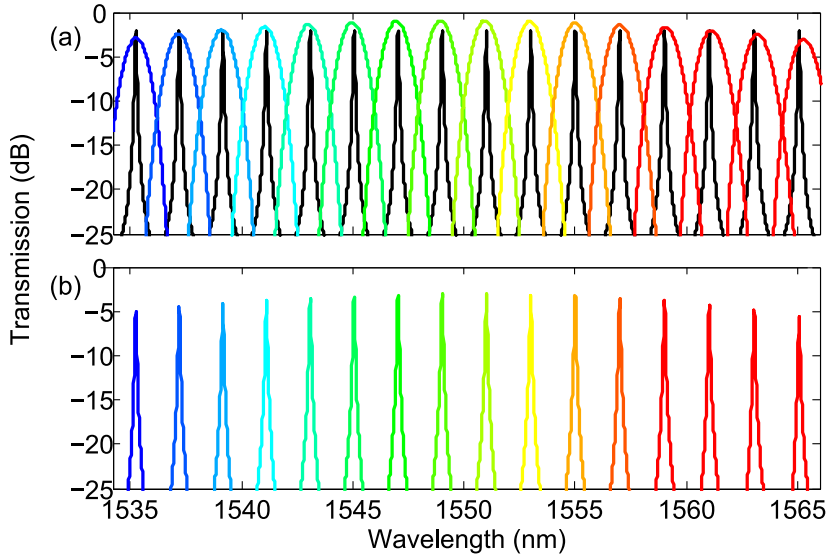
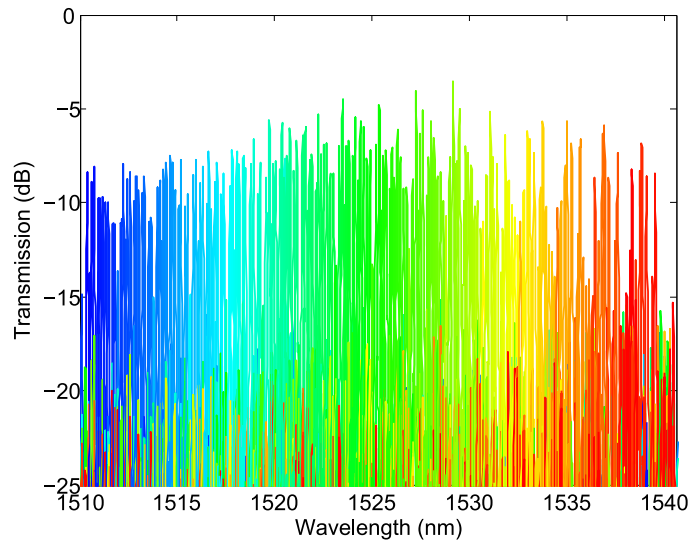
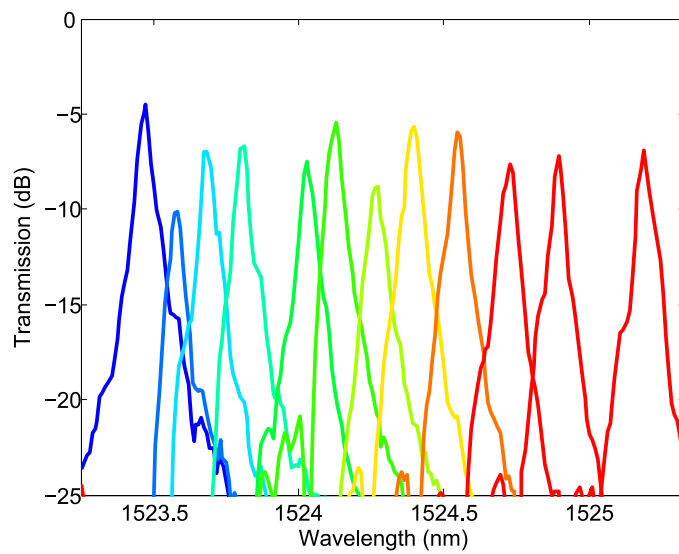


**Figure 6:** a) Transmission spectra of an individual AWG (colored lines) and a ring resonator (black line). b) Transmission spectrum of a cascaded AWG and ring resonator.



(a)



(b)

**Figure 7:** a) Transmission spectrum of the 208 channel spectrometer. (b) Transmission spectrum of the mid channels only, to show more detail.

thermal tuning is adjusted such that, the comb of a ring resonator is shifted slightly (0.15 nm) with respect to the comb of the preceding

ring resonator. With these parameters we obtain a spectrometer with  $1.95/13 = 0.15$  nm channel spacing. The full width at half maximum of the resonance peaks of the ring resonator is 0.06 nm.

By thermally tuning the ring resonators, we measured the transmission spectrum of the spectrometer. Figure 7a shows the device transmission for all channels. The transmission is normalized for fiber-to-chip coupling losses. In Figure 7b, the central channels are plotted to show more detail.

In this thesis, we investigated passive integrated photonic components for OCT. For the first time, we showed images of tissue phantom and human skin using OCT systems with integrated interferometers containing long reference arms. In order to proceed with more complex photonic integrated circuits for OCT, it is necessary to optimize fiber-to-chip coupling losses. We also demonstrated a high-resolution, multi-channel spectrometer on SOI. Further improvement in fabrication tolerances would enable ultra-compact spectrometers. Integration of active devices such as light sources and detectors on top of passive structures similar to the ones demonstrated in this thesis will open a road towards fully integrated OCT systems.

# 1

## Introduction

Medical imaging technologies are essential for diagnosis and clinical management of diseases. In addition, they are also widely used in medical research related to understanding disease pathogenesis and development of better therapies. X-ray radiography, magnetic resonance imaging (MRI) and ultrasound are some of the widely used medical imaging modalities. They provide a window to the internal human body parts, revealing the structures hidden by skin and tissue. While these existing medical imaging technologies improve, new medical imaging technologies that can overcome some of the limitations of existing modalities are also being invented.

In the last two decades, a new imaging modality called optical coherence tomography (OCT) [1] has emerged as an important diagnostic tool, especially in ophthalmology [2]. In this section, first, we will provide an overview of OCT and its applications. Then, we will review the literature on miniaturization of OCT systems. Finally, we will provide an outline of the thesis.

## 1.1 Optical coherence tomography and its applications

Optical coherence tomography (OCT) is a non-invasive, imaging modality capable of producing real-time, cross-sectional, high-resolution images of semi-transparent samples such as biological tissue. OCT can image tissue cross sections with  $< 10\ \mu\text{m}$  axial resolution at depths exceeding 2 cm in transparent tissues (e.g. human eye, animal embryos) and 1-2 mm in highly scattering tissues (e.g. skin, retina, blood vessel wall). The resolution and penetration depth of OCT and other major imaging modalities are shown in the Figure 1.1. Each of these imaging methods measure different physical properties and has a resolution and penetration depth that prove advantageous for specific applications. Confocal microscopy, which is an optical imaging technique, enable high axial and transverse ( $< 1\ \mu\text{m}$ ) resolution imaging, but have limited penetration in biological tissue. Ultrasound imaging uses high-frequency sound waves to view soft tissues such as muscles and internal organs. High frequency ultrasound imaging yields improved resolution, up to  $100\ \mu\text{m}$ , at the expense of a shallower penetration depth. MRI uses powerful magnets and radio waves to form images of the body with up to 1 mm resolution. It relies on detecting a radio frequency signal emitted by excited hydrogen atoms in the body. Computed tomography (CT) takes multiple X-ray images from different angles to reconstruct 3D images. The resolution of CT is comparable to MRI.

From Figure 1.1, we see that the achievable resolution and penetration depth of OCT nicely fills the gap between confocal microscopy and high-frequency ultrasound. Its capabilities place OCT in a unique position for non-invasive visualization of microstructural morphology in specific applications.

The working principle of OCT is similar to ultrasound; it is an optical analog of ultrasound imaging. Ultrasound builds images by sending sound waves to tissue and by recording the sound waves scattered by tissue. While, OCT builds images by sending light waves to tissue and by recording the light waves reflected by tissue. An optical signal reflected from a biological tissue contains magnitude and time delay information, which yields depth-resolved reflectivity profile of tissue. Contrast in OCT images arises from the boundaries of structures with different refractive indices.

Despite of many similarities between OCT and ultrasound, the recovery mechanism of time delay information is different. The speed of sound

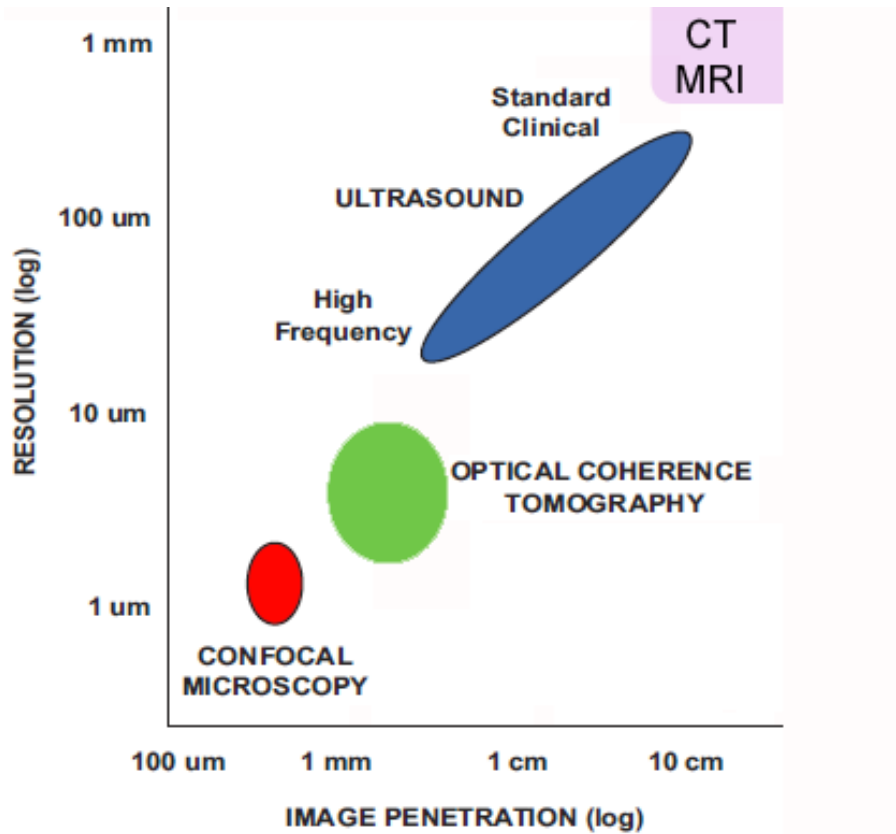


**Figure 1.1:** Penetration depth and resolution of prevailing imaging modalities (figure modified from [3]).

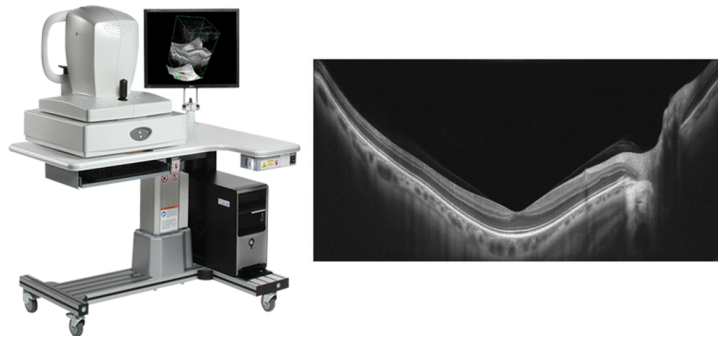
is approximately 1500 m/s in tissue and the time delay corresponding to 100  $\mu\text{m}$  distance between two scatterers is 130 ns (waves travel twice that distance in back-reflection mode). Such time delays, typical in ultrasound imaging, are recorded with high speed electronic circuits. On the other hand, the speed of light in tissue is around  $2 \times 10^8$  m/s. To measure the delay of light between two scatterers separated by 10  $\mu\text{m}$ , temporal resolution of 100 fs is required. With current electronic circuits such signals with that level of small delay can not be detected. However, we can resolve such short delays using interferometry. In OCT, the backscattered light is combined with a reference light beam and by processing the resulting interference signal, the depth resolved reflectivity profile is extracted. By scanning the beam over the sample, 2D or

3D images are obtained. Images are displayed in false color or grayscale to visualize tissue structure.

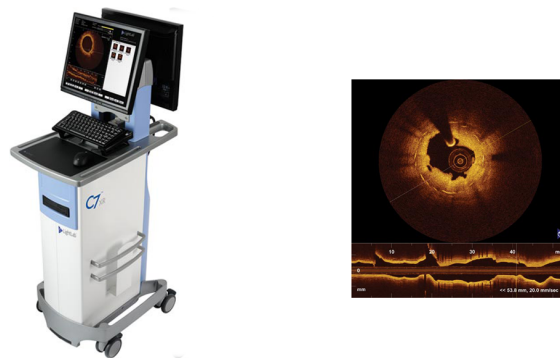
OCT is especially useful for imaging applications where tissue microstructures of interest are few millimeters thick and require high resolution. OCT imaging can be thought as an "optical biopsy"; without excising and processing tissue samples, it provides real-time, in situ visualization of tissue microstructure with resolutions of  $< 10 \mu\text{m}$ . Such imaging can be utilized in different situations: (1) Where excision of the tissue is not a viable option, such as the eye. (2) Diagnosis of some diseases like cancer may require excisional biopsy. If the excisional biopsy area is large, with few excisions the diseased tissue may not be sampled correctly. OCT imaging can be used to guide biopsy sampling in such situations. (3) Using optical fibers to deliver and collect light, OCT can be coupled with catheter, endoscopic or laparoscopic type devices to image hollow body organs such as the cardiovascular system, gastrointestinal tract, bladder etc.

OCT has found clinical applications in ophthalmology [2], intravascular imaging [4] and dermatology [5]. Commercial ophthalmic, intravascular and dermatological OCT devices and typical OCT images of retina, blood vessel and skin are shown in Figure 1.2. Structures such as retina, blood vessel and skin consist of layered structures and OCT is ideal for imaging such tissues with high resolution. Applications in other medical fields, such as gastroenterology [6], pulmonology [7], and dentistry [8] may emerge from research to clinic [9] in the future.

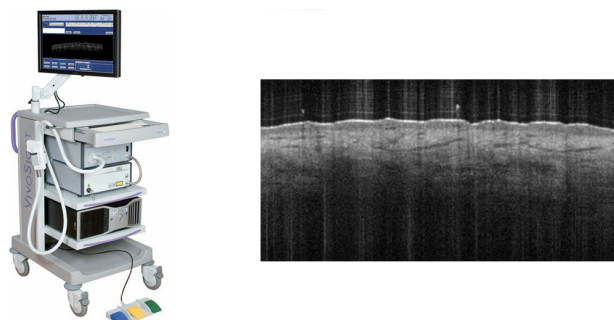
Industrial applications of OCT for material characterization are also being investigated. Specifically, materials which are transparent to near-infrared or telecom wavelengths can be inspected with OCT. Such materials include silicon, many polymers and plastics, some ceramics, and organic materials such as pearl. Studies have shown that OCT can be useful for surface and thickness measurements; non-contact material characterization for ceramics, glass and optical components, polymers, fiber composites; and quality evaluation of data storage devices [11]. OCT images of a liquid crystal display (LCD) with defects are shown in Figure 1.3. High-throughput imaging for manufacturing and process control of such products can benefit from OCT. As awareness of OCT increases in industrial manufacturing environments and its benefits are better understood, OCT is likely to find more applications in material characterization and process monitoring.



(a)



(b)



(c)

**Figure 1.2:** Commercial OCT devices and OCT images. a) Ophthalmic OCT (Optovue, USA) and retina image. b) Intravascular OCT (St. Jude Medical, USA) and blood vessel image. c) Dermatological OCT (Michelson Diagnostics, UK) and skin image.

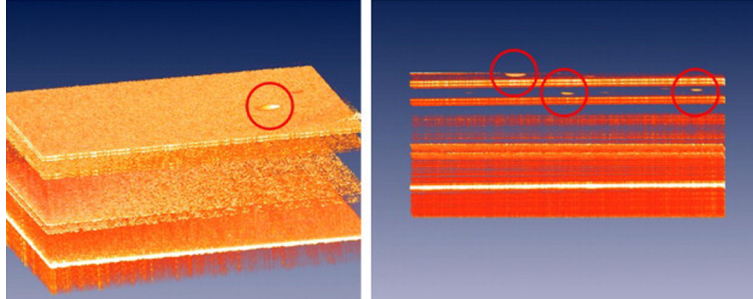


**Figure 1.3:** 3D and 2D cross-sectional OCT images of an LCD panel with defects. The defects are indicated with red circles [10].

## 1.2 Types of OCT implementations

A typical OCT system consists of a broadband light source, an interferometer, a photodetector, an x-y galvo scanner and a computer. A number of different types of OCT imaging techniques have been developed for obtaining images from backscattered light. They are mainly divided as time-domain OCT, full-field OCT and Fourier-domain OCT.

### 1.2.1 Time-domain OCT

The first generation OCTs were time-domain systems. Time-domain OCT (TD-OCT), first demonstrated in 1991 by Huang et al. [1], is an extension of low-coherence interferometry to imaging. Low-coherence interferometry has been used mainly for reflection measurements in optical components [12], [13]. It is also called optical coherence-domain reflectometry (OCDR), when it is used for determining the positions and magnitudes of reflection sites within miniature optical assemblies [14]. A schematic of a TD-OCT is given in Figure 1.4. Light from a broadband (low-coherence) light source is split into two arms (paths). The light in the sample arm is directed at the sample surface and the light in the reference arm is directed at a moving reference mirror. The backscattered light from the sample and reference arms are combined and send to a photodetector. Due to the broadband (low coherence) nature of light, interference of the optical fields occur only when the path lengths of the reference and the sample arm are matched to within the coherence length of the light. The reference mirror is moved in a linear fashion to change the reference arm path length and match different optical paths corresponding to the reflections from the sample. An illustration

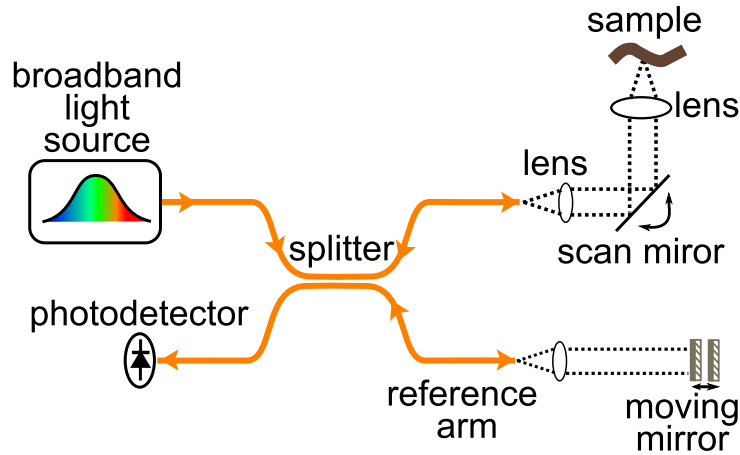


**Figure 1.4:** Schematic diagram of time-domain OCT.

of a TD-OCT signal for two discrete reflectors is given in Figure 1.5. The envelope of the interference provides the reflectivity profile of the sample.

Generation of OCT images from reflectivity profiles is shown in Figure 1.6. A depth-resolved reflectivity profile is commonly referred to as an axial scan (A-scan) or A-line. An A-scan is obtained by moving the reference arm mirror for a few millimeters, depending on the desired imaging depth. In order to obtain cross-sectional, 2D images (B-scan), after each A-scan acquisition, the position of the beam on the sample is slightly shifted by a scan-mirror and another A-scan is acquired. Typically, 512 or 1024 axial scans are acquired to obtain a cross-sectional image. By mapping different intensity levels in reflectivity profiles to different colors, an image is created from the 2D data set. Gray scale or false color map is used to represent the reflectivity amplitudes. Three-dimensional, volumetric data sets can be generated by acquiring sequential cross-sectional images by scanning the incident optical beam in a raster pattern.

The imaging speed in TD-OCT is limited by the scan speed of the reference arm delay line. Using mechanically translated mirrors, scan velocity of approximately 30 cm/s can be achieved. For 3 mm imaging depth, that would correspond to  $\sim 100$  Hz axial scan rate. Higher axial scan rates have been achieved by using a grating-based delay line, termed as rapid-scanning optical delay (RSOD). Using RSOD, linear axial scanning over a range of 3 mm at a velocity of 6 m/s and a repetition rate

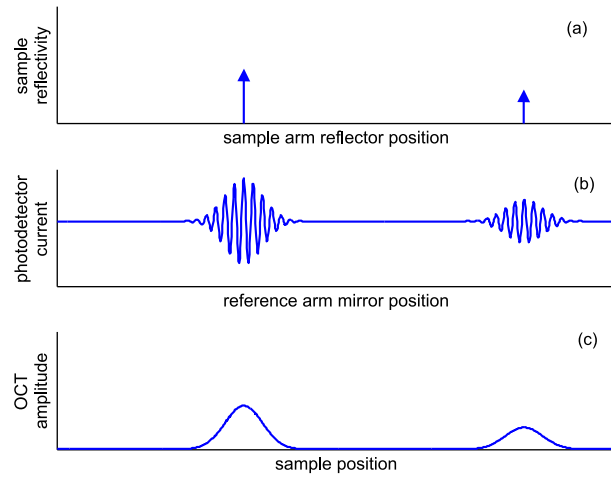


**Figure 1.5:** Illustration of TD-OCT signal for a sample with two discrete-reflectors.

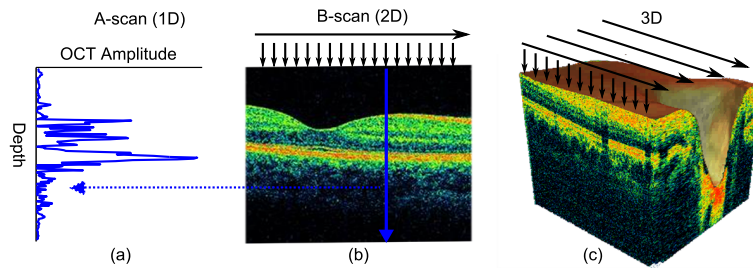


**Figure 1.6:** Generation of cross-sectional and volumetric OCT images. a) Axial reflectivity profile (A-scan). The A-scan is the reflectivity profile of the blue line in the cross-sectional image in b. b) Generation of a cross-sectional image (B-scan) from consecutive A-scans c) Volumetric, 3D image reconstruction by stitching multiple B-scans. The images are obtained from [15].

of 2 kHz has been demonstrated [16]. Imaging speed of 2 kHz (A-scan/s rate) is relatively slow compared to Fourier-domain OCT (FD-OCT) systems. FD-OCT systems have better sensitivity and can achieve much higher scan rates which is necessary for imaging large tissue volumes and beneficial for a wide variety of medical applications.

### 1.2.2 Full-field OCT

The full-field OCT technique is based on white-light interference microscopy [18]. A schematic diagram of a full-field OCT is given in Figure 1.7. In contrast to TD-OCT and FD-OCT, the entire field of view is illuminated with low spatial and temporal coherence light and it does not require scanning of the light beam over the sample. Full-field OCT typically uses a 2D image sensor such as a charge-coupled device (CCD) or complementary metaloxide-semiconductor (CMOS) camera to acquire the interferometric signal in parallel. Unlike TD-OCT and FD-OCT approaches, which acquire images in axial orientation, full-field OCT acquires images in *en face* (transverse) orientation. A nanometric-resolution piezoelectric transducer (PZT) is adjusted to correctly sample the interferometric signal. In full-field OCT, spatially incoherent, very broadband source such as a thermal tungsten filament lamp or a Xenon arc is used to achieve ultra-high ( $\sim 1 \mu\text{m}$ ) axial resolution. *En face* image acquisition also enables high lateral resolution ( $\sim 1 \mu\text{m}$ ) using high-NA microscope objectives. The focal plane is moved at different depths to

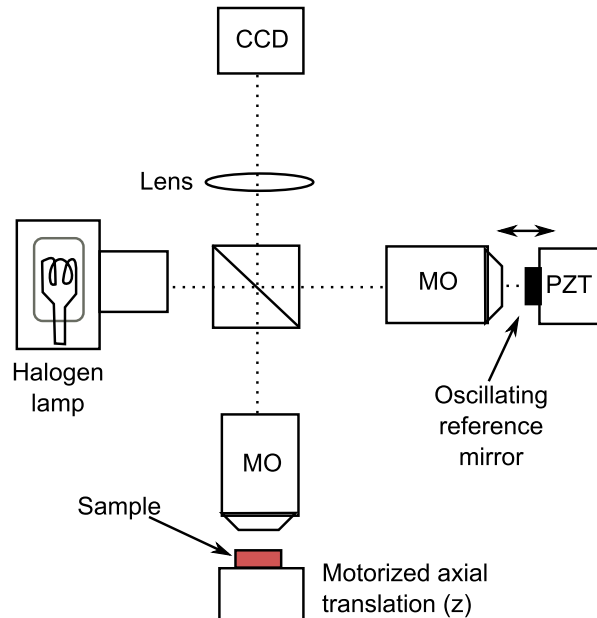


**Figure 1.7:** Schematic diagram of a full-field OCT. MO: microscope objective, BS: beam-splitter, PZT: piezoelectric stage actuator, CCD; charge-coupled device (figure modified from [17]).

produce 3-D tomographs from the *en face* images. Thus, 1  $\mu\text{m}$  isotropic resolution images that compare favorably with the histology sections of the same tissues [19] can be obtained. However, due to inherent sensitivity of *en face* acquisition to motion, *in vivo in vivo* imaging with full-field OCT is challenging.

Currently, light sources used in full-field OCT are bulky. In the future, if a small light source with low spatial and temporal coherence can be used together with a mobile phone camera, the full-field OCT approach could enable portable, low cost OCTs for histology applications. In this thesis, the focus is on the miniaturization of FD-OCTs using photonic integrated components.

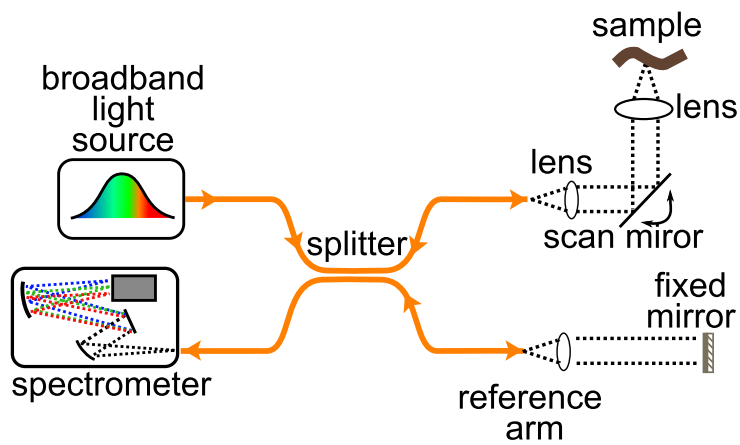
### 1.2.3 Fourier-domain OCT

In Fourier-domain OCT, the length of the reference arm is kept fixed and the depth information is obtained by recording the spectrum of the interference. An FD-OCT system can be implemented in two different ways: spectral-domain OCT (SD-OCT) and swept-source OCT (SS-OCT). A schematic diagram of SD-OCT and SS-OCT are shown in 1.8a and 1.8b respectively. In SD-OCT, a broadband light source such as a superluminescent LED (SLED) is used as a light source and the spectrum of the interference is measured using a spectrometer. While, in SS-OCT the light source is a swept-source laser (tunable laser) and the spectrum is recorded using a photodetector. As a side note, naming spectrometer-based OCT as SD-OCT seems to be a little confusing because spectral-domain and Fourier-domain are sort of synonyms. However, in OCT literature the naming convention was initially chosen like that.

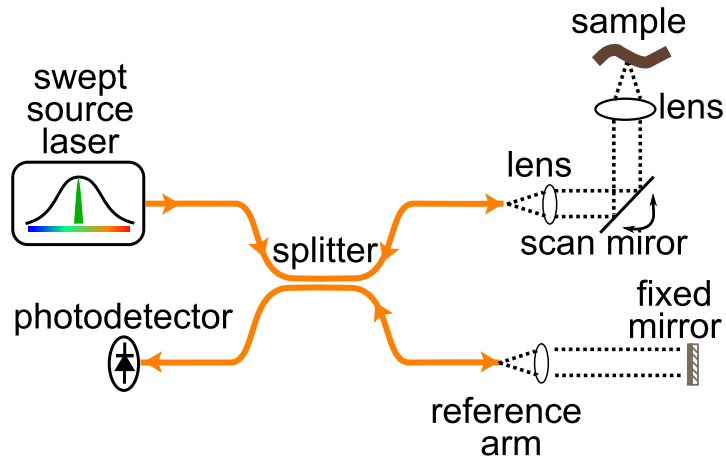
The procedure to obtain an A-scan in FD-OCT is different than in TD-OCT. An illustration of an FD-OCT signal for two discrete reflectors is given in Figure 1.9. The interference between a reflection from the sample and a reflection from reference arm mirror creates a sinusoidal modulation in the spectrum. The oscillation frequency of the modulation is proportional to the path difference between the sample and reference arms. When the path length difference increases, the frequency of the modulation also increases. Thus, scatterers at different depths produce modulations at different frequencies. The magnitude of the oscillation is proportional to the sample reflectivity. The interference spectrum is usually measured in wavelength, and later rescaled to frequency; Fourier transform of the spectrum in frequency scale provides a depth-resolved

reflectivity profile of the sample, namely an A-scan. Like in TD-OCT, the axial resolution in FD-OCT is inversely proportional to the source bandwidth. For a Gaussian-shaped light source, the axial resolution is given by [20]:

$$\Delta z = \frac{2 \ln 2}{n_g \pi} \frac{\lambda_0^2}{\Delta \lambda} \quad (1.1)$$



(a)



(b)

**Figure 1.8:** Schematic diagram of Fourier-domain OCTs. a) Spectral-domain OCT. b) Swept-source OCT.

where  $\Delta z$  is the full-width-at-half-maximum (FWHM) of the axial resolution,  $\Delta\lambda$  is the FWHM bandwidth of the light source,  $\lambda_0$  is the center wavelength of the light source and  $n_g$  is the group index of the medium. The broader the spectrum, the better the resolution. Also for the same bandwidth in wavelength, better resolution is obtained at smaller wavelengths.

The maximum possible imaging depth, in TD-OCT is determined by the delay in the reference arm. On the other hand, in FD-OCT, it depends on the spectral resolution of the measured spectrum and is given by the following formula [20]:

$$z_{\max} = \frac{\lambda_0^2}{4n_g\delta\lambda} \quad (1.2)$$

where  $z_{\max}$  is the maximum imaging depth,  $\lambda_0$  is the center wavelength,  $n_g$  is the group index of the medium and  $\delta\lambda$  is the spectral resolution.

Fourier-domain detection measures backscattering from all depths simultaneously, while time-domain detection measures backscattering from a single depth. For that reason, Fourier-domain detection has a significant sensitivity advantage over time-domain detection [21]–[25]. The sensitivity improvement is approximately the ratio of the imaging depth to the axial resolution. For imaging depth of 2 mm with 10  $\mu\text{m}$  axial resolution, this corresponds to a sensitivity increase of 200 times. As mechanical scanning is not necessary in the reference arm and there is a significant sensitivity enhancement, higher acquisition speed with respect to TD-OCT is achieved. Increased imaging speed shortens the examination time, reduces exposure time and motion artifacts.

### Comparison of SD-OCT to SS-OCT

In principle, both SD-OCT and SS-OCT measure the spectrum of the interference and provide the same information. However, the small differences in the implementation have practical consequences. We briefly explain these differences in this section.

Both SD-OCT and SS-OCT have depth dependent signal degradation (sensitivity fall-off), which is related to the resolution of the recorded spectrum. In SD-OCT, the spectrum is recorded by a line scan camera, which have finite pixel size. Thus, the spectrum in SD-OCT is convolved with a rectangular (rect) function. The Fourier transform of the rect function is a sinc function, whose amplitude decreases away from the origin. This sinc function multiplies the depth-resolved backscat-

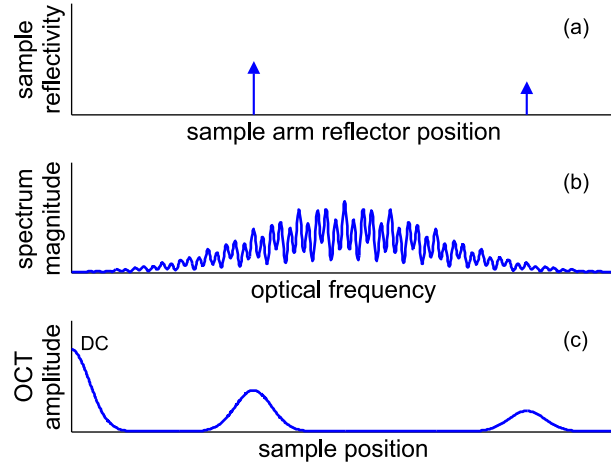


**Figure 1.9:** Illustration of FD-OCT signal for a sample with two discrete-reflectors. a) Sample reflectivity. b) Spectral interference. c) Fourier transform of the spectral interference which gives the sample reflectivity profile.

tering information and reduces the magnitude of the OCT signal with increasing depth [26]. The 6 dB fall-off in SD-OCT is typically 1 mm, which can be improved by increasing the resolution of the spectrometer. On the other hand, the spectral resolution of a SS-OCT system is determined by the instantaneous linewidth of the swept-source laser. Thus, the spectrum in SS-OCT is convolved with the Fourier transform of the instantaneous linewidth. The smaller the line width, the less the depth dependent signal degradation. There have been several developments in swept-source lasers for reducing the instantaneous linewidth. Nowadays, swept-sources with 6 dB fall-off  $> 10$  mm are common.

In SS-OCT, usually balanced detection is used [27], while balanced detection in SD-OCT requires two identical spectrometers [28] and is not so practical to implement it. In OCT imaging, balanced detection provides multiple benefits: it suppresses intensity fluctuations of the light source; reduces self-interference signals originating from multiple reflections within the optical components; it also improves the dynamic range by removing the relatively large background signal.

Both SD-OCT and SS-OCT systems are operated at sufficiently high speeds for *in vivo* cross-sectional imaging. Ultrahigh speed imaging can further reduce motion artifacts for real-time 3D imaging. Currently, the speed of swept-source lasers have a factor of 10 higher scan rates than line scan cameras, providing speed advantage to SS-OCT over SD-OCT.

Axial resolution improves with increasing light-source bandwidth. Compared to swept-source lasers broader bandwidth can be obtained with femtosecond lasers, supercontinuum sources and multiple SLEDs. This provides an advantage to SD-OCT over SS-OCT in terms of axial resolution. Currently, the high axial resolution of 2-3  $\mu\text{m}$  that is possible with SD-OCT systems can not be matched by SS-OCT systems, which have axial resolution on the order of 10  $\mu\text{m}$ . Due to higher axial resolution, most of the current commercial ophthalmic OCT systems are implemented as SD-OCT with center wavelengths around 850 nm.

In the last decade, there has been tremendous advances in FD-OCT enabling unprecedented imaging speeds. Thanks to the profound increase in imaging speed, *in vivo* 3D-OCT volumetric imaging has become possible. For example, in retinal imaging, acquisition time of < 1 s is necessary for motion artifact free 3D imaging. Additionally, with high speed imaging, multiple cross-sectional scans can be averaged to further improve image quality.

### Choice of center wavelength in OCT

From Eq. 1.1 we can see that if we keep the source bandwidth constant and use shorter wavelengths, the axial resolution improves quadratically. In other words, for the same axial resolution, at shorter wavelengths we can use light sources with smaller bandwidths. However, the penetration depth in semi-transparent materials such as biological tissue is limited by scattering or absorption and scattering reduces with increasing wavelength. The relation between wavelength and imaging depth for tissue was estimated by Faber et. al [29] and is reproduced in Figure 1.10. They also plotted the spectral width necessary for 10  $\mu\text{m}$  axial resolution. From the figure, we see that imaging depth improves with increasing wavelength, the dips are due to water absorption bands.

For retinal imaging the choice of wavelength has been either 800 nm or 1050 nm. Povazay et al. showed that lower scattering at 1050 nm provides greater penetration into choroidal tissue compared to conventional 800 nm systems [30]. In imaging the anterior (front) part of the eye, 1300 nm allows greater penetration through highly scattering tissues such as limbus and sclera, thus yielding visualization of angle structures [31]. To image as deeply as possible with reasonable axial resolution, OCT systems for skin imaging also use 1300 nm [32], [33]. Kawagoe et. al developed a supercontinuum source with center wavelength of 1700 nm and obtained better penetration depth for low-water-

absorption samples compared to 1300 nm [34]. OCT has also attracted interest for imaging paintings. Liang et al. analyzed the scattering and absorption properties of historic pigments/paints and concluded that the optimum spectral window for imaging of art with OCT is centered around 2200 nm [35].

### 1.3 Developments in FD-OCT

#### 1.3.1 Developments in spectral-domain OCT

The first SD-OCT implementation was reported in 1995 by Fercher et al. [36]. In that study, it was used to measure intraocular distances. After 3 years, the first images with SD-OCT were demonstrated by Hausler et al. [37]. In 1999, the same group [21] and Mitsui [22], independently discussed that SD-OCT has sensitivity advantage over TD-OCT. Despite these reports, the OCT community in large have not realized the ad-

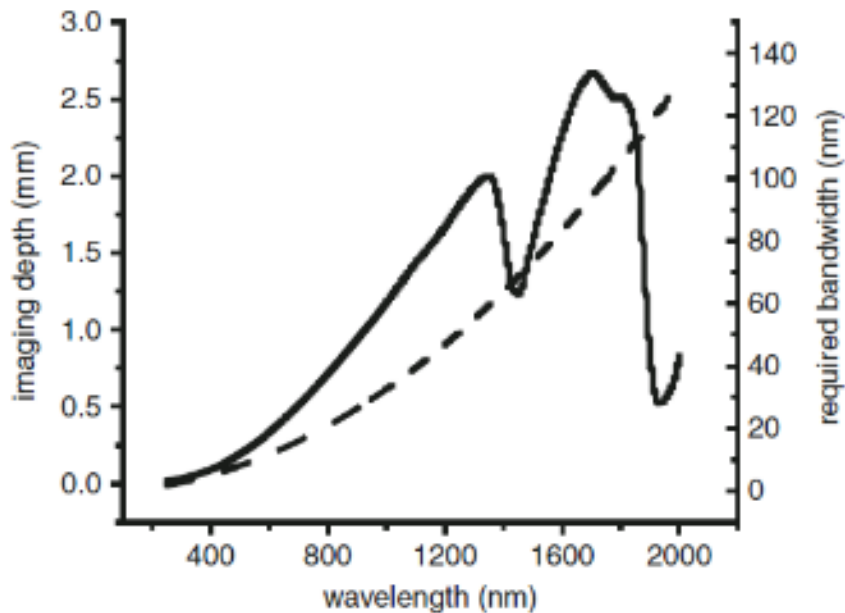


**Figure 1.10:** Imaging depth (solid curve) and bandwidth (dashed curve) required for the OCT light-source to maintain a resolution of 10  $\mu\text{m}$  as a function of wavelength (calculated for typical parameters of an OCT system and tissue properties). The graph is reproduced from [29]

vantage of FD-OCT until 2003. In 2003, three well-known OCT groups argued the same in popular optics journals [23]–[25]. After realization of the sensitivity advantage, and availability of high-speed line scan cameras, research in OCT rapidly shifted from TD-OCT to FD-OCT. In 2004, Nassif et al. [38] demonstrated video rate, *in vivo* retinal imaging using SD-OCT with 29,000 axial scans per second and 6  $\mu\text{m}$  axial resolution. In the same year, ultrahigh-resolution SD-OCT retinal imaging was demonstrated: Cense et al. showed 3.5  $\mu\text{m}$  resolution in tissue at 14,600 axial scans per second using a multiplexed superluminescent diode light source [39] and Wojtkowski et al. demonstrated 2.1  $\mu\text{m}$  resolution in tissue at 19,000 axial scans per second using a femtosecond laser light source [40]. Using graphics processing unit (GPU) processing power with high-speed OCT, real time, 3D OCT imaging has become possible. Zhang et al. immediately processed and visualized 5 volume/s, with 100 B-scans/volume and 256 A-scans per B-scan. Currently, CMOS line scan cameras with 140 kHz line rates (Basler AG, Germany) and InGaAs line-scan cameras with 92 kHz line rates (Sensors Unlimited Inc, USA) are commercially available. The imaging speed of SD-OCT is limited by the line-rate of the line scan camera which records the spectrum. As new cameras with higher line rates come to the market, the imaging speed of FD-OCT will further increase.

The progress that has been made in FD-OCT is nicely demonstrated by comparing TD-OCT and FD-OCT images of retina, given in Figure 1.11. Certainly, the increase of axial resolution as a result of using very broadband light source (femtosecond laser) provides much more details. However, such resolution would not be effective with TD-OCT imaging speed, due to motion related blurring. Thanks to the shorter measurement time in FD-OCT, the image quality is not hindered as much as in TD-OCT.

### 1.3.2 Developments in swept-source OCT

Like TD-OCT and FD-OCT, SS-OCT is an extension of an existing method for measurement of reflections, namely optical frequency-domain reflectometry (OFDR). For that reason, SS-OCT is also called optical frequency-domain imaging (OFDI) by some research groups. OFDR has been used for optical component characterization, by measuring backreflections from fibers and waveguides [42]–[45]. The development phases of SS-OCT have been similar to SD-OCT. In SS-OCT, the A-scan rate depends on the scan rate of the swept-source laser. As the scan rate of

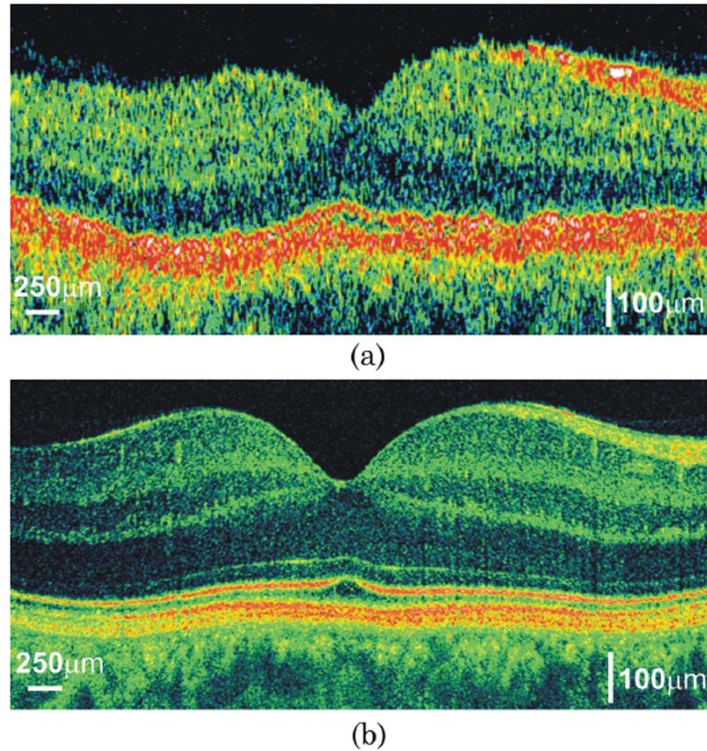


**Figure 1.11:** Comparison of cross-sectional *in vivo* human retina OCT images. a) Image taken with a commercial TD-OCT (ZEISS Stratus OCT 3); 400 A-scans/sec, 10  $\mu\text{m}$  axial resolution. b) Image taken with a laboratory-built FD-OCT; 30,000 A-scans/sec, 2  $\mu\text{m}$  axial resolution. The figure is modified from [41].

the lasers has improved, imaging speed of SS-OCT has increased. OCT images using swept source were first demonstrated in 1997 by Chinn et al. [46] with 10 Hz scan rate and Golubovic et al. [47], with 2 kHz scan rate. The initial swept-source lasers were slow and noisy, and the sensitivity advantage was not recognized till 2003, when Choma et al. showed theoretically and demonstrated experimentally that SS-OCT can have a higher sensitivity than TD-OCT using a commercial fiber laser with 350 Hz scan rate [25]. Due to the necessity for such lasers in SS-OCT, considerable effort has been devoted in the last decade to the development of rapidly scanning, widely tunable laser sources.

In 2003, Yun et al. developed a rapidly-tuned swept-source laser and

demonstrated high-sensitivity OCT images with A-scan rate of 16 kHz and 13.5  $\mu\text{m}$  axial resolution [48]. The enabling component of the laser in that study was a novel wavelength-scanning filter based on a polygonal scanner and a diffraction grating. The same research group demonstrated SS-OCT imaging at higher imaging speeds by improving the scan rate of the laser; first at 115 kHz [49] and later at 403 kHz [50]. A significant improvement in OCT imaging speed has been the invention of the Fourier-domain mode locked laser (FDML) in 2006 by Huber et al. [51], [52]. The first FDML laser operated around 1300 nm and had a sweep rate of 290 kHz. Currently, FMDL lasers reached a sweep rate of 5.2 MHz [53]. FDML lasers use a very long fiber-based cavity and synchronously tune a high-finesse, tunable bandpass filter. The tuning rate of the filter is matched to the round-trip time of the cavity. More recently, there has been development in MEMS-tunable vertical-cavity surface-emitting lasers (VCSEL) for SS-OCT. Currently, optically pumped MEMS-tunable VCSELs have reached sweep rate of 1 MHz at 1300 nm [54].

### 1.3.3 Alternative developments in high speed FD-OCT

Besides the standard SD-OCT and SS-OCT, there have been important developments based on the Fourier-domain detection principle. These developments can be basically considered as modified SD-OCT and SS-OCT approaches. One of the methods is to replace the swept-source laser in SS-OCT with a femtosecond laser followed by a dispersive pulse stretcher that produces pulses on the order of 100 nm. Such a pulse contains different wavelengths at different positions in the pulse. In other words, it maps the spectrum of an optical pulse into a temporal waveform. Once the wavelength and time relation is calibrated, the spectrum can be measured using a single photodetector [55]. Using this technique, Goda et al. [56] demonstrated a record high axial scan rate of 90.9 MHz. Another method that achieves MHz A-scan rates is using an arrayed waveguide grating (AWG) with discrete channels. Each channel of the AWG is connected to a photodetector, thus the A-scan speed is limited by the acquisition speed from the individual photodetectors. With such a system, A-scan rate of 60 MHz has been reported by Choi et al. [57].

## 1.4 Miniaturization of OCT

As a result of the recent advances in OCT performance, such as improved axial resolution and scan speed, OCT has strengthened its position as a medical imaging modality with many more applications to come. Adoption of a technology not only depends on its capabilities, but also on its price and size. Miniaturization of OCT can reduce both the size and price, enabling its widespread use in many areas; medical as well as industrial. There are mainly two approaches to miniature OCT components: Micro-electromechanical system (MEMS) technology and integrated photonics. Both of these technologies use semiconductor processing technologies similar to the ones used in electronic integrated circuit fabrication. The basic wafer-scale fabrication techniques are: patterning by photolithography, etching and deposition of material layers to produce the patterned shapes. Pursuing these methods, several OCT components such as scanners, swept-source lasers, spectrometers, interferometers and photodetectors have been miniaturized.

### 1.4.1 MEMS for OCT

MEMS technology is very suitable for realizing micro actuators such as movable mirrors and membranes. Developments in such actuators bring new opportunities for miniaturizing optical systems. MEMS based scanning mirrors have been used to develop compact OCT scanners and MEMS movable membranes enabled small tunable lasers.

In OCT systems, galvanometer scanners are commonly used to scan the beam over the sample. Galvanometer scanners can easily hold sufficiently large mirrors to accommodate a beam diameter of 5 mm - 10 mm that is necessary to obtain a small spot size at the focus point of a typical scan lens. Due to wide availability, high speed, stability and reliability, they are currently the most widely used scanner technology in many applications. Galvanometer scanners consist of two orthogonally oriented X and Y servo motors which are housed in an aluminum mount to dissipate the heat of the motors. The aluminum mount and the size of the motors constrain the minimum size and weight of the scanner. Using MEMS mirrors for beam scanning, more portable OCT scanners have been demonstrated in hand-held [58] and endoscopic scanners [59]. Only very recently, few companies like Mirrorcle Technologies (CA, USA) and Sercalo Microtechnology (Neuchâtel, Switzerland) started to offer MEMS mirrors. The development of MEMS mirror technology is currently driven by high-volume applications such as barcode scanners and

microprojectors. OCT can leverage these developments, and it is likely that in near future MEMS mirror technologies will replace traditional galvanometer mirrors. Additionally, for some applications scanning can be even done manually by scanning the probe laterally over the sample [60]–[62].

A typical swept-source laser consists of a semiconductor gain medium within a cavity with a tunable wavelength filter. Tunable wavelength filters for such lasers have been implemented in different ways: a Fabry-Perot filter [63], combination of a diffraction grating with a polygon mirror [64] or a galvanometer mirror [65] have been used to filter specific wavelengths. Several industrial research groups have implemented optical filters with MEMS components and demonstrated smaller swept-source lasers. Some of these lasers are summarized in Table 1.1.

**Table 1.1:** MEMS-based swept-source lasers, FP: Fabry–Perot

Company	Center $\lambda$ (nm)	Sweep rate (kHz)	Tuning range (nm)	Power (mW)	Technology
Santec	1060, 1300	100	100	20	MEMS scanning mirror and a grating as an optical filter [66].
Axsun	1060, 1300	100	100	15	MEMS FP filter and micro-optical components [67].
Exalos	1060, 1300	150	100	15	1D MEMS mirror and a micro grating [68].

In addition to these external cavity lasers, a MEMS-tunable, vertical-cavity surface-emitting laser (VCSEL) with micron-scale cavity length has been developed by Praevium Research, Inc. Their laser has low mirror mass for high sweep speeds, single-mode operation without mode hops, and long dynamic coherence length. The tunable VCSEL centered at 1310 nm is fabricated by bonding a wide-gain, indium phosphide (InP)-based quantum-well active region to a gallium arsenide (GaAs)-based oxidized mirror. An electrostatically actuated dielectric mirror suspended over the top of this structure tunes the emission wavelength

by changing the cavity length. The device is optically pumped by a 980 nm laser source. The average fiber-coupled output power of these lasers under full dynamic tuning is near 1 mW. Ophthalmic SS-OCT requires power levels on the order of 5–10 mW, which can be achieved using semiconductor optical amplification.

### 1.4.2 Integrated photonics for OCT

Significant miniaturization and cost reduction could be achieved through the use of compact integrated photonic components for OCT. Integrated photonic components are based on optical waveguides, where light is manipulated by changing the geometry and the refractive index of the optical waveguide structures. Integrated photonic devices are fabricated on planar substrates (e.g. semiconductor or dielectric crystal wafer) using similar technologies for electronic integrated circuit (EIC) manufacturing. Planar substrates are modified by using microfabrication methods such as photolithography, etching and deposition to define guided-wave devices. Integrated photonic devices such as waveguides, splitters, switches, modulators, spectrometers, lasers, SLEDs and photodetectors have been demonstrated. Integration of several of these devices on a single substrate have been also demonstrated using different material systems. The aim is to integrate more and more components on a single substrate, connected to each other via optical waveguides. The most obvious benefit of integration is the reduction in size, weight and cost that results from wafer-scale integration of photonic devices. Integration can also improve the robustness and stability of photonic systems by having a complete photonic integrated circuit (PIC) on a single substrate. Due to these benefits, realization of OCT devices through photonic integration would also increase its deployment in other application areas.

Although it may not be possible to realize all of them optimally on the same material system, different components can be combined on a substrate that is suitable to implement passive structures. Depending on the device, specific material systems are favored. For example, silica PICs are preferred for low-loss, thermally stable passive devices; compound semiconductor (e.g. GaAs, InP) PICs are efficient for light sources; silicon nitride ( $\text{Si}_3\text{N}_4$ ) PICs are transparent in the visible and infrared regions and permit moderately small waveguide bend radii and silicon PICs have the merit of being manufacturable in a CMOS fab.

One of the OCT components that can be integrated on a chip is the interferometer. Some research groups have already demonstrated inte-

grated interferometers for OCT using different material systems. Culeman et al. reported on parallel integration of eight Michelson interferometers implemented in glass [69]. Their design was used as part of a TD-OCT to image human skin. We demonstrated a Michelson interferometer implemented in silicon on insulator [70]. The sensitivity of that system was not sufficient for *in vivo* imaging. Recently, Nguyen et al. fabricated a Michelson interferometer using  $\text{Si}_3\text{N}_4$  and silicon dioxide ( $\text{SiO}_2$ ) waveguides and was used in an SS-OCT system to obtain an image of an *in vitro* tissue phantom [71]. In another study, Akca et al. demonstrated a beam splitter and an arrayed waveguide grating on chip for OCT in silicon oxynitride ( $\text{SiON}$ ) [72]. Although the waveguides in those studies are sufficiently low loss to implement a long reference arm, none of these four designs had a sufficiently long on-chip reference arm to compensate the optical path length of an x-y scanner. Therefore, they used an external reference arm or required scanning of the sample or the chip to obtain an image. Recently, we reported on two photonic integrated circuits for OCT; one was based on  $\text{Si}_3\text{N}_4$  and  $\text{SiO}_2$  waveguides [73] and the other was based on silicon on insulator (SOI) waveguides [74]. The PIC based on  $\text{Si}_3\text{N}_4$  and  $\text{SiO}_2$  waveguides consisted of splitters and a 190 mm long reference arm. It was used as the core of a spectral-domain OCT system consisting of a superluminescent diode centered at 1320 nm, a spectrometer with 1024 channels, and a galvanometric x-y scanner. Using the system, we imaged human skin *in vivo*. The PIC based on SOI had a similar design to the previous one but with much smaller footprint. The chip consisted of three  $2 \times 2$  splitters, a 13 cm physical length (50.4 cm optical length) reference arm and grating couplers. It was used as the interferometer of a SS-OCT system. Using the system, we demonstrated cross-sectional OCT imaging of a layered tissue phantom.

The aforementioned studies are based on passive photonic integrated circuits. Further integration approaches of active devices such as light sources and detectors will open a road towards fully integrated OCT systems.

### 1.4.3 Companies commercializing integrated photonics for OCT

The possibility of using integrated photonics to miniaturize OCT has also received interest from few start-ups to commercialize OCT systems or components utilizing this technology. Currently, there are two such



**Figure 1.12:** NITID, portable OCT imaging device for dermatology from DermaLumics. (image obtained from DermaLumics website [76])

companies which have a product on the market. One of the companies is Medlumics (Madrid, Spain). Founded in 2009, they have recently released a hand-held diagnostic device that combines epiluminescence microscopy and OCT imaging. An image of their device, which is called NITID, is shown in Figure 1.12. They have spun-out a new company named DermaLumics in 2015 which continues to develop and promote this device. Based on one of their patents [75], it seems that it is a TD-OCT, using an integrated photonic interferometer with an integrated delay line.

Another company which has a product in the field of integrated photonics for OCT is Tornado Spectral Systems (Toronto, Canada). In 2013, they released OCTANE-860, a fully packaged, turn-key spectrometer for OCT, centered at 860 nm. The dispersive elements in the spectrometer are implemented using integrated photonic components. A schematic diagram of OCTANE-860 is given in Figure 1.13.

OCTANE-860 has an FC/APC fiber interface. The device contains a polarization beam splitter (PBS) connected to two dispersive elements on a planar lightwave circuit (PLC) chip. PLC is another term used for photonic integrated circuit. The first 1024 pixels of the linear array (LA) read out the TE (transverse electric) polarization, and the second 1024 pixels read out the orthogonal TM (transverse magnetic) polarization. The measurement bandwidth of the spectrometer is 70 nm and the dispersion of the spectrometer is 0.068 nm/pix at 860 nm. With these parameters, it can provide 9.6  $\mu\text{m}$  axial resolution in air.

There is also a company called Compact Imaging (Mountain View, CA, USA) working on a miniature TD-OCT utilizing multiple reference arms [78]. However, they do not have a product on the market yet. As the technology matures and the market grows, it is likely that more

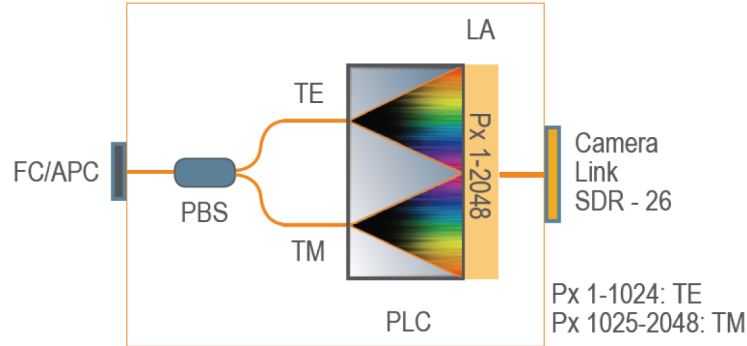


**Figure 1.13:** Schematic diagram of OCTANE-860 spectrometer from Tornado Spectral Systems. PBS: polarizing beam splitter, TE: transverse electric, TM: transverse magnetic, PLC: planar lightwave circuit, LA: linear array.(image obtained from the website of Tornado Spectral Systems [77])

companies will emerge in this domain.

## 1.5 Challenges and outline

In this thesis, the aim is to explore passive photonic integrated circuits towards miniaturized OCT. Most of the effort was spent designing PICs based on SOI technology, while we also investigated a design based on box-shaped  $\text{Si}_3\text{N}_4$  and silicon dioxide  $\text{SiO}_2$  (TriPleX<sup>TM</sup>) waveguides.

During the research within the context of this thesis, we came across several challenges. The initial designs with SOI were based on Michelson interferometer configuration. The roughness on the sidewall of a waveguide scatters the light in all directions and is mostly radiated away, but some of it scatters backward in the waveguide. In Michelson configuration, backscattering due to the sidewall roughness in the sample and reference arm waveguides can degrade the system performance in high refractive index contrast waveguides. As a solution to this problem, in later designs, we used a Mach-Zehnder configuration in our interferometers.

The return loss of individual components in a photonic integrated circuit for OCT is crucial. The return loss of optical components which are connected to each other with fibers do not present a significant problem if the fiber length is much longer than the coherence length of the

light source. However, the distances between individual components in a photonic integrated chip are in the order of the coherence length of OCT light sources. Thus, fringes due to reflections within the chip may appear as spurious background signals in the OCT signal. To avoid this, the transitions between different photonic integrated components need to be sufficiently smooth to reduce such reflection effects. Reflections may also result at the edge of the chip, while coupling the light in and out of the chip. In order to reduce such reflections, we used angled grating couplers for the SOI designs and angle polished waveguides for the TriPleX<sup>TM</sup> designs.

The axial resolution of OCT depends on the source bandwidth, thus optical components of an OCT system should support a sufficiently broad bandwidth. Directional couplers and MMI (multimode interference) splitters, which are commonly used in our research group, are not sufficiently broadband for OCT. A solution for  $1 \times 2$  splitters is to use y-splitters. For  $2 \times 2$  splitters we designed an adiabatic coupler, which is a modified directional coupler consisting of waveguides of varying widths rather than conventional uniform waveguides. Although such couplers are several times longer than general directional couplers, they can be designed to have flat 50:50 splitting ratios over 200 nm bandwidth.

Although we demonstrated OCT imaging using the chip-based system, the sensitivity and axial resolution are relatively low compared to state-of-the art OCT systems. However, the sensitivity and the axial resolution can be significantly improved using more advanced fabrication methods to fabricate fiber-to-chip coupling structures with lower insertion loss and larger bandwidth. Simple grating couplers used in our design are easy to fabricate but are not the optimum solution. By using more advanced fabrication processes, grating couplers with 1.6 dB loss and 80 nm 3 dB bandwidth have been demonstrated [79] For even larger bandwidths, a solution is to use horizontal butt-coupling using spot size converters to couple the light in and out of the chip.

This thesis is organized as follows.

In Chapter 2, we go through the theory of OCT. After introducing the fundamentals of spectral interferometry, we explain OCT parameters such as axial and lateral resolution, imaging depth range, sensitivity fall-off, and dispersion effects.

In Chapter 3, design of the 1300 nm, SOI based Mach-Zehnder interferometer is discussed. Additionally, design and characterization of an adiabatic coupler is covered. Experimental results obtained with the SS-OCT system using this chip are presented.

In Chapter 4, we present the design of the 1300 nm, TriPleX™ based OCT chip. *in vivo* human skin images obtained with the SD-OCT system utilizing this chip are presented.

In Chapter 5, the design of a 208 channel spectrometer with 0.15 nm channel spacing in SOI is presented. The spectrometer architecture is based on cascaded ring resonators and AWGs together with heaters to shift the spectral response of the ring resonators. The measurement set-up and the characterization of the spectrometer is discussed.

In Chapter 6, we present the general conclusions of the studies constituting the thesis and discuss potential future work and directions towards a truly portable, integrated-photonics-based OCT systems.

## 1.6 Publications

### Publications in international journals

1. G. Yurtsever, N. Weiss, J. Kalkman, T.G. van Leeuwen, R. Baets. *Ultra-compact silicon photonic integrated interferometer for swept-source optical coherence tomography*. Optics letters, 39(17), p.5228-5231 (2014)
2. G. Yurtsever, B. Považay, A. Alex, B. Zabihian, W. Drexler, R. Baets. *Photonic integrated Mach-Zehnder interferometer with an on-chip reference arm for optical coherence tomography*. Biomedical Optics Express, 5(4), p.1050-1061 (2014).
3. Y. Li, S. Verstuyft, G. Yurtsever, S. Keyvaninia, G. Roelkens, D. Van Thourhout and R. Baets. *Heterodyne laser Doppler vibrometers integrated on silicon-on-insulator with thermo-optic based frequency shifters*. Applied Optics, 52(10), p.2145-2152 (2013).
4. Y. Li, D. Vermeulen, Y. De Koninck, G. Yurtsever, G. Roelkens, R. Baets. *OCT supports industrial nondestructive depth analysis*. Optics Letters, 37(21), p.4356-4358 (2012).

### Publications in magazines

1. P. Merken, R. Vandersmissen and G. Yurtsever. *OCT supports industrial nondestructive depth analysis*. Laser Focus World, 47(8), p.82 (2011)

**Publications in international conferences**

1. Y. Li, S. Verstuyft, G. Yurtsever, S. Keyvaninia, G. Roelkens, D. Van Thourhout and R. Baets. *Miniaturized laser Doppler vibrometers integrated on silicon-on-insulator with thermo-optic serrodyne optical frequency shifter*. 9th International Conference on Group IV Photonics, United States, p.219-221 (2012).
2. Y. Li, D. Vermeulen, Y. De Koninck, G. Yurtsever, G. Roelkens and R. Baets. *Fiber couplers for silicon-on-insulator photonic IC*. Optical Fiber Communication Conference (OFC) 2012, p.JTh2A.8 (2012)
3. G. Yurtsever and R. Baets. *Integrated spectrometer on silicon on insulator*. Proceedings of the 16th Annual Symposium of the IEEE Photonics Benelux Chapter, Belgium, p.273-276 (2011).
4. G. Yurtsever, K. Komorowska, R. Baets. *Integrated photonic circuit in silicon on insulator for Fourier-domain optical coherence tomography*. Conference on Optical Coherence Tomography and Coherence Techniques V, 8091(80910T), Germany, (2011).
5. G. Yurtsever, K. De Vos, T. Claes, P.P.P. Debackere, P. Bienstman and R. Baets. *Photonic Biosensors in Silicon-on-Insulator*. 2nd International Conference On Silicon Photonics (invited), United States, (2010).
6. G. Yurtsever, P. Dumon, W. Bogaerts, R. Baets. *Integrated photonic circuit in silicon on insulator for Fourier-domain optical coherence tomography*. Proceedings of SPIE Photonics West 2010-BIOS: Biomedical Optics, 7554, United States, p.75541B (5 pages) (2010).
7. G. Yurtsever, J. Brouckaert, W. Bogaerts, P. Dumon, D. Van Thourhout and R. Baets. *Compact demultiplexer using cascaded planar concave grating and ring resonators on SOI* The 22nd Annual Meeting of the IEEE Photonics Society, Turkey, (2009).
8. G. Yurtsever and R. Baets. *Towards integrated optical coherence tomography system on silicon on insulator*. Proceedings Annual Symposium of the IEEE/LEOS Benelux Chapter, Netherlands, p.163-166 (2008).



## References

- [1] D. Huang, E. A. Swanson, C. P. Lin, J. S. Schuman, W. G. Stinson, W. Chang, M. R. Hee, T. Flotte, K. Gregory, C. A. Puliafito, *et al.*, “Optical coherence tomography”, *Science*, vol. 254, no. 5035, pp. 1178–1181, 1991 (cit. on pp. 1, 6).
- [2] M. Adhi and J. S. Duker, “Optical coherence tomography—current and future applications”, *Current opinion in ophthalmology*, vol. 24, no. 3, p. 213, 2013 (cit. on pp. 1, 4).
- [3] W. Drexler and J. G. Fujimoto, “Optical coherence tomography: technology and applications”, in, Springer, 2008, ch. 1 (cit. on p. 3).
- [4] T. Yonetsu, B. E. Bouma, K. Kato, J. G. Fujimoto, and I.-K. Jang, “Optical coherence tomography—15 years in cardiology.”, *Circulation journal: official journal of the Japanese Circulation Society*, vol. 77, no. 8, pp. 1933–1940, 2013 (cit. on p. 4).
- [5] T. Gambichler, V. Jaedicke, and S. Terras, “Optical coherence tomography in dermatology: technical and clinical aspects”, *Archives of dermatological research*, vol. 303, no. 7, pp. 457–473, 2011 (cit. on p. 4).
- [6] T. S. Kirtane and M. S. Wagh, “Endoscopic optical coherence tomography (oct): advances in gastrointestinal imaging”, *Gastroenterology research and practice*, vol. 2014, 2014 (cit. on p. 4).
- [7] R. Hou, T. Le, S. D. Murgu, Z. Chen, and M. Brenner, “Recent advances in optical coherence tomography for the diagnoses of lung disorders”, *Expert review of respiratory medicine*, vol. 5, no. 5, pp. 711–724, 2011 (cit. on p. 4).
- [8] Y.-S. Hsieh, Y.-C. Ho, S.-Y. Lee, C.-C. Chuang, J.-c. Tsai, K.-F. Lin, and C.-W. Sun, “Dental optical coherence tomography”, *Sensors*, vol. 13, no. 7, pp. 8928–8949, 2013 (cit. on p. 4).
- [9] M. Wojtkowski, “High-speed optical coherence tomography: basics and applications”, *Applied Optics*, vol. 49, no. 16, pp. D30–D61, 2010 (cit. on p. 4).
- [10] S.-H. Kim, J.-H. Kim, and S.-W. Kang, “Nondestructive defect inspection for lcds using optical coherence tomography”, *Displays*, vol. 32, no. 5, pp. 325–329, 2011 (cit. on p. 6).

- 
- [11] D. Stifter, “Beyond biomedicine: a review of alternative applications and developments for optical coherence tomography”, *Applied Physics B*, vol. 88, no. 3, pp. 337–357, 2007 (cit. on p. 4).
- [12] K. Takada, I. Yokohama, K. Chida, and J. Noda, “New measurement system for fault location in optical waveguide devices based on an interferometric technique”, *Applied Optics*, vol. 26, no. 9, pp. 1603–1606, 1987 (cit. on p. 6).
- [13] B. L. Danielson and C. Whittenberg, “Guided-wave reflectometry with micrometer resolution”, *Applied Optics*, vol. 26, no. 14, pp. 2836–2842, 1987 (cit. on p. 6).
- [14] R. C. Youngquist, S. Carr, and D. E. Davies, “Optical coherence-domain reflectometry: a new optical evaluation technique”, *Optics Letters*, vol. 12, no. 3, pp. 158–160, 1987 (cit. on p. 6).
- [15] Optovue, 2015, <http://www.optovue.com> (cit. on p. 8).
- [16] G. Tearney, B. Bouma, and J. Fujimoto, “High-speed phase-and group-delay scanning with a grating-based phase control delay line”, *Optics Letters*, vol. 22, no. 23, pp. 1811–1813, 1997 (cit. on p. 8).
- [17] W. Drexler and J. G. Fujimoto, “Optical coherence tomography: technology and applications”, in, Springer, 2008, ch. 19 (cit. on p. 9).
- [18] A. Dubois, K. Grieve, G. Moneron, R. Lecaque, L. Vabre, and C. Boccara, “Ultrahigh-resolution full-field optical coherence tomography”, *Applied Optics*, vol. 43, no. 14, pp. 2874–2883, 2004 (cit. on p. 9).
- [19] M. Jain, N. Narula, B. Salamoon, M. M. Shevchuk, A. Aggarwal, N. Altorki, B. Stiles, C. Boccara, and S. Mukherjee, “Full-field optical coherence tomography for the analysis of fresh unstained human lobectomy specimens”, *Journal of pathology informatics*, vol. 4, 2013 (cit. on p. 10).
- [20] B. B. et al., “Optical frequency domain imaging”, in *Optical coherence tomography: technology and applications*, W. Drexler and J. G. Fujimoto, Eds., Springer Science and Business Media, 2008 (cit. on pp. 11–12).
- [21] P. Andretzky, M. W. Lindner, J. M. Herrmann, A. Schultz, M. Konzog, F. Kiesewetter, and G. Haeusler, “Optical coherence tomography by spectral radar: dynamic range estimation and in-vivo measurements of skin”, in *BiOS Europe ’98*, International Society for Optics and Photonics, 1999, pp. 78–87 (cit. on pp. 12, 15).
- [22] T. Mitsui, “Dynamic range of optical reflectometry with spectral interferometry”, *Japanese journal of applied physics*, vol. 38, no. 10R, p. 6133, 1999 (cit. on pp. 12, 15).
- [23] R. Leitgeb, C. Hitzenberger, and A. Fercher, “Performance of fourier domain vs. time domain optical coherence tomography”, *Optics Express*, vol. 11, no. 8, pp. 889–894, 2003 (cit. on pp. 12, 16).

- [24] J. F. De Boer, B. Cense, B. H. Park, M. C. Pierce, G. J. Tearney, and B. E. Bouma, “Improved signal-to-noise ratio in spectral-domain compared with time-domain optical coherence tomography”, *Optics letters*, vol. 28, no. 21, pp. 2067–2069, 2003 (cit. on pp. 12, 16).
- [25] M. Choma, M. Sarunic, C. Yang, and J. Izatt, “Sensitivity advantage of swept source and fourier domain optical coherence tomography”, *Optics Express*, vol. 11, no. 18, pp. 2183–2189, 2003 (cit. on pp. 12, 16–17).
- [26] W. Drexler and J. G. Fujimoto, “Optical coherence tomography: technology and applications”, in, Springer, 2008, ch. 2 (cit. on p. 13).
- [27] M. A. Choma, K. Hsu, and J. A. Izatt, “Swept source optical coherence tomography using an all-fiber 1300-nm ring laser source”, *Journal of biomedical optics*, vol. 10, no. 4, pp. 044 009–044 009, 2005 (cit. on p. 13).
- [28] W.-C. Kuo, C.-M. Lai, Y.-S. Huang, C.-Y. Chang, and Y.-M. Kuo, “Balanced detection for spectral domain optical coherence tomography”, *Optics express*, vol. 21, no. 16, pp. 19 280–19 291, 2013 (cit. on p. 13).
- [29] D. J. Faber and T. G. van Leeuwen, “Optical coherence tomography”, in *Optical-Thermal Response of Laser-Irradiated Tissue*, Springer, 2011, pp. 713–742 (cit. on pp. 14–15).
- [30] B. Považay, B. Hermann, A. Unterhuber, B. Hofer, H. Sattmann, F. Zeiler, J. E. Morgan, C. Falkner-Radler, C. Glittenberg, S. Blinder, *et al.*, “Three-dimensional optical coherence tomography at 1050nm versus 800nm in retinal pathologies: enhanced performance and choroidal penetration in cataract patients”, *Journal of biomedical optics*, vol. 12, no. 4, pp. 041 211–041 211, 2007 (cit. on p. 14).
- [31] J. A. Goldsmith, Y. Li, M. R. Chalita, V. Westphal, C. A. Patil, A. M. Rollins, J. A. Izatt, and D. Huang, “Anterior chamber width measurement by high-speed optical coherence tomography”, *Ophthalmology*, vol. 112, no. 2, pp. 238–244, 2005 (cit. on p. 14).
- [32] Michelson Diagnostics , 2015, <http://www.vivosight.com> (cit. on p. 14).
- [33] A. Alex, B. Považay, B. Hofer, S. Popov, C. Glittenberg, S. Binder, and W. Drexler, “Multispectral in vivo three-dimensional optical coherence tomography of human skin”, *Journal of biomedical optics*, vol. 15, no. 2, pp. 026 025–026 025, 2010 (cit. on p. 14).
- [34] H. Kawagoe, S. Ishida, M. Aramaki, Y. Sakakibara, E. Omoda, H. Kataura, and N. Nishizawa, “Development of a high power supercontinuum source in the 1.7 um wavelength region for highly penetrative ultrahigh-resolution optical coherence tomography”, *Biomedical optics express*, vol. 5, no. 3, pp. 932–943, 2014 (cit. on p. 15).
- [35] H. Liang, R. Lange, B. Peric, and M. Spring, “Optimum spectral window for imaging of art with optical coherence tomography”, *Applied Physics B*, vol. 111, no. 4, pp. 589–602, 2013 (cit. on p. 15).

- [36] A. F. Fercher, C. K. Hitzenberger, G. Kamp, and S. Y. El-Zaiat, “Measurement of intraocular distances by backscattering spectral interferometry”, *Optics Communications*, vol. 117, no. 1, pp. 43–48, 1995 (cit. on p. 15).
- [37] G. Hausler, M. W. Lindner, *et al.*, ““coherence radar” and “spectral radar”—new tools for dermatological diagnosis”, *Journal of Biomedical Optics*, vol. 3, no. 1, pp. 21–31, 1998 (cit. on p. 15).
- [38] N. Nassif, B. Cense, B. Hyle Park, S. H. Yun, T. C. Chen, B. E. Bouma, G. J. Tearney, and J. F. d. Boer, “In vivo human retinal imaging by ultrahigh-speed spectral domain optical coherence tomography”, *Optics letters*, vol. 29, no. 5, pp. 480–482, 2004 (cit. on p. 16).
- [39] B. Cense, N. Nassif, T. Chen, M. Pierce, S.-H. Yun, B. Park, B. Bouma, G. Tearney, and J. de Boer, “Ultrahigh-resolution high-speed retinal imaging using spectral-domain optical coherence tomography”, *Optics Express*, vol. 12, no. 11, pp. 2435–2447, 2004 (cit. on p. 16).
- [40] M. Wojtkowski, V. Srinivasan, T. Ko, J. Fujimoto, A. Kowalczyk, and J. Duker, “Ultrahigh-resolution, high-speed, fourier domain optical coherence tomography and methods for dispersion compensation”, *Optics express*, vol. 12, no. 11, pp. 2404–2422, 2004 (cit. on p. 16).
- [41] W. Drexler and J. G. Fujimoto, “State-of-the-art retinal optical coherence tomography”, *Progress in retinal and eye research*, vol. 27, no. 1, pp. 45–88, 2008 (cit. on p. 17).
- [42] W. Eickhoff and R. Ulrich, “Optical frequency domain reflectometry in single-mode fiber”, *Applied Physics Letters*, vol. 39, no. 9, pp. 693–695, 1981 (cit. on p. 16).
- [43] U. Glombitza and E. Brinkmeyer, “Coherent frequency-domain reflectometry for characterization of single-mode integrated-optical waveguides”, *Lightwave Technology, Journal of*, vol. 11, no. 8, pp. 1377–1384, 1993 (cit. on p. 16).
- [44] B. Soller, D. Gifford, M. Wolfe, and M. Froggatt, “High resolution optical frequency domain reflectometry for characterization of components and assemblies”, *Optics Express*, vol. 13, no. 2, pp. 666–674, 2005 (cit. on p. 16).
- [45] J. Müller, M. Krause, and E. Brinkmeyer, “Spatially resolved loss measurement in silicon waveguides using optical frequency-domain reflectometry”, *Electronics Letters*, vol. 47, no. 11, pp. 668–670, 2011 (cit. on p. 16).
- [46] S. Chinn, E. Swanson, and J. Fujimoto, “Optical coherence tomography using a frequency-tunable optical source”, *Optics letters*, vol. 22, no. 5, pp. 340–342, 1997 (cit. on p. 17).
- [47] B. Golubovic, B. Bouma, G. Tearney, and J. Fujimoto, “Optical frequency-domain reflectometry using rapid wavelength tuning of a  $\text{Cr}^{4+}$ :forsterite laser”, *Optics Letters*, vol. 22, no. 22, pp. 1704–1706, 1997 (cit. on p. 17).

- [48] S. Yun, G. Tearney, J. de Boer, N. Iftimia, and B. Bouma, “High-speed optical frequency-domain imaging”, *Optics Express*, vol. 11, no. 22, pp. 2953–2963, 2003 (cit. on p. 18).
- [49] W.-Y. Oh, S. H. Yun, G. J. Tearney, and B. E. Bouma, “115 khz tuning repetition rate ultrahigh-speed wavelength-swept semiconductor laser”, *Optics letters*, vol. 30, no. 23, pp. 3159–3161, 2005 (cit. on p. 18).
- [50] W.-Y. Oh, B. J. Vakoc, M. Shishkov, G. J. Tearney, and B. E. Bouma, “> 400 khz repetition rate wavelength-swept laser and application to high-speed optical frequency domain imaging”, *Optics letters*, vol. 35, no. 17, pp. 2919–2921, 2010 (cit. on p. 18).
- [51] R. Huber, M. Wojtkowski, and J. Fujimoto, “Fourier domain mode locking (fdml): a new laser operating regime and applications for optical coherence tomography”, *Optics Express*, vol. 14, no. 8, pp. 3225–3237, 2006 (cit. on p. 18).
- [52] R. Huber, D. C. Adler, and J. G. Fujimoto, “Buffered fourier domain mode locking: unidirectional swept laser sources for optical coherence tomography imaging at 370,000 lines/s”, *Optics letters*, vol. 31, no. 20, pp. 2975–2977, 2006 (cit. on p. 18).
- [53] W. Wieser, B. R. Biedermann, T. Klein, C. M. Eigenwillig, and R. Huber, “Multi-megahertz oct: high quality 3d imaging at 20 million a-scans and 4.5 gvoxels per second”, *Optics express*, vol. 18, no. 14, pp. 14685–14704, 2010 (cit. on p. 18).
- [54] V. Jayaraman, D. John, C. Burgner, M. Robertson, B. Potsaid, J. Jiang, T. Tsai, W. Choi, C. Lu, P. Heim, *et al.*, “Recent advances in mems-vcsls for high performance structural and functional ss-oct imaging”, in *SPIE BiOS*, International Society for Optics and Photonics, 2014, pp. 893402–893402 (cit. on p. 18).
- [55] S. Moon and D. Y. Kim, “Ultra-high-speed optical coherence tomography with a stretched pulse supercontinuum source”, *Optics express*, vol. 14, no. 24, pp. 11575–11584, 2006 (cit. on p. 18).
- [56] K. Goda, A. Fard, O. Malik, G. Fu, A. Quach, and B. Jalali, “High-throughput optical coherence tomography at 800 nm”, *Optics express*, vol. 20, no. 18, pp. 19612–19617, 2012 (cit. on p. 18).
- [57] D. Choi, H. Hiro-Oka, H. Furukawa, R. Yoshimura, M. Nakanishi, K. Shimizu, and K. Ohbayashi, “Fourier domain optical coherence tomography using optical demultiplexers imaging at 60,000,000 lines/s”, *Optics letters*, vol. 33, no. 12, pp. 1318–1320, 2008 (cit. on p. 18).
- [58] C. D. Lu, M. F. Kraus, B. Potsaid, J. J. Liu, W. Choi, V. Jayaraman, A. E. Cable, J. Hornegger, J. S. Duker, and J. G. Fujimoto, “Handheld ultrahigh speed swept source optical coherence tomography instrument using a mems scanning mirror”, *Biomedical optics express*, vol. 5, no. 1, pp. 293–311, 2014 (cit. on p. 19).

- [59] D. Wang, P. Liang, S. Samuelson, H. Jia, J. Ma, and H. Xie, “Correction of image distortions in endoscopic optical coherence tomography based on two-axis scanning mems mirrors”, *Biomedical optics express*, vol. 4, no. 10, pp. 2066–2077, 2013 (cit. on p. 19).
- [60] B. Y. Yeo, R. A. McLaughlin, R. W. Kirk, and D. D. Sampson, “Enabling freehand lateral scanning of optical coherence tomography needle probes with a magnetic tracking system”, *Biomedical optics express*, vol. 3, no. 7, pp. 1565–1578, 2012 (cit. on p. 20).
- [61] N. Weiss, T. G. van Leeuwen, and J. Kalkman, “Doppler-based lateral motion tracking for optical coherence tomography”, *Optics letters*, vol. 37, no. 12, pp. 2220–2222, 2012 (cit. on p. 20).
- [62] N. Iftimia, G. Maguluri, E. W. Chang, S. Chang, J. Magill, and W. Brugge, “Hand scanning optical coherence tomography imaging using encoder feedback”, *Optics Letters*, vol. 39, no. 24, pp. 6807–6810, 2014 (cit. on p. 20).
- [63] R. Huber, M. Wojtkowski, K. Taira, J. Fujimoto, and K. Hsu, “Amplified, frequency swept lasers for frequency domain reflectometry and oct imaging: design and scaling principles”, *Optics Express*, vol. 13, no. 9, pp. 3513–3528, 2005 (cit. on p. 20).
- [64] S.-H. Yun, C. Boudoux, G. J. Tearney, and B. E. Bouma, “High-speed wavelength-swept semiconductor laser with a polygon-scanner-based wavelength filter”, *Optics letters*, vol. 28, no. 20, pp. 1981–1983, 2003 (cit. on p. 20).
- [65] R. Huber, M. Wojtkowski, J. G. Fujimoto, J. Jiang, and A. Cable, “Three-dimensional and c-mode oct imaging with a compact, frequency swept laser source at 1300 nm”, *Optics Express*, vol. 13, no. 26, pp. 10 523–10 538, 2005 (cit. on p. 20).
- [66] B. Vuong, C. Sun, M. K. Harduar, A. Mariampillai, K. Isamoto, C. Chong, B. A. Standish, and V. X. Yang, “23 khz mems based swept source for optical coherence tomography imaging”, in *Engineering in Medicine and Biology Society, EMBC, 2011 Annual International Conference of the IEEE, IEEE*, 2011, pp. 6134–6137 (cit. on p. 20).
- [67] M. Kuznetsov, W. Atia, B. Johnson, and D. Flanders, “Compact ultrafast reflective fabry-perot tunable lasers for oct imaging applications”, in *BiOS, International Society for Optics and Photonics*, 2010, 75541F–75541F (cit. on p. 20).
- [68] Exalos , 2015, [http://http://www.exalos.com](http://www.exalos.com) (cit. on p. 20).
- [69] D. Culemann, A. Knuettel, and E. Voges, “Integrated optical sensor in glass for optical coherence tomography (oct)”, *Selected Topics in Quantum Electronics, IEEE Journal of*, vol. 6, no. 5, pp. 730–734, 2000 (cit. on p. 22).

- [70] G. Yurtsever, P. Dumon, W. Bogaerts, and R. Baets, “Integrated photonic circuit in silicon on insulator for fourier domain optical coherence tomography”, in *BiOS*, International Society for Optics and Photonics, 2010, 75541B–75541B (cit. on p. 22).
- [71] V. D. Nguyen, N. Weiss, W. Beeker, M. Hoekman, A. Leinse, R. Heidemann, T. van Leeuwen, and J. Kalkman, “Integrated-optics-based swept-source optical coherence tomography”, *Optics letters*, vol. 37, no. 23, pp. 4820–4822, 2012 (cit. on p. 22).
- [72] B. Akca, B. Považay, A. Alex, K. Wörhoff, R. de Ridder, W. Drexler, and M. Pollnau, “Miniature spectrometer and beam splitter for an optical coherence tomography on a silicon chip”, *Optics express*, vol. 21, no. 14, pp. 16 648–16 656, 2013 (cit. on p. 22).
- [73] G. Yurtsever, B. Považay, A. Alex, B. Zabihian, W. Drexler, and R. Baets, “Photonic integrated mach-zehnder interferometer with an on-chip reference arm for optical coherence tomography”, *Biomedical optics express*, vol. 5, no. 4, pp. 1050–1061, 2014 (cit. on p. 22).
- [74] G. Yurtsever, N. Weiss, J. Kalkman, T. G. van Leeuwen, and R. Baets, “Ultra-compact silicon photonic integrated interferometer for swept-source optical coherence tomography”, *Optics letters*, vol. 39, no. 17, pp. 5228–5231, 2014 (cit. on p. 22).
- [75] J. L. R. GUIVERNAU and E. M. BALBÁS, *Integrated delay line for optical coherence tomography*, US Patent App. 14/129,367, 2012 (cit. on p. 23).
- [76] Dermalumics , 2015, <http://www.dermalumics.com> (cit. on p. 23).
- [77] Tornado Spectral Systems, 2015, <http://tornado-spectral.com> (cit. on p. 24).
- [78] K. Neuhaus, H. Subhash, R. Dsouza, J. Hogan, C. Wilson, and M. Leahy, “Signal simulation and signal processing for multiple reference optical coherence tomography”, in *SPIE BiOS*, International Society for Optics and Photonics, 2015, pp. 931 236–931 236 (cit. on p. 23).
- [79] D. Vermeulen, S. Selvaraja, P. Verheyen, G. Lepage, W. Bogaerts, P. Absil, D. Van Thourhout, and G. Roelkens, “High-efficiency fiber-to-chip grating couplers realized using an advanced cmos-compatible silicon-on-insulator platform”, *Optics express*, vol. 18, no. 17, pp. 18 278–18 283, 2010 (cit. on p. 25).



# 2

## Theory of optical coherence tomography

In this thesis, we investigate how optical coherence tomography (OCT) can benefit from integrated photonics technology to realize smaller, cheaper systems. In order to make such an investigation, it is necessary to understand the theoretical and practical aspects of OCT. As we mentioned in Chapter 1, current state-of-the-art OCT systems are implemented as FD-OCT due to its advantages in speed and sensitivity over TD-OCT. In this chapter, we focus only on Fourier-domain OCT (FD-OCT) theory [1], [2] and skip the theory of time-domain OCT (TD-OCT) [3]. All photonics integrated circuits in our work have been designed for FD-OCT. In the following sections, we explain OCT image formation and key OCT parameters, such as resolution, imaging depth, sensitivity, sensitivity fall-off, and dispersion effects.

### 2.1 Fourier-domain OCT

The principle of FD-OCT is based on spectral interferometry, where depth information is obtained by analyzing the spectral interference of a sample arm and a reference arm. As we explained in the Introduction chapter, an FD-OCT system can be implemented in two different ways:

spectral-domain OCT (SD-OCT) and swept-source OCT (SS-OCT). In SD-OCT, the spectral interference is measured using a broadband light source and a spectrometer. On the other hand, in SS-OCT the spectral interference is measured using a swept-source (tunable) laser and a photodetector. To derive the equations related to OCT image formation in FD-OCT, we use SD-OCT as a working example. An SD-OCT diagram is shown in Figure 2.1. In SD-OCT, light from a broadband light source is split into two arms by a splitter. The beam in the sample arm is focused on the tissue and the light in the reference arm is sent to a fixed mirror. The back-reflected light from multiple layers within the tissue is collected with the same focusing optics and interferes with the light reflecting from the fixed mirror in the reference arm. The interference signal is dispersed by a spectrometer into its spectral components. The spectrum is detected with a 1D photodetector array (line scan camera) in the spectrometer. The Fourier transform of the measured spectral interference provides the depth-resolved reflectivity profile of the sample, which is called A-scan. By scanning the beam laterally over the sample, 2D cross-sectional and 3D volumetric images are obtained by stitching the A-scans. Below, we derive the equations which show how an A-scan can be obtained from the spectral interference.

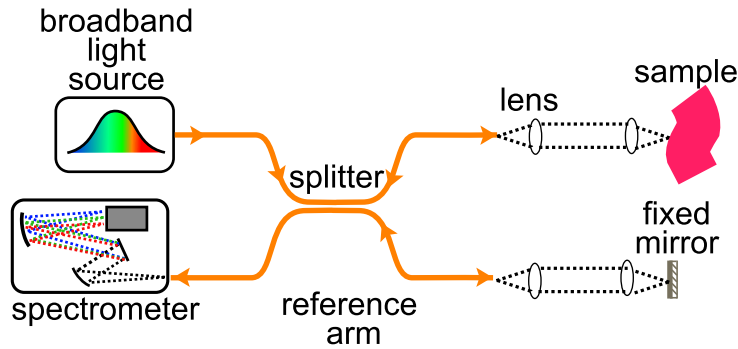


**Figure 2.1:** Schematic diagram of spectral-domain OCT.

For the sake of simplicity in derivations, we will make some assumptions. We assume that the reference arm and sample arm electric fields (E-fields) have the same spectral profile; same polarization; the optical components are lossless and wavelength independent; zero delay line is above the sample surface and the sample arm consists of the same guiding medium with the reference arm so that there is no dispersion mismatch. The last two assumptions related to the path lengths and

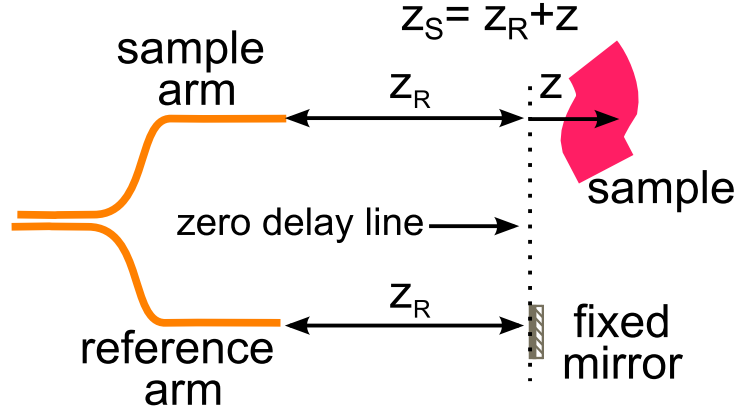


**Figure 2.2:** Diagram of the sample and reference arms to explain the notation used to define their path lengths.

the zero delay line position are depicted in Figure 2.2. Derivations with similar assumptions can be found in [4] and [5].

We can write the path length of the sample arm,  $z_S$ , as

$$z_S = z_R + z \quad (2.1)$$

where  $z_R$  is the path length of the common parts of the reference and the sample arms and  $z$  is the path length after the zero delay line. Here, we assume that until the zero delay line the reference and sample arms are identically constructed; they have the same path length  $z_R$  and the same wavenumber  $k_R$ .

In frequency domain, the E-fields of the reference arm and the sample arm can be represented as

$$E_R(\omega) = r_R E_0(\omega) \exp(i2k_R(\omega)z_R) \quad (2.2)$$

$$E_S(\omega) = E_0(\omega) \exp(i2k_R(\omega)z_R) \int_0^{+\infty} r_S(z) \exp(2k_S(\omega)z) dz \quad (2.3)$$

Here, subscripts  $R$  and  $S$  denote the reference and sample arms, respectively;  $E_0(\omega)$  denotes the envelope of the electric field;  $k_R(\omega)$  and  $k_S(\omega)$  denote the wavenumbers;  $r_R$  denotes the amplitude reflectivity of the reference mirror;  $r_S(z)$  denotes the depth-resolved reflectivity profile of the sample. We assume that  $r_R$  and  $r_S(z)$  are real. Since the zero delay

line is above the sample surface,  $r_S(z)$  is zero for  $z \leq 0$ . For that reason, the lower limit of the integral starts from zero. The first term in Eq. 2.3 refers to the sample arm before the zero delay line and the integral term refers to the sample arm after the zero delay line.

Apart from a constant scaling factor, the intensity of the interference observed at the spectrometer is given by

$$I(k) = |E_R(k) + E_S(k)|^2 \quad (2.4)$$

where  $k$  is the wavenumber in vacuum. Writing the equation as a function of  $k$  ( $k = \omega/c$ ) rather than  $\omega$  (angular frequency) simplifies the expressions. Let  $S(k) = |E_0(k)|^2$ , then we have

$$\begin{aligned} I(k) = & S(k)r_R^2 + S(k)r_R \int_0^{+\infty} r_S(z)\exp(i2kn_S z)dz \\ & + S(k)r_R \int_0^{+\infty} r_S(z)\exp(-i2kn_S z)dz \\ & + S(k) \left| \int_0^{+\infty} r_S(z)\exp(i2kn_S z)dz \right|^2 \end{aligned} \quad (2.5)$$

after combining the 2nd and 3rd terms, and explicitly writing the last term, we obtain

$$\begin{aligned} I(k) = & S(k) \left[ r_R^2 + 2r_R \int_0^{+\infty} r_S(z)\cos(2kn_S z)dz \right. \\ & \left. + \int_0^{+\infty} \int_0^{+\infty} r_S(z)r_S(z')\exp[-i2kn_S(z-z')] dzdz' \right] \end{aligned} \quad (2.6)$$

Since we assumed that the zero delay line is above the sample surface, we can do a small mathematical trick, and define a function  $\hat{r}_S(z)$  that is symmetric around zero:  $\hat{r}_S(z) = \hat{r}_S(-z) = r_S(z)$ . By replacing  $r_S(z)$  with  $\hat{r}_S(z)$  in the previous equation, we can write  $I(k)$  as

$$I(k) = S(k) \left[ r_R^2 + r_R \int_{-\infty}^{+\infty} \hat{r}_S(z) \cos(2kn_S z) dz + \frac{1}{4} \int_{-\infty}^{+\infty} \int_{-\infty}^{+\infty} \hat{r}_S(z) \hat{r}_S(z') \exp[-i2kn_S(z-z')] dz dz' \right] \quad (2.7)$$

In the 3rd term in Eq. 2.7, we can use the following autocorrelation notation used in OCT literature

$$AC[\hat{r}_S(z)] = \int_{-\infty}^{\infty} \hat{r}_S(z) \hat{r}_S(z') \exp(i2kn_S z') dz' \quad (2.8)$$

Using the autocorrelation notation above and the fact that  $\sin$  is an odd function for the 2nd term in Eq. 2.7, we can write  $I(k)$  as

$$I(k) = S(k) \left[ r_R^2 + r_R \int_{-\infty}^{+\infty} \hat{r}_S(z) \exp(-i2kn_S z) dz + \frac{1}{4} \int_{-\infty}^{+\infty} AC[\hat{r}_S(z)] \exp(-i2kn_S z) dz \right] \quad (2.9)$$

Then, with a change of variable by

$$\hat{z} = 2n_S z \quad (2.10)$$

we can write the expression as

$$I(k) = S(k) \left[ r_R^2 + \frac{r_R}{2n_S} F \left\{ \hat{r}_S \left( \frac{\hat{z}}{2n_S} \right) \right\} + \frac{1}{16n_S^2} F \left\{ AC \left[ \hat{r}_S \left( \frac{\hat{z}}{2n_S} \right) \right] \right\} \right] \quad (2.11)$$

where  $F$  denotes Fourier transform. By inverse Fourier transforming both sides of Eq. (2.11), we obtain the following expression

$$F^{-1} \{I(k)\}(\hat{z}) = F^{-1} \{S(k)\}(\hat{z}) \otimes \left[ r_R^2 \delta(\hat{z}) + \frac{r_R}{2n_S} \hat{r}_S\left(\frac{\hat{z}}{2n_S}\right) + \frac{1}{16n_S^2} AC \left[ \hat{r}_S\left(\frac{\hat{z}}{2n_S}\right) \right] \right] \quad (2.12)$$

where  $F^{-1}$  denotes inverse Fourier transform and  $\otimes$  denotes convolution. The second term in the sum is what we are looking for: the depth-resolved reflectivity profile of the sample. The first and the last terms in the sum are unwanted terms. The first term is a DC term due to the reference beam. This DC term can be removed by blocking the sample arm ( $r_S = 0$ ), recording the data, and then subtracting it from the measured data. This is called background subtraction. The last term,  $AC$ , is the autocorrelation of the sample reflectivity and can overlap with the second term. The autocorrelation term can be removed by different techniques [6], [7]. However, its amplitude is much smaller than the reflectivity profile, and its effect may not be significant. The convolution term in front of the expression determines the axial resolution.

In principle, the axial resolution can be improved by linear deconvolution; simply by dividing both sides in Eq. (2.11) by  $S(k)$ . Then we obtain

$$F^{-1} \left\{ \frac{I(k)}{S(k)} \right\}(\hat{z}) = r_R^2 \delta(\hat{z}) + \frac{r_R}{2n_S} \hat{r}_S\left(\frac{\hat{z}}{2n_S}\right) + \frac{1}{16n_S^2} AC \left[ \hat{r}_S\left(\frac{\hat{z}}{2n_S}\right) \right] \quad (2.13)$$

However, the noise level in typical OCT data is high and limits the effectiveness of linear convolution.

The calculations to obtain an A-scan from the spectral interference in SS-OCT is the same as in SD-OCT. Once the interference spectrum is obtained as a function of  $k$ , in theory, there is no difference in data processing. While explaining the characteristic parameters of FD-OCT in the next sections, we will compare some practical aspects of SD-OCT and SS-OCT.

## 2.2 Resolution

The optical sectioning capability of OCT is similar to confocal microscope systems. Using the confocal approximation, transverse (lateral) resolution in OCT is determined by the numerical aperture of the focusing lens and is given by the following expression [8]:

$$\Delta xy = 0.37 * \frac{\lambda_0}{NA} \quad (2.14)$$

where  $\lambda_0$  is the center wavelength of the light source and NA is the numerical aperture of the focusing lens, assuming it is properly filled. Derivations of the detected intensity from a point scatterer in an OCT system as a function of lateral and axial positions can be found in [9], [10].

Although the axial (longitudinal) resolution of confocal microscopy depends on the available numerical aperture, OCT's resolution is determined by the bandwidth of the light source provided that the optical components in the system (e.g splitters) are sufficiently broadband. Thus, the axial and lateral resolutions of OCT are decoupled from each other.

We will briefly derive the expression for the axial resolution in OCT. A Gaussian spectrum, centered at  $k_0$  with standard deviation  $\sigma_k$  can be written as

$$S(k) = |E(k)|^2 = \frac{1}{\sigma_k \sqrt{2\pi}} e^{-(k-k_0)^2/2\sigma_k^2} \quad (2.15)$$

From Eq. (2.11) we see that the Fourier transform of  $S(k)$  with respect to  $\hat{z}$  gives us the axial resolution.

$$\begin{aligned} F \{S(k)\} (\hat{z}) &= \int_{-\infty}^{+\infty} S(k) e^{-ik\hat{z}} dk \\ &= \frac{1}{\sigma_k \sqrt{2\pi}} \int_{-\infty}^{+\infty} e^{-(k-k_0)^2/2\sigma_k^2} e^{-ik\hat{z}} dk \\ &= e^{-i\hat{z}k_0} e^{-\frac{1}{2}\sigma_k^2 \hat{z}^2} \end{aligned} \quad (2.16)$$

We can write the equation as of function of z using Eq. 2.10

$$F \{S(k)\} (z) = e^{-i2nz k_0} e^{-\frac{1}{2}\sigma_k^2 4n^2 z^2} \quad (2.17)$$

Using the following relation between FWHM (full width at half maximum) and standard deviation,  $\sigma$ ,

$$\text{FWHM} = 2\sqrt{2\ln 2}\sigma \quad (2.18)$$

and the relation between  $k$  and  $\lambda$ , we can express  $\sigma_k$  in terms of  $\Delta\lambda$  as

$$\Delta k_{FWHM} = 2\sqrt{2\ln 2}\sigma_k = 2\pi \frac{\Delta\lambda}{\lambda_0^2} \quad (2.19)$$

where  $\lambda_0$  is the center wavelength and  $\Delta\lambda$  is the FWHM of the spectral envelope. Leaving  $\sigma_k$  alone on the left side yields

$$\sigma_k = \frac{\pi}{\sqrt{2\ln(2)}} \frac{\Delta\lambda}{\lambda_0^2} \quad (2.20)$$

Using the relation between  $\sigma_k$  and  $\Delta\lambda$  in Eq. (2.20) and the final expression in Eq. (2.16), we obtain the FWHM of  $F\{S(k)\}(z)$  as

$$FWHM_z = 2\sqrt{2\ln 2} \frac{1}{2\sigma_k} = \frac{2\ln 2}{\pi} \frac{\lambda_0^2}{\Delta\lambda} \quad (2.21)$$

The axial resolution in OCT is usually denoted by  $\Delta z$ , and for a light source with a Gaussian-profile spectral envelope it is  $FWHM_z$  and we can write  $\Delta z$  as

$$\Delta z = \frac{2\ln 2}{\pi} \frac{\lambda_0^2}{\Delta\lambda} \quad (2.22)$$

For simplicity, we derived the axial resolution in air. For a sample with dispersion,  $\Delta z$  is further divided by its group index  $n_g$  [11].

The axial resolution in OCT is inversely proportional to the bandwidth of the light source, while dependence on the center wavelength is quadratic. In Figure 2.3, axial resolution in air as a function of source bandwidth is given for center wavelengths 800 nm and 1300 nm. Using a light source centered at 800 nm, 10  $\mu\text{m}$  resolution can be obtained with 30 nm FWHM light source, while it requires 75 nm FWHM light source centered at 1300 nm. .

The actual depth-resolved reflectivity profile of the sample is convolved with a Gaussian function of FWHM of  $\delta z$  (Eq. (2.11)). Deviation from Gaussian spectral profile may further degrade the axial resolution and create sidelobes. These side lobes can be suppressed by reshaping the spectrum before its Fourier transform is calculated [12]. In a noiseless ideal system, deconvolution can be used to obtain much higher axial

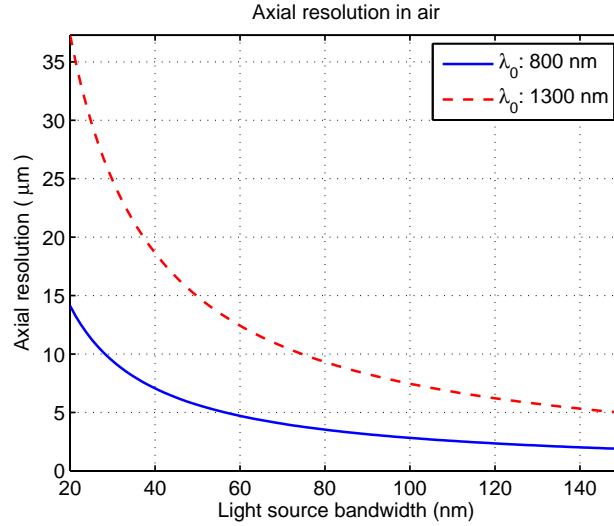


**Figure 2.3:** Dependence of axial resolution in OCT on light source bandwidth.

resolution, however, in real noisy systems, simple deconvolution does not work well. More complex deconvolution algorithms for axial resolution improvement in OCT have been proposed [13], [14].

## 2.3 Imaging range

In Fourier-domain OCT, the spectral profile of the interference is sampled in  $k$ -space and then Fourier transformed to obtain a depth-resolved reflectivity profile of the sample. If the spectral interference is sampled with a period of  $\delta k$  and Fourier transformed, based on the Nyquist theorem, the maximum  $\hat{z}$  value on the  $\hat{z}$ -axis will be  $1/(2F_s) = 2\pi/(2\delta k)$ . Thus, the maximum measurable path length difference between the reference and sample arms in FD-OCT is given by

$$\hat{z}_{\max} = \frac{2\pi}{2\delta k} \quad (2.23)$$

Using the following relation between  $k$  and  $\lambda$ , we can write  $\delta k$ , the sampling period in wavenumber, as

$$\begin{aligned}\delta k &= \frac{2\pi}{\lambda_1} - \frac{2\pi}{\lambda_2} \\ &= \frac{2\pi\delta\lambda}{\lambda_0^2}\end{aligned}\tag{2.24}$$

where  $\delta\lambda$  is the sampling period in wavelength and  $\lambda_0$  is the center wavelength. Then, by substituting  $\delta k$  from Eq. (2.24) to Eq. (2.23),  $\hat{z}_{\max}$  can be expressed in wavelength as

$$\hat{z}_{\max} = \frac{\lambda_0^2}{2\delta\lambda}\tag{2.25}$$

However, in order to find the physical distance, we need to use the relation  $\hat{z} = 2nz$ , which was defined in Eq. (2.10). After change of variables, we obtain the maximum possible imaging depth as

$$z_{\max} = \frac{\lambda_0^2}{4n\delta\lambda}\tag{2.26}$$

Here, we derived the maximum possible imaging depth for a sample without dispersion. For a sample with dispersion, the refractive index in the equation above is replaced by the group index ( $n_g$ ) of the sample [11].

In SD-OCT,  $\delta\lambda$  is the channel spacing of the spectrometer, while in SS-OCT the sampling period of the spectrum is determined by the sweep rate of the laser and the analog-to-digital sampling rate of the photodetector output.

Based on Eq. (2.26), the imaging ranges vs. sampling period for center wavelengths of 800 nm and 1300 nm are plotted in Figure 2.4. For the same sampling period, larger center wavelengths provide a higher imaging range.

We should note that the imaging depth is also limited by scattering and absorption properties of the sample as we discussed in Section 1.2.3. For example, at 1300 nm, human skin can be imaged only 1-2 mm deep due to the highly scattering nature of skin tissue.

## 2.4 Sensitivity

The sensitivity of an OCT instrument is the critical factor in determining image quality, penetration depth, and image acquisition speed. In OCT, sensitivity is defined as the signal-to-noise ratio for a perfect sample reflector [15]. Shot noise limited sensitivity [16] is given by the following

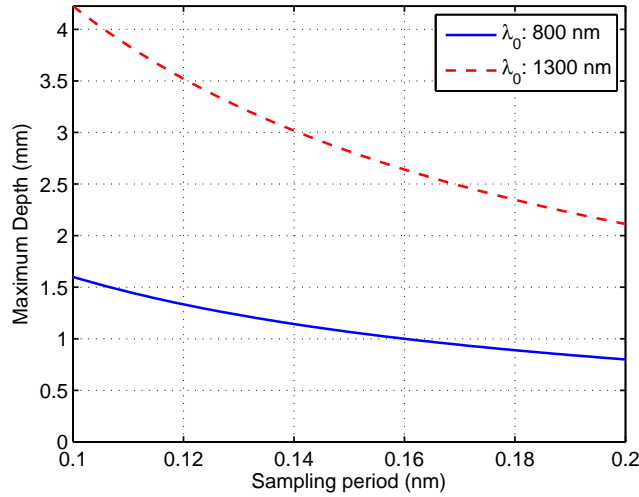


**Figure 2.4:** Imaging range in FD-OCT as a function of sampling period in wavelength.

formula

$$\text{Sensitivity}_{\text{shot}} [\text{dB}] = 20 \log_{10} \left( \frac{\eta P_{\text{sample}} \tau_i}{E_\nu} \right)^{1/2} \quad (2.27)$$

where  $P_{\text{sample}}$  is the power received from the sample arm,  $\eta$  is the quantum efficiency of the photodetector,  $\tau_i$  is the integration time, and  $E_\nu$  is the photon energy.

In practice, the sensitivity of an OCT system is found experimentally by inserting a neutral density filter (typically OD2 - OD3) into the sample arm and measuring the reflection from a mirror. The OCT signal from the mirror reflection is found and looks like the one shown in Figure 2.5. Then the ratio of the reflection peak to the standard deviation of the noise floor is calculated and the signal loss due to attenuation is added. The experimental sensitivity is defined as

$$\text{Sensitivity} [\text{dB}] = 20 \log_{10} \frac{\text{max signal}}{\text{std of noise}} + 20 * OD \quad (2.28)$$

The  $20 * OD$  term is to compensate the attenuation of the neutral density filter. The reason for using  $20 \log_{10}$  rather than  $10 \log_{10}$  is: here the ratio is signal/noise rather than signal<sup>2</sup>/noise<sup>2</sup>.

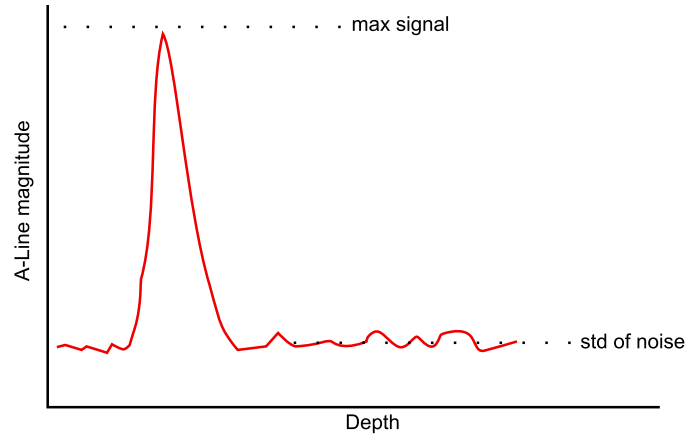


**Figure 2.5:** Measuring sensitivity in an OCT system, both axes are in linear scale.

Typical values of state of the art commercial and research instruments have sensitivities around 90-100 dB for 50 kHz axial acquisition speed, with 1 mW power on the sample. Due to the losses in the optical elements, analog to digital converter (ADC) noise, electronics and light source noise, measured sensitivity values are generally  $\sim 10$  dB lower than the shot noise limited sensitivity.

## 2.5 Linear sampling in k-space

In addition to the fundamental principles of FD-OCT, explained in the sections above, there are few practical factors affecting OCT imaging. One of them is sampling the spectral interference linearly (uniformly) in wavenumber (k-space). As seen in Eq. (2.9),  $\hat{z}$  and  $k$  are Fourier transform pairs. In order to use the efficient FFT algorithm to obtain an A-scan, it is necessary that the optical spectrum is sampled linearly in  $k$ . In SD-OCT, usually a spectrometer disperses the light linearly in wavelength rather than in wavenumber. In SS-OCT, the sweep rate of the laser may not be linear in k-space. Non-linear mapping in k-space leads to depth-dependent broadening of the point spread function (PSF), thus axial resolution and sensitivity will degrade with increasing depth [17]. Mapping of the measured spectrum from linear  $\lambda$ -space to linear k-space in a spectrometer based OCT is typically performed by a separate measurement of a reflective surface (mirror) placed in the

sample arm. The interference from a reflective surface is a sinusoidal function and its phase can be retrieved. Phase retrieval is usually done by finding the zero crossings or using Hilbert transform [18]. By fitting a high order polynomial to the phase data, the spectrum is resampled by interpolating the data for linearly spaced phase points.

Linear sampling in  $k$ -space can also be done by designing a spectrometer with spectral dispersion that is linear in wavenumber [19]. Similar linear-in-wavenumber dispersion has also been reported using compound prism designs [20].

In SS-OCT systems, to sample the spectrum linearly in  $k$ -space, part of the laser output can be split and sent to a Fabry-Perot or Mach-Zehnder interferometer to generate a trigger signal that is used as the sampling clock of the ADC card [21], [22]. This trigger signal samples the spectrum in evenly spaced  $k$  points, thus the data can be Fourier transformed without any resampling.

## 2.6 Signal fall-off

Another practical aspect in OCT is the signal fall-off. Signal fall-off, also referred as sensitivity fall-off, is the attenuation of the OCT signal due to decrease in fringe visibility with increasing depth. In other words, the higher the frequency of the fringes, the lower the fringe visibility. This effect is mainly due to the spectral extent integrated by a pixel of the detector array of the spectrometer and is also a function of the spectrometer resolution. We briefly derive an expression for the signal fall-off, assuming that the spectrum is sampled evenly in  $k$ -space. The details of the derivation can be found in [23].

The spectrum measured with a spectrometer can be approximated by a convolution between the spectrometer's spectral transfer function,  $T(k)$ , and the true intensity spectrum,  $I(k)$ . Then, the intensity in the detector plane can be written in  $k$ -space as  $T(k) \otimes I(k)$  where  $k$  is the wavenumber.  $T(k)$  depends on the spectrometer characteristics, such as focal length, diffraction grating, and entrance-slit width. Since the detector array has a finite pixel width, the convolved light intensity in the detector plane is then integrated over the pixel area, yielding the following expression for the signal  $S_i$ , collected on a given pixel at position  $x_i$ .

$$\begin{aligned}
S_i &= \int_{x_i-a/2}^{x_i+a/2} T(k) \otimes I(k) dk \\
&= \int_{-\infty}^{+\infty} R(k - k_i) [T(k) \otimes I(k)] dk \\
&= [R(k) \otimes T(k) \otimes I(k)](k_i)
\end{aligned} \tag{2.29}$$

where  $a$  is the pixel width,  $R(k)$  is a rectangle (rect) function with unit amplitude for  $|k| < a/2$  and zero elsewhere. The general form of the signal  $S$  can be represented as function of  $k$  as

$$S(k) = D(k) [R(k) \otimes T(k) \otimes I(k)] \tag{2.30}$$

where  $D(k)$  is a Dirac comb of period  $\delta k$ , the pixel spacing. Depth-resolved reflectivity profile of the sample is obtained by taking the Fourier transform of this signal, and is given by

$$S_f(z) = D_f(z) \otimes [R_f(z) T_f(z) I_f(z)] \tag{2.31}$$

$D(z)$ ,  $R_f(z)$ ,  $T_f(z)$  and  $I_f(z)$  are Fourier transforms of  $D(k)$ ,  $R(k)$ ,  $T(k)$  and  $I(k)$  respectively. Here,  $R_f(z)$  is a sinc function. From the expression above, we see that both pixel width and spectrometer resolution affect the spectral intensity as low-pass filters [23]. In general, the spectrometer impulse response  $T(k)$  is narrower than  $R(k)$  and  $R_f(z)$  is the dominant low-pass filter. Thus, the result of the integration of light over a rectangular pixel is a low-pass filter which is a sinc function. A more detailed derivation of a signal fall-off expression for SD-OCT is presented by Hu et al. [19].

All of these discussions on pixel spacing, pixel width and spectrometer resolution also apply to SS-OCT. There, pixel spacing corresponds to ADC sampling rate, pixel width corresponds to sample and hold time of the ADC card, and spectrometer resolution corresponds to linewidth of the source.

## 2.7 Dispersion

Dispersion effects arise due to the frequency dependence of refractive indices of the materials in the sample and reference arms. The broader the bandwidth of the light source, the more significant the effect of dispersion. In OCT, when the sample and reference arms contain different

lengths of optical fiber or other dispersive media (e.g lenses, tissue), dispersion mismatch occurs. The dispersion imbalance between the two arms of the interferometer can be minimized by inserting extra optical glass with the necessary dispersion properties. The effect of dispersion in OCT is broadening of the axial point spread function and decrease of its amplitude. Assuming a Gaussian light source, the axial resolution is broadened by a factor of

$$\sqrt{1 + (\Delta k'' \sigma_\omega^2)^2} \quad (2.32)$$

where,  $\Delta k''$  is the 2nd order phase mismatch between sample and reference arms, such that  $\Delta k'' = k_S'' z_S - k_R'' z_R$  with  $k_S''$  and  $k_R''$  are 2nd order terms in the Taylor expansion of wavenumber  $k$  of sample and reference arms:

$$k(\omega) = k(\omega_0) + k'(\omega - \omega_0) + \frac{1}{2}k''(\omega - \omega_0)^2 + \dots \quad (2.33)$$

$k''$  is also referred as the group velocity dispersion (GVD). It is usually given in units of  $\text{fs}^2/\text{cm}$ .  $z_S$  and  $z_R$  are lengths traveled by light in the sample and reference arms. The  $\sigma_\omega$  term is the standard deviation of the Gaussian light source.

The degradation in the amplitude of the OCT signal is described by the following multiplicative factor

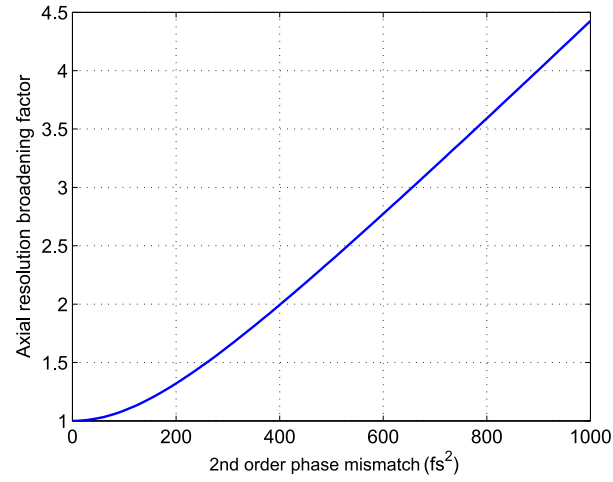
$$\frac{1}{\left[1 + (\Delta k'' \sigma_\omega^2)^2\right]^{1/4}} \quad (2.34)$$

The derivations of both Eqs. (2.32) and (2.34) are given in appendix A.

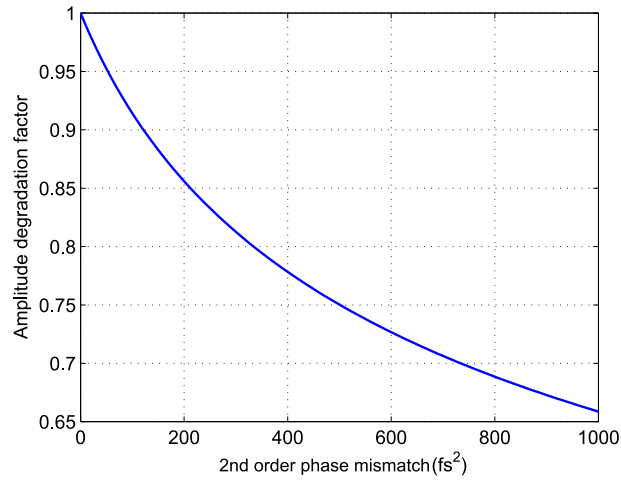
Glass has a GVD around  $500 \text{ fs}^2 \text{ cm}^{-1}$  for a center wavelength of 1300 nm. Thus, 1 cm of glass will cause  $500 \text{ fs}^2$  of second order phase accumulation. Axial resolution broadening and amplitude degradation are plotted in Figures 2.6a and 2.6b for different amounts of 2nd order phase mismatch. In these plots, the light source was assumed to have a Gaussian spectrum with 100 nm FWHM and center wavelength of 1300 nm.

### Dispersion compensation

Dispersion effects in OCT can be compensated in software by canceling the phase mismatch related term. The interferometric signal has the form of



(a)



(b)

**Figure 2.6:** The effect of 2<sup>nd</sup> order dispersion mismatch in OCT. (a) Broadening of the axial resolution due to dispersion mismatch. (b) Degradation of point spread function amplitude due to dispersion mismatch

$$S(\omega) = S_0(\omega) \cos(\omega \Delta \tau_g + \Delta \phi(\omega)) \quad (2.35)$$

where,  $\Delta\tau_g$  is group delay mismatch between the two arms. The phase of the interference signal can be extracted by writing it in its analytic form as

$$\begin{aligned}\tilde{S}(\omega) &= S_0(\omega) \exp [i\Delta\Phi(\omega)] \\ &= S_0(\omega) \exp [i(\omega\Delta\tau_g + \Delta\phi(\omega))] \\ &= S_0(\omega) \cos [\omega\Delta\tau_g + \Delta\phi(\omega)] + iS_0(\omega) \sin [\omega\Delta\tau_g + \Delta\phi(\omega)]\end{aligned}\quad (2.36)$$

The derivation of the dispersion effect on the OCT signal and the phase term  $\Delta\Phi(\omega)$  are given in appendix A). We can find  $S_0(\omega) \sin(\omega\Delta\tau_g + \Delta\phi(\omega))$  by using the fact that it is the Hilbert transform of  $S_0(\omega) \cos(\omega\Delta\tau_g + \Delta\phi(\omega))$ . Then, the phase of the analytical signal is given by:

$$\phi(t) = \arctan \left( \frac{\cos [\omega\Delta\tau_g + \Delta\phi(\omega)]}{\sin [\omega\Delta\tau_g + \Delta\phi(\omega)]} \right) \quad (2.37)$$

In practice, a reflection from a reflective surface is measured to obtain a clean sinusoidal interference signal. After background subtraction is performed, we calculate the Hilbert transform (e.g. Matlab's `x = hilbert(xr)` function) of the data to obtain its analytical signal. From the analytical signal, we extract the phase (e.g. using Matlab's `angle` function) [24] and fit a polynomial to it. Later, when we acquire data for OCT imaging, we calculate the analytical signal of the data and multiply it with the inverse phase, using the coefficients of the polynomial fit  $\exp(-i\Delta\phi(\omega)_{fit})$ . The order of the polynomial can be determined by checking whether the axial resolution improves by increasing the polynomial order. Typically 3rd order polynomial fit provides a significant improvement, if there is any dispersion mismatch.

If the sample dispersion changes significantly for each measurement (e.g. different people have different eye lengths), iterative dispersion correction algorithm that measures and optimizes the sharpness of the image can be used to find the polynomial coefficients for the phase [24]. In such an iterative algorithm, dispersion coefficients obtained by the methods described in the above paragraph can be used as initial values.

## 2.8 Conclusion

State-of-the-art OCT systems are quite demanding in terms of optimization in every aspect. To build an OCT system with high-sensitivity

and real-time 3D imaging capabilities, it is necessary to have a thorough understanding of its theory and practical aspects. Even from the fundamental aspects presented in this chapter, we can see that OCT technology is an intersection of optical design, biomedical optics, signal processing, electronics and software. Thus, it requires collaboration of people with knowledge in these fields to improve this technology further.

# References

- [1] W. Drexler and J. G. Fujimoto, “Optical coherence tomography: technology and applications”, in, Springer, 2008, ch. 2,5,7 (cit. on p. 37).
- [2] M. Wojtkowski, “High-speed optical coherence tomography: basics and applications”, *Applied Optics*, vol. 49, no. 16, pp. D30–D61, 2010 (cit. on p. 37).
- [3] J. M. Schmitt, “Optical coherence tomography (oct): a review”, *Selected Topics in Quantum Electronics, IEEE Journal of*, vol. 5, no. 4, pp. 1205–1215, 1999 (cit. on p. 37).
- [4] G. Hausler, M. W. Lindner, *et al.*, ““coherence radar” and “spectral radar”—new tools for dermatological diagnosis”, *Journal of Biomedical Optics*, vol. 3, no. 1, pp. 21–31, 1998 (cit. on p. 39).
- [5] L. V. Wang and H.-i. Wu, “Biomedical optics: principles and imaging”, in. John Wiley & Sons, 2012, ch. 9, pp. 199–202 (cit. on p. 39).
- [6] J. Ai and L. V. Wang, “Spectral-domain optical coherence tomography: removal of autocorrelation using an optical switch”, *Applied physics letters*, vol. 88, no. 11, p. 111115, 2006 (cit. on p. 42).
- [7] R. K. Wang and Z. Ma, “A practical approach to eliminate autocorrelation artefacts for volume-rate spectral domain optical coherence tomography”, *Physics in medicine and biology*, vol. 51, no. 12, p. 3231, 2006 (cit. on p. 42).
- [8] W. Drexler and J. G. Fujimoto, “Optical coherence tomography: technology and applications”, in, Springer, 2008, ch. 2 (cit. on p. 43).
- [9] S. Yun, G. Tearney, J. De Boer, and B. Bouma, “Motion artifacts in optical coherence tomography with frequency-domain ranging”, *Optics Express*, vol. 12, no. 13, pp. 2977–2998, 2004 (cit. on p. 43).
- [10] N. Weiss, T. G. van Leeuwen, and J. Kalkman, “Localized measurement of longitudinal and transverse flow velocities in colloidal suspensions using optical coherence tomography”, *Physical Review E*, vol. 88, no. 4, p. 042312, 2013 (cit. on p. 43).
- [11] B. B. et al., “Optical frequency domain imaging”, in *Optical coherence tomography: technology and applications*, W. Drexler and J. G. Fujimoto, Eds., Springer Science and Business Media, 2008 (cit. on pp. 44, 46).

- [12] J. Gong, B. Liu, Y. L. Kim, Y. Liu, X. Li, and V. Backman, “Optimal spectral reshaping for resolution improvement in optical coherence tomography”, *Optics express*, vol. 14, no. 13, pp. 5909–5915, 2006 (cit. on p. 44).
- [13] Y. Wang, Y. Liang, and K. Xu, “Signal processing for sidelobe suppression in optical coherence tomography images”, *JOSA A*, vol. 27, no. 3, pp. 415–421, 2010 (cit. on p. 45).
- [14] E. Bousi and C. Pitris, “Axial resolution improvement by modulated deconvolution in fourier domain optical coherence tomography”, *Journal of biomedical optics*, vol. 17, no. 7, pp. 071 307–071 307, 2012 (cit. on p. 45).
- [15] M. Choma, M. Sarunic, C. Yang, and J. Izatt, “Sensitivity advantage of swept source and fourier domain optical coherence tomography”, *Optics Express*, vol. 11, no. 18, pp. 2183–2189, 2003 (cit. on p. 46).
- [16] N. Nassif, B. Cense, B. Hyle Park, S. H. Yun, T. C. Chen, B. E. Bouma, G. J. Tearney, and J. F. d. Boer, “In vivo human retinal imaging by ultrahigh-speed spectral domain optical coherence tomography”, *Optics letters*, vol. 29, no. 5, pp. 480–482, 2004 (cit. on p. 46).
- [17] M. Wojtkowski, R. Leitgeb, A. Kowalczyk, A. F. Fercher, and T. Bajraszewski, “In vivo human retinal imaging by fourier domain optical coherence tomography”, *Journal of biomedical optics*, vol. 7, no. 3, pp. 457–463, 2002 (cit. on p. 48).
- [18] T.-J. Ahn, J. Y. Lee, and D. Y. Kim, “Suppression of nonlinear frequency sweep in an optical frequency-domain reflectometer by use of hilbert transformation”, *Applied optics*, vol. 44, no. 35, pp. 7630–7634, 2005 (cit. on p. 49).
- [19] Z. Hu and A. M. Rollins, “Fourier domain optical coherence tomography with a linear-in-wavenumber spectrometer”, *Optics letters*, vol. 32, no. 24, pp. 3525–3527, 2007 (cit. on pp. 49–50).
- [20] N. Hagen and T. S. Tkaczyk, “Compound prism design principles, iii: linear-in-wavenumber and optical coherence tomography prisms”, *Applied optics*, vol. 50, no. 25, pp. 5023–5030, 2011 (cit. on p. 49).
- [21] J. Zhang, W. Jung, J. Nelson, and Z. Chen, “Full range polarization-sensitive fourier domain optical coherence tomography”, *Optics Express*, vol. 12, no. 24, pp. 6033–6039, 2004 (cit. on p. 49).
- [22] W. Choi, B. Potsaid, V. Jayaraman, B. Baumann, I. Grulkowski, J. J. Liu, C. D. Lu, A. E. Cable, D. Huang, J. S. Duker, *et al.*, “Phase-sensitive swept-source optical coherence tomography imaging of the human retina with a vertical cavity surface-emitting laser light source”, *Optics letters*, vol. 38, no. 3, pp. 338–340, 2013 (cit. on p. 49).
- [23] C. Dorrer, N. Belabas, J.-P. Likforman, and M. Joffre, “Spectral resolution and sampling issues in fourier-transform spectral interferometry”, *JOSA B*, vol. 17, no. 10, pp. 1795–1802, 2000 (cit. on pp. 49–50).

- 
- [24] M. Wojtkowski, V. Srinivasan, T. Ko, J. Fujimoto, A. Kowalczyk, and J. Duker, “Ultrahigh-resolution, high-speed, fourier domain optical coherence tomography and methods for dispersion compensation”, *Optics express*, vol. 12, no. 11, pp. 2404–2422, 2004 (cit. on p. 53).



# 3

## Ultra-compact silicon photonic integrated interferometer with an on-chip reference arm for swept-source optical coherence tomography

As discussed in the Introduction chapter, optical coherence tomography (OCT) can benefit from photonic integration. Integrated photonics can enable low-cost and compact OCT systems that can widen their use in proven fields (e.g. ophthalmology) and open new opportunities for its deployment in other areas. We begin this chapter with a brief discussion of using photonic integration for OCT. Then, we provide a short background on silicon-based integrated photonics, namely silicon photonics. Here, we cover fabrication of silicon waveguides and integrated photonic components that can be used to design an integrated interferometer. After these introductory sections, we move to the main subject of this chapter: demonstration of OCT imaging using a silicon photonic integrated Mach-Zehnder interferometer. First, we discuss waveguide de-

sign for the integrated Mach-Zehnder interferometer. Next, we describe the integrated interferometer together with the swept-source OCT (SS-OCT) system built around it. Then, we present the axial resolution and sensitivity characterization of the SS-OCT system. Subsequently, we show an OCT image of a layered tissue phantom (an object with optical properties of tissue) obtained using the system. We conclude the chapter by discussing the challenges and potential improvements in silicon photonic integrated circuit design related to OCT imaging.

The work in this chapter was mainly done in collaboration with Prof. Ton G. van Leeuwen and Nicolas Weiss from Biomedical Engineering and Physics, Academic Medical Center, University of Amsterdam, The Netherlands. The experiments were carried out in the laboratory of Prof. Ton G. van Leeuwen under his guidance. Nicolas Weiss was instrumental in building the SS-OCT setup with the chip and in analyzing the data. We also had significant discussions related to the experimental setup and data processing with Prof. Jeroen Kalkman from the Department of Imaging Physics, Delft University of Technology, The Netherlands.

### 3.1 Integrated photonics and miniaturization of OCT

Current implementations of OCT systems are based on fiber and free-space optical components. Wafer-level integration of optical components has shown advantages in cost, size, stability and power efficiency for optical network technology [1]. Imaging applications like OCT can benefit from such photonic integration as well. Integrated photonics has the potential to enable mass production of OCT devices to significantly reduce size and cost, which can increase its use in established fields as well as enable new applications.

Photonic integrated circuits (PICs) are analogous to electronic integrated circuits (EICs) in a way that they implement multiple functions on a single substrate. The fabrication methods of PICs are similar to EICs, where devices are built on top of carrier substrates. The fabrication processes may include several steps like photolithography, etching, deposition, diffusion and doping.

The basic element of integrated photonics is the waveguide. Other components are usually built by introducing modifications to the waveguide structure such as changing the geometry and altering or actively manipulating the physical properties of the waveguide. Devices such as

splitters, filters, modulators, amplifiers, lasers, and detectors have been demonstrated in different materials systems [2].

Currently, optimal realization of a complex photonic system using a single material platform may not be possible; however, components implemented with different materials can be combined on a single substrate that is suitable to implement passive structures [3]. Choice of a material system depends on the device type. For example, for efficient light sources, compound semiconductor based materials such as GaAs and InP are used [4]–[7]; for low-loss, thermally stable passive devices, silica-based PICs are preferred [8]; for applications requiring transparency in the visible and/or infrared regions together with moderately small waveguide bend radii,  $\text{Si}_3\text{N}_4$  can be chosen as a material platform [9]; and for applications requiring large volume and low cost, silicon-based PICs are favorable as they can be manufactured in a CMOS fab benefiting from the existing infrastructure and know-how of silicon microelectronics industry. Silicon also provides the possibility of PICs with very small foot-print and integration with electronics [10]. Silicon is transparent for wavelengths larger than  $1.1\ \mu\text{m}$ .

Different material systems have been used to demonstrate photonic integrated components for OCT. Based on semiconductor materials, several types of integrated tunable lasers for SS-OCT have been reported: a MEMS-tunable vertical-cavity surface-emitting laser (VCSEL) [5]; an electrically tuned quantum-dot laser [7]; and a Vernier-tuned distributed Bragg reflector laser [11]. Using silica waveguides, Culeman et al. [12] demonstrated parallel integration of eight Michelson interferometers for time-domain OCT (TD-OCT). Silica arrayed waveguide gratings (AWGs) have been long used in optical fiber communication systems for wavelength division multiplexing, where individual wavelength channels are combined or separated. Choi et al. [13] reported an OCT system that uses a 256 channel, 25 GHz channel spacing, silica AWG as a spectrometer. Silicon oxynitride (SiON) was a material choice by Akca et al. [14] to demonstrate a beam splitter and an AWG on the same chip for spectral-domain OCT (SD-OCT). They imaged the output focal plane of their AWG directly onto a camera, so that the spectrum can be more densely sampled compared to an AWG with discrete output channels. Using  $\text{Si}_3\text{N}_4$  and silicon dioxide ( $\text{SiO}_2$ ) waveguides, Nguyen et al. fabricated a Michelson interferometer for SS-OCT [15]. Use of silicon waveguides for OCT was first demonstrated by Margallo-Balbas [16] by fabricating a thermo-optic delay line for TD-OCT. Recently, Schneider et al. [17] reported an integrated interferometer in silicon with on-chip germanium

detectors.

Among these designs mentioned above, none of them had a sufficiently long on-chip reference arm to compensate the optical path length of an x-y scanner. Therefore, they used an external reference arm or it required scanning of the sample or the chip to obtain an image. In this chapter, we present the design, characterization and application of a silicon integrated Mach-Zehnder interferometer with a long on-chip reference arm. It was used as the interferometer of an SS-OCT system with an x-y scanner by which we obtained images of a tissue phantom. Before we dive into the details of this study with the integrated interferometer, we present a short introduction on silicon photonics technology to clarify the design and fabrication of the interferometer, specifically for readers who are not familiar with integrated photonics technology.

## 3.2 Silicon photonics

In recent years, photonic integrated circuits based on silicon have gained substantial interest from the telecom industry. Silicon is one of the most developed material systems for microelectronic fabrication. Therefore, using silicon as a platform for photonic integrated circuits enables the use of existing CMOS infrastructure and processing know-how developed for silicon microelectronics fabrication. Wafer-scale, high-volume fabrication of silicon photonic integrated circuits using CMOS infrastructure [18] significantly reduces the price per chip. In addition, silicon waveguides have a very high confinement factor, which enables much smaller integrated photonic circuits than low-index-contrast material systems. Furthermore, several groups have demonstrated that active components such as lasers, photodetectors and modulators can be integrated on wafer-scale with silicon waveguides. A broad review of active component integration with silicon waveguides is presented by Park et al. [19]. In addition to active components, electronic and photonic integration can be combined on the same material system, which can further miniaturize electro-optical systems [20].

Compared to other integrated photonic material systems, silicon can have a significant potential for mass fabrication of OCT devices, which would result in miniaturization, cost reduction, and wider deployment. Multiple interferometers can also be fit on a single chip for parallel, faster OCT systems. Below, we briefly review the fabrication processes of silicon photonic components and basic building blocks such as waveguides, splitters and grating couplers used in this study.

### 3.2.1 Fabrication of waveguides

One of the fundamental processes used in wafer-scale microfabrication is the transfer of a pattern from a mask to a wafer. Figure 3.1 illustrates the major processing steps of pattern transfer using projection photolithography. The process starts by coating a wafer with a photosensitive material and is aligned under a mask which contains the desired pattern. A photosensitive material, usually termed as photoresist, is a substance that experiences a change in its chemical properties when exposed to light. Masks are usually made up of quartz (transparent to UV light) and chromium (opaque metal). The mask is typically illuminated with ultraviolet (UV) light and the pattern on the mask is projected on the photoresist. As a result of the exposure to light, the properties of the exposed and unexposed regions differs in their chemical composition. A baking process following the exposure step, catalyzes a reaction that changes the solubility of the exposed and unexposed regions. Once baked, subsequently the photoresist is developed; in other words, the wafer is placed in a chemical bath which dissolves the exposed regions. Then, liquid or a gas chemical that reacts and removes the device material is used for etching. The areas on the device material that are not protected by the photoresist are etched. After etching is finished, the resist is removed using special solvents and the transfer of the mask pattern to the wafer is complete.

In our study, we used silicon wafers that consists of silicon-insulator-silicon layers. This type of material is called silicon on insulator (SOI). The top silicon layer is a crystalline silicon device layer, separated from the bottom silicon substrate layer by a  $\text{SiO}_2$  (buried oxide) layer. The top silicon layer is used to fabricate optical waveguides and other photonic integrated devices. The buried oxide layer acts as a bottom cladding for the waveguides in the device layer. The bottom silicon layer is a supporting carrier substrate. The basic steps of fabricating a silicon waveguide on an SOI wafer is illustrated in Figure 3.2. First, the wafer is coated with a photoresist. The resist-coated wafers are then exposed under a mask which contains the waveguide pattern. After exposure, the wafer is baked and subsequently developed to remove the exposed resist. Then, the wafer is etched to transfer the pattern into the top silicon layer. Finally, the remaining resist is removed from the wafer. The resulting waveguide has a top air cladding and bottom  $\text{SiO}_2$  ( $n = 1.45$ ) cladding. This geometry creates a high-refractive-index contrast between the silicon core ( $n = 3.5$ ) and its claddings. High-index-contrast waveguides tightly confine the light in the core and allow for small bend

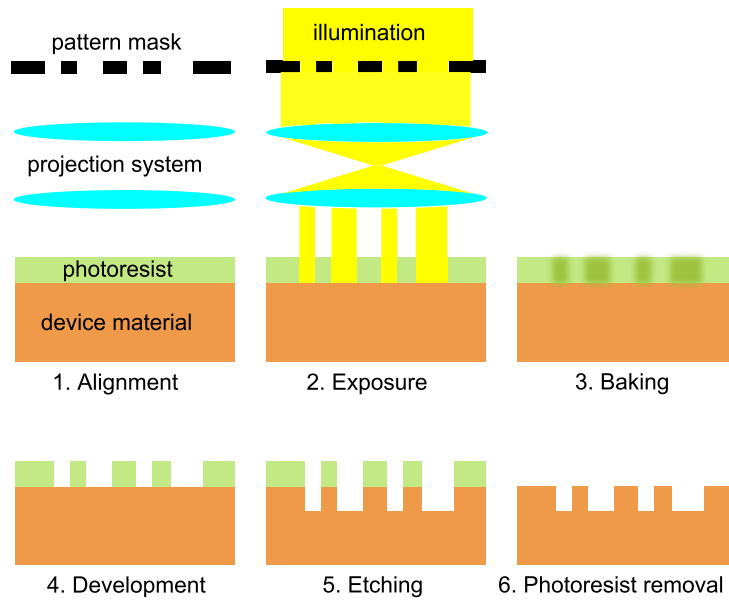


**Figure 3.1:** Patterning of a substrate using projection photolithography.

radii. The top of the waveguides can also be covered with other materials to enhance their functionality or protect them from contamination with dirt.

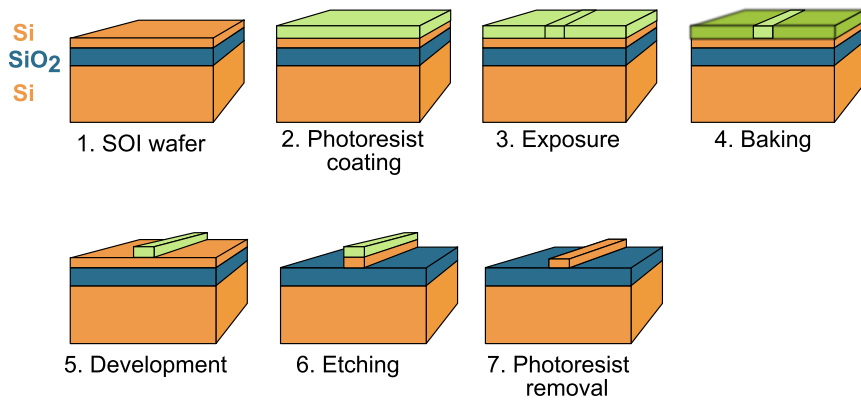


**Figure 3.2:** Fabrication process overview of a waveguide in SOI.

Wafer-scale fabrication in a CMOS facility has high fixed costs, which is usually compensated by high-volume production in industry. In order

to enable access to such facilities for research purposes at reasonable cost, a silicon photonics platform named ePIXfab has been established in Europe. ePIXfab organizes multi-project-wafer (MPW) fabrication runs for silicon photonic devices [21]. In these fabrication runs, designs from different contributors are combined on the same mask and are fabricated together in partner institutions' CMOS fabs (Imec, Belgium and LETI, France). With this approach, mask, wafer, processing and overhead costs are all shared between participating users. All silicon photonic devices in the scope of this thesis are fabricated through ePIXfab.

We used ePIXfab MPW runs that are specific for passive photonic devices. In passive devices runs, designs are processed on a 200 mm diameter SOI wafer made of 220 nm top silicon layer with a 2  $\mu\text{m}$  buried oxide layer. The fabrication processes are carried out using deep-UV 193 nm lithography. The processes offered in these runs are outlined in Figure 3.3. Only two etch steps are offered: 220 nm deep etch and 70 nm shallow etch. The 220 nm etch step is generally used for fabricating ridge waveguides and the 70 nm etch process is usually used in the definition of grating couplers and rib waveguides. Using both etch steps, quite complex photonics structures can be realized.

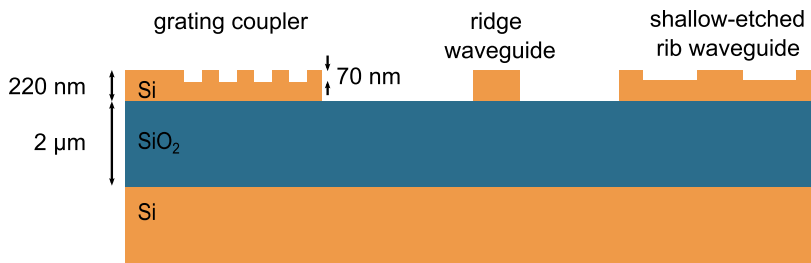


**Figure 3.3:** Cross-sectional view of SOI processes offered by ePIXfab passive components runs.

### 3.2.2 Basic integrated photonic components in SOI

In this section, we provide a brief background on three integrated photonic components to design an integrated interferometer: waveguides, splitters and grating couplers.

## Waveguides

Integrated photonic waveguides are used to confine and guide light on a planar substrate. Like an optical fiber, integrated photonic waveguides have a high-index core that is surrounded by a low-index cladding. However, compared to optical fibers, the refractive index contrast between the core and the cladding is much higher for SOI waveguides. As a result, the optical mode is much tightly confined to the core, allowing less than a micron size waveguides and very small bend radii. At 1550 nm, a typical single-mode SOI ridge waveguide has 450 nm width and 220 nm height. Such a waveguide can have a 5  $\mu\text{m}$  bend radius, losing only 0.01 dB power per 90° bend. With this type of waveguides very compact PICs can be fabricated. However, the small waveguide size has also its disadvantages: high propagation loss and sensitivity to fabrication tolerances. The loss of a standard single-mode fiber (SMF-28) is  $< 0.35$  dB/km, while a 450 nm wide, 220 nm high, SOI ridge waveguide fabricated with 193 nm deep UV lithography has 1.4 dB/cm propagation loss at 1550 nm [22]. The propagation loss in SOI waveguides is caused mainly by the scattering at the sidewalls of the waveguide [23]. The reason for the scattering is the roughness created during the etching process. By using shallow-etched rib waveguides, the overlap between the E-field and the sidewalls of the waveguide can be reduced. Propagation loss of 0.27 dB/cm for 470 nm wide, shallow-etched rib waveguides have been demonstrated [24].

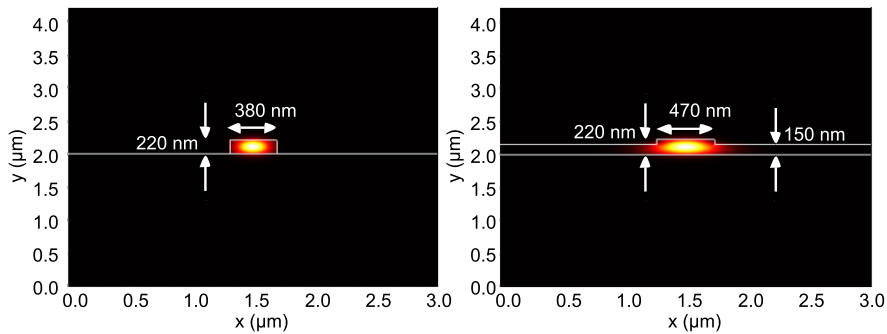


**Figure 3.4:** Mode profiles of the fundamental TE modes of SOI waveguides at 1300 nm. (a) Ridge waveguide. (b) Shallow-etched rib waveguide.

The fundamental transverse-electric (TE) mode profiles of single-mode ridge and shallow-etched rib waveguides at 1300 nm are shown in Figure 3.4. The fundamental mode is guided in the center of the wave-

uide. The confinement of the fundamental mode in a shallow-etched rib waveguide is not as tight as the confinement in a ridge waveguide, requiring larger bend radii.

### **Splitters / Couplers**

Splitting optical power is essential in interferometry. An important parameter of a splitter used in an interferometer for OCT is the wavelength dependence of its splitting ratio. An OCT system operating around 1300 nm would ideally require splitters which are as wavelength independent as possible over 100 nm. Widely used splitters in integrated photonics are y-splitters, directional couplers and multimode interference (MMI) splitters. Y-splitters are wavelength independent and are good candidates for splitting the light equally in two arms. However, when it is used for combining two arms, 3 dB power loss will occur. They are also not suitable for balanced detection, which requires  $2 \times 2$  splitters. Balanced detection helps to suppress common-mode noise such as relative intensity noise [25]. The working principle of an MMI splitter is based on interference of several modes in a multimode waveguide [26]. The 3 dB bandwidth for MMI splitters is around 50 nm and it may have some undesired internal reflections [27]. Directional couplers consist of identical parallel waveguides. Their splitting ratio is highly wavelength dependent, and therefore they are suitable only for narrow-band operation. They are also quite sensitive to fabrication tolerances.

A lesser-known broadband splitter is the adiabatic coupler. It resembles a directional coupler; however, its geometry and operating principle are different. Waveguides in a directional splitter are identical, while in an adiabatic coupler, a narrow and a broad waveguide on one side, gradually converge to identical waveguides on the other side. Adiabatic means that the input mode gradually changes its profile while traveling through the coupler. Mode evolutions in a directional coupler and an adiabatic coupler are illustrated in Figure 3.5. An input field to a directional coupler is composed of two super modes in the coupling section. These two modes have different effective indices and propagate at different speeds. On the other hand, in an adiabatic coupler, an input mode excites only one mode. While propagating through the coupler, ideally, this mode adiabatically transforms to a mode that carries equal amount of power in the output arms. Adiabatic couplers using both rib and ridge silicon waveguides have been experimentally demonstrated [28], [29]. For our interferometer in this study, we used adiabatic couplers.

The design and characterization of these couplers are explained in the following sections.

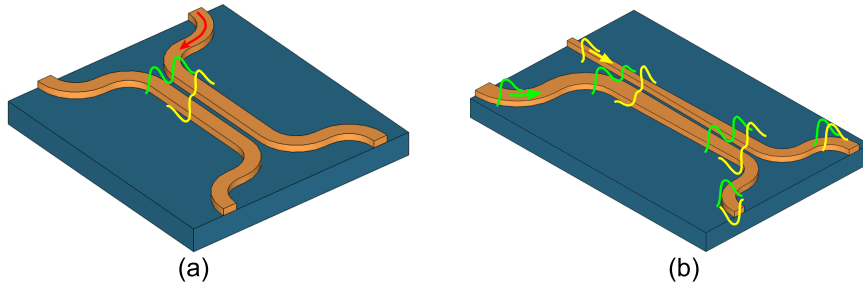


**Figure 3.5:** Mode evolutions in directional and adiabatic couplers. (a) In a directional coupler, both its even (green) and odd (yellow) modes are excited. (b) In an adiabatic coupler, only one of the modes is excited, the even (green) or the odd (yellow) mode.

### Grating couplers

Photonic integrated circuits are usually interfaced with single mode optical fibers, which have mode-field diameter of  $10\ \mu\text{m}$ . Interfacing silicon waveguides, which have less than a micron cross-section, to an optical fiber is challenging. One common solution for fiber-to-chip coupling of such small waveguides is to use grating couplers [30]. As illustrated in Figure 3.6a, if a waveguide is etched periodically, the propagating light will be diffracted by the grating. By changing the periodicity of the grating, the angle of diffraction can be tuned and by changing the etch depth, the size of the diffracted field can be modified. A 3D illustration of coupling light from a waveguide to a fiber through a grating coupler is given in Figure 3.6b. Light from a small waveguide expands to the size of the grating and the diffracted light from the grating couples to a fiber. Grating couplers fabricated on 220 nm SOI with 70 nm etch depth have typically 6 dB insertion loss and 43 nm 1 dB bandwidth [30] at 1550 nm. An advantage of grating couplers is the ability to measure vertically without the need to cleave and polish the chips, which is necessary with side (butt) coupling. Vertical access to waveguides also enables wafer-scale testing.

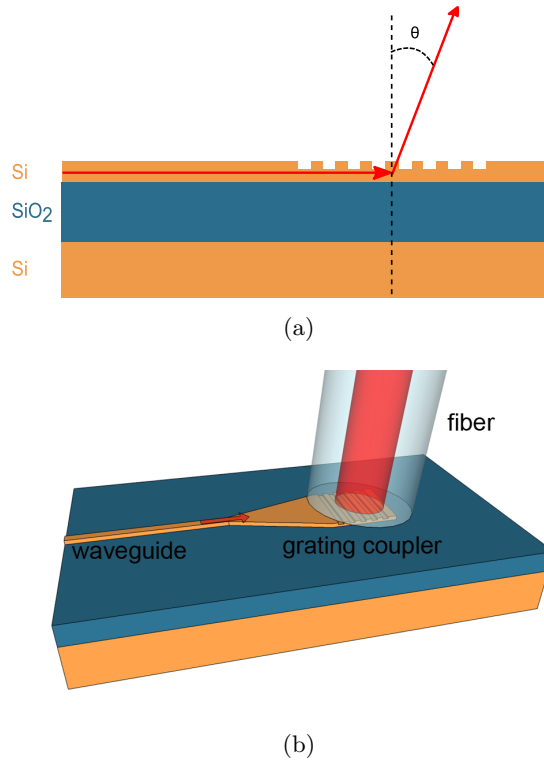


**Figure 3.6:** Illustration of a grating coupler. (a) Diffraction of light out of the chip using a grating coupler, side view. (b) Coupling of light from a waveguide to a fiber through a grating coupler.

### 3.3 Design of the photonic integrated interferometer and the SS-OCT setup

OCT systems built with fiber and/or discrete optical components usually utilize a Michelson type interferometer. In principle, an OCT system can also utilize a Mach-Zehnder interferometer as it does not affect the SNR (signal-to-noise ratio) of the system [31]. However, unlike optical fibers, integrated waveguides have sidewall roughness due to limitations in the fabrication processes. The roughness on the sidewall of a waveguide scatters the light in all directions and is mostly radiated away; however, some of it will scatter back into the waveguide. In Michelson configuration, backscattering due to the sidewall roughness in the sample and reference arm waveguides can degrade the system performance in high-

index-contrast waveguides such as SOI waveguides, as we demonstrated previously [32]. For that reason, we chose to design a Mach-Zehnder type interferometer rather than a Michelson interferometer.

### 3.3.1 Waveguide design

For the Mach-Zehnder interferometer design in this study, shallow-etched rib waveguides were preferred over ridge waveguides, as they have lower sidewall roughness and propagation loss. Shallow-etched rib waveguides support only TE modes and are inherently polarization maintaining. We also decided to deposit  $\text{SiO}_2$  on top of the waveguides to protect the waveguides from contamination with dust. To determine the waveguide size for single mode operation, we simulated the effective refractive-index ( $n_{\text{eff}}$ ) as a function of waveguide width, Figure 3.7. For all waveguide related simulations in this study, we used fully-vectorial mode-solver software wave and optical propagation software Fimmprop (both from Photon Design, UK) [33]. The effective refractive-index simulation was done at 1265 nm, which is the lower spectral end of the swept-source laser of the OCT system. Here, the cut-off region is determined by the effective refractive index ( $n_{\text{eff}} = 2.74$ ) of the 150 nm thick slab region. When the width of the waveguide increases beyond 525 nm,

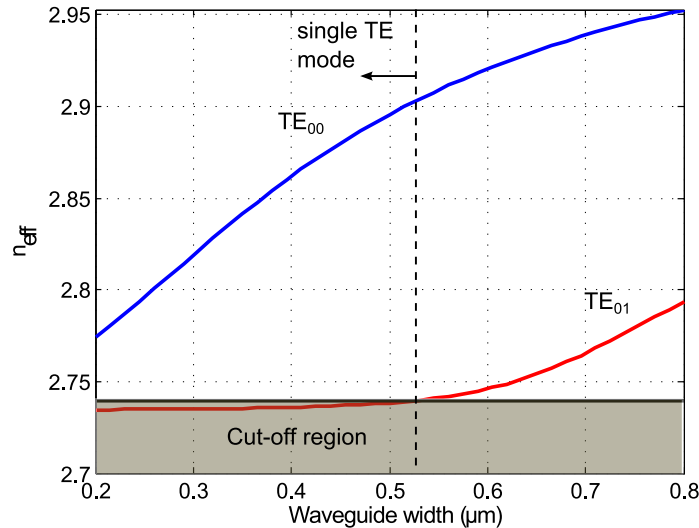


**Figure 3.7:** Effective refractive index as a function of waveguide width for a  $\text{SiO}_2$  clad SOI waveguide at 1265 nm.

the  $n_{neff}$  of  $TE_{01}$  mode becomes larger than the  $n_{eff}$  of the slab and the  $TE_{01}$  mode becomes a guided mode of the waveguide. Thus, the waveguide is single mode for widths smaller than 525 nm.

In OCT, dispersion mismatch in reference and sample arms degrades the axial resolution. For that reason, we also simulated group-velocity dispersion (GVD) with respect to waveguide width at 1312 nm, which is the center wavelength of the light source. As can be seen in Figure 3.8, GVD is decreasing with an increasing waveguide width. Since  $\text{SiO}_2$  top cladding protects the waveguides from contamination, we favored it over air cladding as the GVD advantage of air cladding is not significant. We chose the waveguide width as 470 nm; as wide as possible but slightly away from the single-mode cut-off width (525 nm).

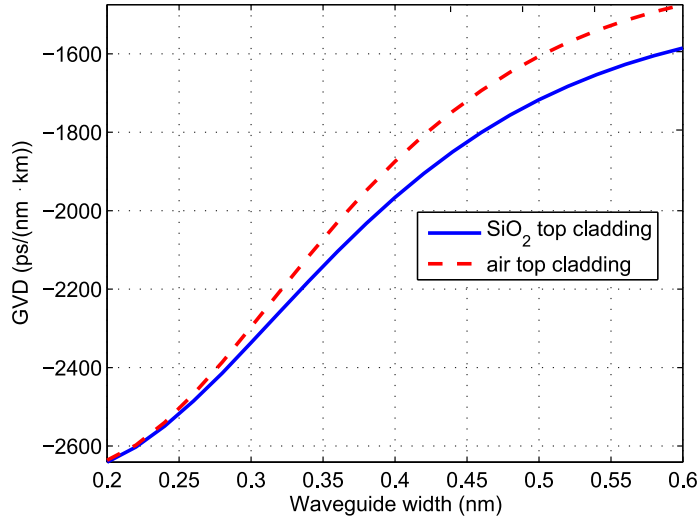


**Figure 3.8:** Simulation of GVD for shallow-etched rib waveguide for different waveguide widths at 1312 nm.

### 3.3.2 Adiabatic coupler design

For the  $2 \times 2$  couplers, we chose to design adiabatic couplers as they have a broader bandwidth than directional couplers. We designed a  $2 \times 2$  adiabatic coupler by fixing its gap to 700 nm, asymmetric waveguides widths to 350 nm and 470 nm, and symmetric waveguide widths to 410 nm. Then, using the optical propagation software Fimmprop, we simulated the splitting ratio with respect to the length of the splitter. The splitting ratio converged close to 50:50 for lengths greater than

1050 nm. To make sure that it is sufficiently adiabatic we chose the length of the splinter twice as that value: 2100 nm.

An SEM (scanning electron microscope) image of a fabricated adiabatic coupler is given in Figure 3.9. As can be seen from the SEM images, the side walls are not perfectly vertical. Simulation of the optical mode propagation in the straight section of the  $2 \times 2$  adiabatic coupler, when one of the inputs is excited, is given in Figure 3.10. In the figure, we see that the mode transfer happens mainly in the last 500  $\mu\text{m}$ .

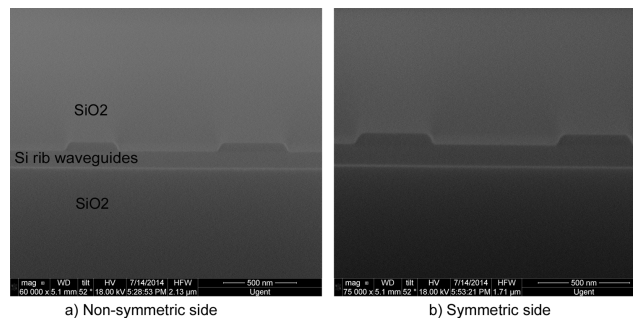


**Figure 3.9:** SEM image of the fabricated adiabatic coupler. a) Non-symmetric waveguides, both waveguides have the same width. b) Symmetric waveguides, the waveguides have different widths.

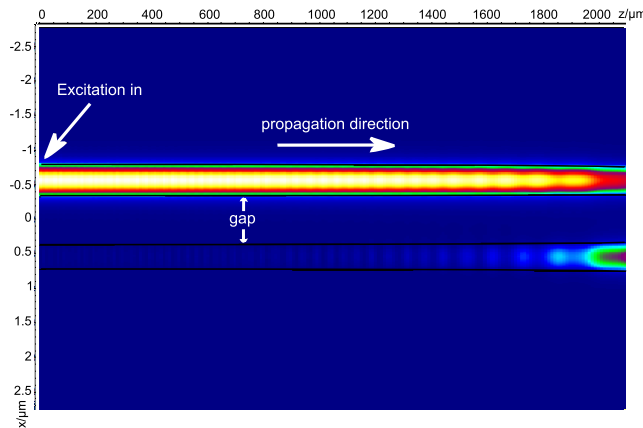


**Figure 3.10:** Simulation of mode propagation in the straight section of the  $2 \times 2$  adiabatic coupler.

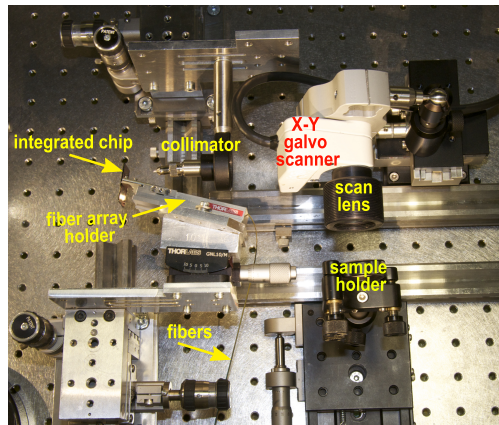
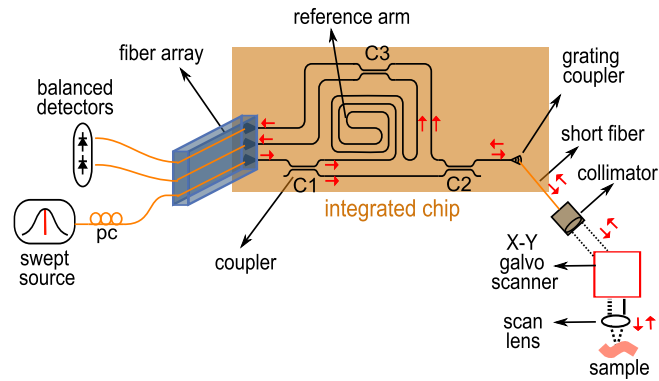
In principle,  $1 \times 2$  splitters can be realized using y-splitters, as they are wavelength independent. However, generally y-splitters have higher

insertion losses than directional type couplers and also cause some back reflection at the junction. For that reason, we decided to use the  $2 \times 2$  adiabatic couplers also as  $1 \times 2$  couplers, leaving one of the ports unused.

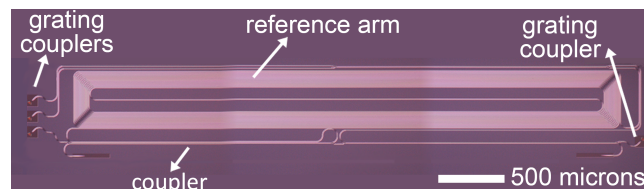
### 3.3.3 The SS-OCT system with the integrated interferometer

Using shallow-etched SOI rib waveguides with 470 nm width, we designed a Mach-Zehnder interferometer for SS-OCT. The Mach-Zehnder interferometer and the SS-OCT system built around the chip are illustrated in Figure 3.11a. Light from a swept source (Axsun Technologies, USA) centered at 1312 nm is coupled into the chip using an SMF-28 fiber array with a 127  $\mu\text{m}$  pitch and  $10^\circ$  polish angle (OZ Optics, Canada). For long term alignment stability, the fiber array was glued to the chip with UV curable glue. Coupling in and out of the chip is achieved with grating couplers. We used tilted grating couplers with reduced back-reflection [34]. The polarization of the input light is adjusted to the TE-polarization, since the grating couplers were designed for TE-light. After entering the chip, the light is split into reference and sample arms via the  $2 \times 2$  coupler C1. All couplers of the interferometer are adiabatic couplers. The reference arm consists of a 13 cm long (physical length) spiral. In the sample arm, the light is split again by the  $2 \times 2$  coupler C2 and finally sent out of the chip with a grating coupler. The light exiting the chip is coupled to a short (2 cm) piece of SMF, which is attached to a collimator (F280APC-C, Thorlabs, USA). The short fiber is cleaved on the chip side and connectorized (FC/APC) on the collimator side. Using that short piece of fiber, it is easier to align the collimator to the output of the grating coupler. The light from the collimator is directed to the sample via the galvanometric (galvo) x-y scanner and the scan lens. Back-scattered light from the sample is combined on the chip with the light from the reference arm at the  $2 \times 2$  coupler C3. The combined light at both output arms of the  $2 \times 2$  coupler C3 leaves the chip via grating couplers. The fibers in the fiber array aligned with these grating couplers send the light to a balanced photodetector (Thorlabs PDB 110C, USA). A photograph of the setup showing the integrated interferometer chip and the components around it is given in Figure 3.11b.

A microscope image of the fabricated chip is shown in Figure 3.11c. The single-mode shallow-etched rib waveguides are 470 nm wide, 220 nm high, and the bend radius is 50  $\mu\text{m}$ . The group index of the waveguides is  $n_g = 3.88$  and hence the optical length of the reference arm is



(a)



(b)

**Figure 3.11:** a) Schematic of the OCT setup with the photonic integrated circuit, pc: polarization controller; C1, C2, C3:  $2 \times 2$  adiabatic couplers. The direction of the light is indicated by red arrows. b) Photograph of a part of the SS-OCT setup with the chip. c) Microscope image of the fabricated photonic integrated interferometer.

$13 \text{ cm} \times 3.88 = 50.4 \text{ cm}$ . A single etch step of 70 nm was used for the definition of the waveguides and the grating couplers. The fabrication was

carried out through ePIXfab, and the name of the specific fabrication run was EP3540.

To characterize the individual photonic integrated components, we measured the bandwidth of the grating couplers, the  $2 \times 2$  couplers, and the power levels at the sample and reference arms. The grating couplers have 7.5 dB insertion loss and a 45 nm bandwidth (3 dB). For the  $2 \times 2$  couplers, we chose to design adiabatic couplers as they have a broader bandwidth than directional couplers. Simulated and measured splitting ratios of the adiabatic coupler are plotted in Figure 3.12. There is a slight deviation of the measurements relative to the simulations. This discrepancy could be attributed to the possibility that fabricated waveguide geometries are slightly different from the simulated ones.

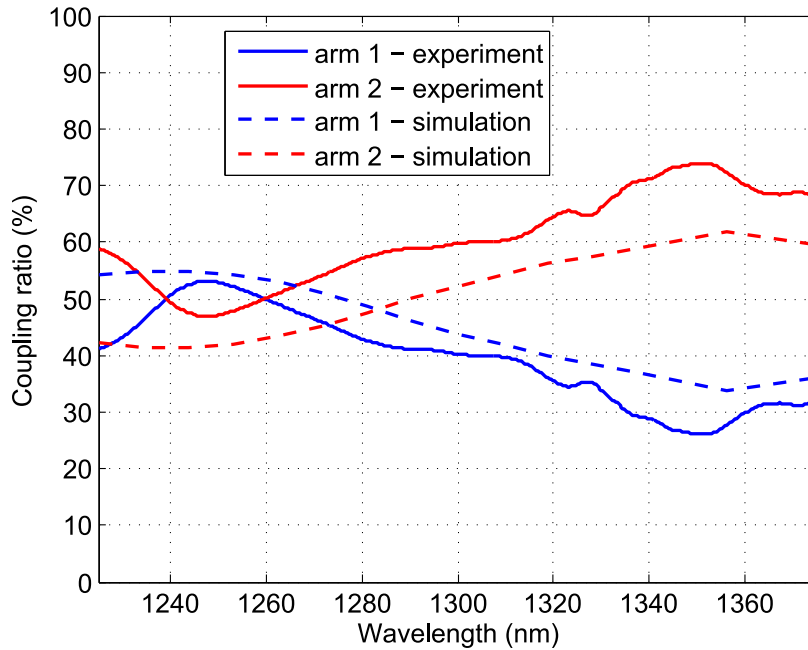


**Figure 3.12:** Measured and simulated coupling ratios of the adiabatic coupler.

### 3.4 Axial resolution and sensitivity characterization

The swept-source laser has a 50 kHz repetition rate, 92 nm tuning range, and provides  $-6$  dB fall-off at 3.5 mm depth. Each sweep cycle is sam-

pled with 1088 points which corresponds to a 5.09 mm maximum imaging depth. The power delivered to the chip was 12.4 dBm (17.5 mW), while the power on the sample was measured to be  $-9.4$  dBm (115  $\mu$ W), which means 21.8 dB attenuation compared to the input power. The attenuation is mostly due to losses induced by the two grating couplers and two  $2 \times 2$  couplers. The power levels from the reference arm reaching the balanced photodetectors were  $-14.7$  dBm (36  $\mu$ W) and  $-16.8$  dBm (21  $\mu$ W).

As dispersion of the reference arm cannot be compensated for in the sample arm, numerical dispersion compensation in software is necessary [35]. For dispersion compensation, we first measured the reflection from a mirror placed in the sample arm. The measured interference fringe (Figure 3.13a) shows that the fringe frequency increases strongly with increasing wavelength. Compared to the source bandwidth, the measured bandwidth of the interference is reduced due to the smaller bandwidth of the grating couplers. This bandwidth reduction limits the axial resolution to 24.4  $\mu$ m (FWHM) (obtained from the Fourier transform of the envelope of the interference signal). On the other hand, without dispersion compensation, the Fourier transform of the interference resulted in 1231  $\mu$ m axial resolution as shown in Figure 3.13b. To compensate for dispersion, we found the dispersion coefficients by fitting a 3<sup>rd</sup> order polynomial to the phase obtained from the interference. After 3<sup>rd</sup> order dispersion compensation [35], 25.5  $\mu$ m axial resolution was obtained as shown in Figure 3.13b. Compensation for dispersion orders higher than the 3<sup>rd</sup> order did not further improve the axial resolution. The axial resolution of a fiber based-OCT system using the same laser was 12.5  $\mu$ m [36]. It should be noted that if the sample is placed close to the maximum imaging depth, aliasing will occur due to the large dispersion. The aliased signals cannot be compensated for dispersion and axial resolution and OCT signal amplitude near the maximum imaging depth will be degraded [37].

To characterize the sensitivity of the system, we placed a neutral density filter with an optical density (OD) of 1.2 in the sample arm, and measured the reflection from a mirror. The sensitivity of the system was calculated by the ratio of the amplitude of the OCT signal peak to the standard deviation of the noise floor. The sensitivity of the system with 115  $\mu$ W power on the sample was measured to be 62 dB. We also measured the sensitivity of the fiber-based SS-OCT system [36] to be 84 dB, using the same swept source, reference and sample arm powers, galvo-scanner, photodetector and analog-to-digital converter card

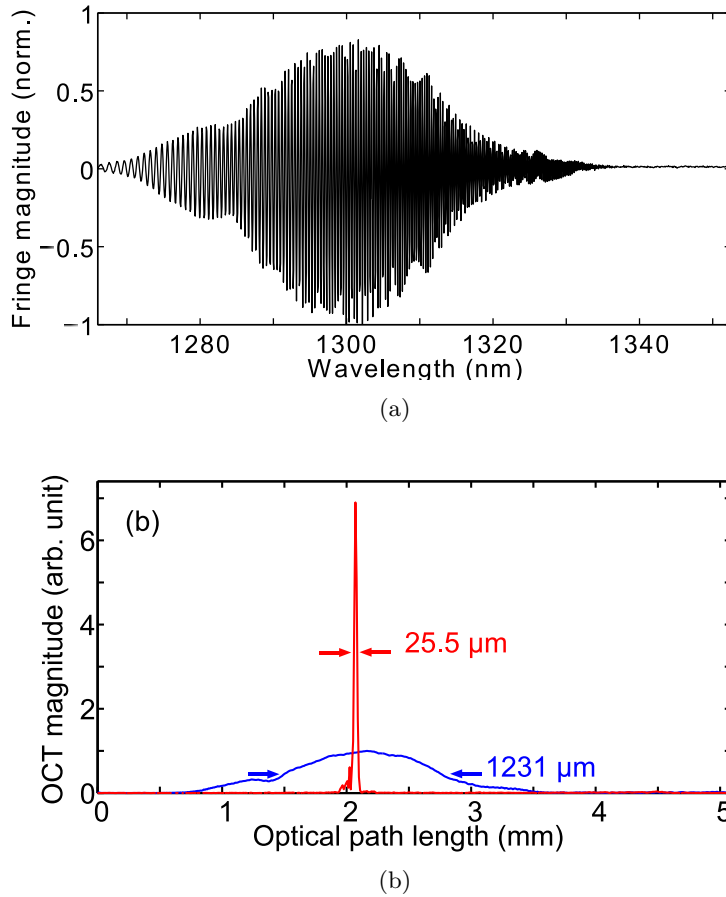


**Figure 3.13:** a) Interference fringe for a reflection from a mirror. b) Fourier-transform of the interference signal, before (blue) and after (red) dispersion compensation. The peak of the blue line is normalized to 1.

settings. These two sensitivity measurements together with their shot-noise limits are summarized in Table 3.1. The chip-based system had a 22 dB lower sensitivity than the fiber-based system. The degradation of the sensitivity can be explained mainly by the insertion losses in the grating couplers and an additional 3 dB loss of the  $2 \times 2$  coupler C2 (while reflected light from the sample passes through the  $2 \times 2$  coupler C2 and goes towards the photodetectors). Additionally, the  $2 \times 2$  couplers of the fiber SS-OCT system (FC1310-70-50-APC, Thorlabs, USA) were significantly more wavelength independent than the on-chip  $2 \times 2$

couplers and thus are better suited for balanced detection resulting in improved common mode noise reduction.

System	Ps ( $\mu$ W)	Sens. shot noise limited (dB)	Sens. meas. (dB)	Chip losses (dB)	Sens. degr. other (dB)
fiber-based	115	102	84	-	18
with integrated interferometer	115	102	62	15	25

**Table 3.1:** Sensitivities and losses. Ps: power at the sample, Sens. meas. : Sensitivity measured, Sens. degr.: Sensitivity degradation.

### 3.5 OCT imaging of tissue phantom

To demonstrate OCT imaging with the chip-based system, we imaged a three-layer tissue phantom. A photograph of the phantom is given in Figure 3.14. The scattering layers of the phantom were separated by non-scattering tape [15]. We obtained an OCT image of the tissue phantom as shown in Figure 3.15 by averaging 100 B-scans (cross-sectional images). The Matlab code used to generate this image is provided in Appendix B. Near the middle of the image, a faint residual background signal as a result of internal reflections in the chip is seen. Due to laser power and phase fluctuations between each A-line, the background sig-

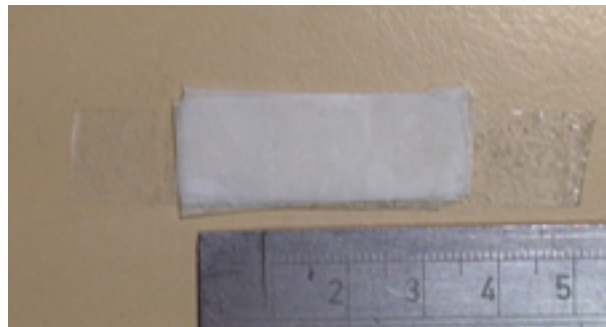


**Figure 3.14:** Photograph of the layered tissue phantom.

nal could not be completely removed by background subtraction. The residual background signal was observed only with the chip-based system, and is absent in the fiber-based system. The phantom was placed slightly away from the residual background signal to prevent them from overlapping.

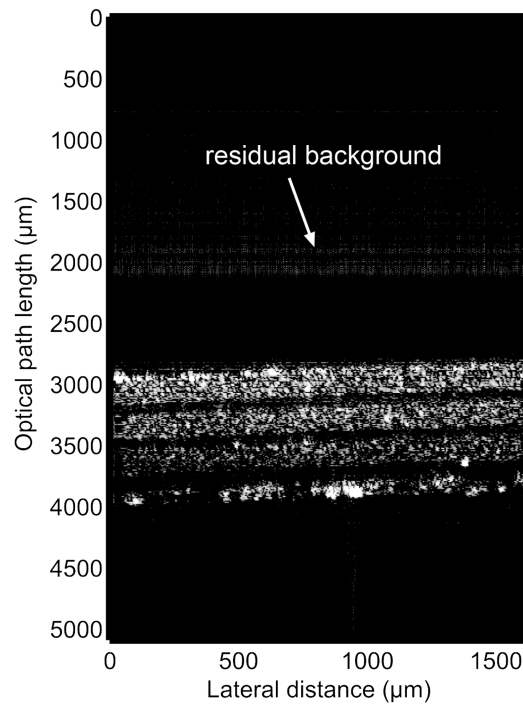


**Figure 3.15:** OCT cross-sectional image (average of 100 B-scans) of a layered tissue phantom.

### 3.6 Discussion

Although we demonstrated OCT imaging using the chip-based system, the sensitivity and axial resolution are relatively low compared to state-of-the-art OCT systems. However, the sensitivity and the axial resolution can be significantly improved using more advanced fabrication methods to fabricate fiber to chip coupling structures with lower insertion loss and larger bandwidth. Simple grating couplers used in this study are easy to fabricate but are not the optimum solution. By using more advanced fabrication processes, grating couplers with 1.6 dB inser-

tion loss and 80 nm 3 dB bandwidth have been demonstrated [38]. For even larger bandwidths, a solution is to use horizontal butt-coupling using spot size converters to couple the light in and out of the chip. Spot size converters gradually enlarge the mode size in the waveguide and are usually fabricated as tapered waveguide structures. Ben Bakir et al. demonstrated  $3\ \mu\text{m} \times 3\ \mu\text{m}$  spot size converters with  $> 200\ \text{nm}$  bandwidth and 1 dB insertion loss [39]. Coupling efficiently to such a small spot size converter with a lensed fiber is feasible. However, based on our experience, coupling efficiently to multiple adjacent small spot size converters may not be practical due to fabrication tolerances in lensed fiber arrays. Thus, spot size converters with low-loss coupling to standard SMFs are desirable. Shiraishi et al. demonstrated a spot size converter with 2.8 dB coupling loss to a standard SMF [40]. SMF spot size converters would also increase the coupling tolerances and reduce packaging costs.

After we have fabricated the interferometer, Yun et al. published a study on adiabatic couplers using SOI rib waveguides [28]. In that study, they demonstrated a design with a flatter splitting ratio than what we have measured. Their rib waveguides had 220 nm-high ribs with 90 nm-high slabs. At the asymmetric side, they used 400 nm and 600 nm wide waveguides, which were tapered to 500 nm waveguides at the symmetric side. The gap of the coupling region was 200 nm and the length was only 100  $\mu\text{m}$ . Thus, by using waveguides with larger effective index difference, the performance of the adiabatic coupler can be significantly improved.

In general, high index contrast integrated waveguides are much more dispersive than SMFs, however by changing the width and height of the waveguides or the cladding material, dispersion could be reduced. Through simulations, we observed that using ridge waveguides rather than rib waveguides provides more flexible dispersion tailoring. For example, we simulated that a  $\text{SiO}_2$  cladding ridge waveguide with 220 nm height and 540 nm width would have zero group velocity dispersion at 1310 nm. Although ridge waveguides have higher losses than rib waveguides, their loss could be reduced to 0.45 dB/cm by using higher resolution lithography [18].

The return loss of individual components in a photonic integrated circuit for OCT is also crucial. The return loss of fiber components which are connected to each other with fibers much longer than the coherence length of the light source do not present a significant problem. However, the distances between individual components in a photonic integrated chip are in the order of the coherence length of OCT light

sources. Thus, fringes due to reflections within the chip may appear as spurious background signals in the OCT signal. To avoid this, the transition between different photonic integrated components needs to be sufficiently smooth to reduce such reflection effects.

While the first step towards an on-chip SS-OCT is to optimize the passive structures, in the long term, integration with active components will open new application opportunities. Wafer scale integration of germanium photodetectors on silicon has recently been demonstrated [41]. An interferometer design similar to the one presented in this study can be integrated with such on-chip photodetectors and used for balanced SS-OCT. Integrating the photodetectors will also eliminate the chip-to-fiber losses for the light sent to the photodetectors. Integration of a tunable laser and other active elements (e.g. optical amplifier, modulator) can be pursued by bonding pre-fabricated components on top of the passive structures or by bonding the active material epitaxial layers on top of the passive waveguides and then processing the active components [19].

Considering state-of-the-art silicon photonic components, including integrated photodetectors, an integrated interferometer for SS-OCT with sensitivity close to fiber interferometers could be realized. The major loss will be the 6 dB loss at coupler C2, as broadband integrated circulators have not matured yet. Additional 1-2 dB loss at the chip to collimating lens interface and 0.5 dB propagation loss could be present.

In conclusion, we fabricated and characterized a silicon-based, integrated photonics interferometer for SS-OCT. We demonstrated cross-sectional imaging of a layered tissue phantom showing the feasibility and potential of integrated silicon-based OCT systems. Thanks to the small size of silicon photonic integrated components, silicon photonics can become a platform for highly parallel OCT systems. Monolithic/hybrid integration of active components with passive structures can enable an on-chip OCT system at low cost and small form factor.



# References

- [1] G. Grasso, P. Galli, M. Romagnoli, E. Iannone, and A. Bogoni, “Role of integrated photonics technologies in the realization of terabit nodes [invited]”, *Optical Communications and Networking, IEEE/OSA Journal of*, vol. 1, no. 3, B111–B119, 2009 (cit. on p. 60).
- [2] I. P. Kaminow, “Optical integrated circuits: a personal perspective”, *Journal of Lightwave Technology*, vol. 26, no. 9, pp. 994–1004, 2008 (cit. on p. 61).
- [3] L. Grenouillet, T. Dupont, P. Philippe, J. Harduin, N. Olivier, D. Bordel, E. Augendre, K. Gilbert, P. Grosse, A. Chelnokov, *et al.*, “Hybrid integration for silicon photonics applications”, *Optical and Quantum Electronics*, vol. 44, no. 12-13, pp. 527–534, 2012 (cit. on p. 61).
- [4] G. D. Cole, E. Behymer, T. C. Bond, and L. L. Goddard, “Short-wavelength mems-tunable vcsels”, *Optics express*, vol. 16, no. 20, pp. 16 093–16 103, 2008 (cit. on p. 61).
- [5] V. Jayaraman, G. Cole, M. Robertson, C. Burgner, D. John, A. Uddin, and A. Cable, “Rapidly swept, ultra-widely-tunable 1060 nm mems-vcsels”, *Electronics letters*, vol. 48, no. 21, pp. 1331–1333, 2012 (cit. on p. 61).
- [6] M. P. Minneman, J. Ensher, M. Crawforda, and D. Derickson, “All-semiconductor high-speed akinetic swept-source for oct”, in *Asia Communications and Photonics Conference and Exhibition*, Optical Society of America, 2011, p. 831 116 (cit. on p. 61).
- [7] B. W. Tilma, Y. Jiao, J. Kotani, B. Smalbrugge, H. P. Ambrosius, P. J. Thijs, X. J. Leijtens, R. Notzel, M. K. Smit, and E. A. Bente, “Integrated tunable quantum-dot laser for optical coherence tomography in the 1.7 wavelength region”, *Quantum Electronics, IEEE Journal of*, vol. 48, no. 2, pp. 87–98, 2012 (cit. on p. 61).
- [8] C. R. Doerr and K. Okamoto, “Advances in silica planar lightwave circuits”, *Journal of lightwave technology*, vol. 24, no. 12, pp. 4763–4789, 2006 (cit. on p. 61).
- [9] L. Zhuang, D. Marpaung, M. Burla, W. Beeker, A. Leinse, and C. Roeloffzen, “Low-loss, high-index-contrast si3n4 - sio2 optical waveguides for optical delay lines in microwave photonics signal processing”, *Optics express*, vol. 19, no. 23, pp. 23 162–23 170, 2011 (cit. on p. 61).

- 
- [10] A. Mekis, S. Gloeckner, G. Masini, A. Narasimha, T. Pinguet, S. Sahni, and P. De Dobbelaere, “A grating-coupler-enabled cmos photonics platform”, *Selected Topics in Quantum Electronics, IEEE Journal of*, vol. 17, no. 3, pp. 597–608, 2011 (cit. on p. 61).
- [11] M. Bonesi, M. Minneman, J. Ensher, B. Zabihian, H. Sattmann, P. Boschert, E. Hoover, R. Leitgeb, M. Crawford, and W. Drexler, “Akinetic all-semiconductor programmable swept-source at 1550 nm and 1310 nm with centimeters coherence length”, *Optics express*, vol. 22, no. 3, pp. 2632–2655, 2014 (cit. on p. 61).
- [12] D. Culemann, A. Knuettel, and E. Voges, “Integrated optical sensor in glass for optical coherence tomography (oct)”, *Selected Topics in Quantum Electronics, IEEE Journal of*, vol. 6, no. 5, pp. 730–734, 2000 (cit. on p. 61).
- [13] D. Choi, H. Hiro-Oka, H. Furukawa, R. Yoshimura, M. Nakanishi, K. Shimizu, and K. Ohbayashi, “Fourier domain optical coherence tomography using optical demultiplexers imaging at 60,000,000 lines/s”, *Optics letters*, vol. 33, no. 12, pp. 1318–1320, 2008 (cit. on p. 61).
- [14] B. Akca, B. Považay, A. Alex, K. Wörhoff, R. de Ridder, W. Drexler, and M. Pollnau, “Miniature spectrometer and beam splitter for an optical coherence tomography on a silicon chip”, *Optics express*, vol. 21, no. 14, pp. 16 648–16 656, 2013 (cit. on p. 61).
- [15] V. D. Nguyen, N. Weiss, W. Beeker, M. Hoekman, A. Leinse, R. Heideman, T. van Leeuwen, and J. Kalkman, “Integrated-optics-based swept-source optical coherence tomography”, *Optics letters*, vol. 37, no. 23, pp. 4820–4822, 2012 (cit. on pp. 61, 78).
- [16] E. Margallo-Balbás, M. Geljon, G. Pandraud, and P. J. French, “Miniature 10 khz thermo-optic delay line in silicon”, *Optics letters*, vol. 35, no. 23, pp. 4027–4029, 2010 (cit. on p. 61).
- [17] S. Schneider, M. Lauermaun, C. Weimann, W. Freude, and C. G. Koos, “Silicon photonic optical coherence tomography system”, in *CLEO: Applications and Technology*, Optical Society of America, 2014, ATu2P–4 (cit. on p. 61).
- [18] S. K. Selvaraja, P. De Heyn, G. Winroth, P. Ong, G. Lepage, C. Cailler, A. Rigny, K. Bourdelle, D. VanThourhout, J. Van Campenhout, *et al.*, “Highly uniform and low-loss passive silicon photonics devices using a 300mm cmos platform”, in *Optical Fiber Communication Conference*, Optical Society of America, 2014, Th2A–33 (cit. on pp. 62, 80).
- [19] H. Park, M. N. Sysak, H.-W. Chen, A. W. Fang, D. Liang, L. Liao, B. R. Koch, J. Bovington, Y. Tang, K. Wong, *et al.*, “Device and integration technology for silicon photonic transmitters”, *Selected Topics in Quantum Electronics, IEEE Journal of*, vol. 17, no. 3, pp. 671–688, 2011 (cit. on pp. 62, 81).

- [20] J. S. Orcutt, B. Moss, C. Sun, J. Leu, M. Georgas, J. Shainline, E. Zraggen, H. Li, J. Sun, M. Weaver, *et al.*, “Open foundry platform for high-performance electronic-photonics integration”, *Optics express*, vol. 20, no. 11, pp. 12 222–12 232, 2012 (cit. on p. 62).
- [21] ePIXfab - The silicon photonics platform, 2015, <http://www.epixfab.eu> (cit. on p. 65).
- [22] S. K. Selvaraja, “Wafer-scale fabrication technology for silicon photonic integrated circuits”, PhD thesis, Ghent University, 2011 (cit. on p. 66).
- [23] K. P. Yap, A. Del age, J. Lapointe, B. Lamontagne, J. H. Schmid, P. Waldron, B. A. Syrett, and S. Janz, “Correlation of scattering loss, sidewall roughness and waveguide width in silicon-on-insulator (soi) ridge waveguides”, *Journal of Lightwave Technology*, vol. 27, no. 18, pp. 3999–4008, 2009 (cit. on p. 66).
- [24] W. Bogaerts *et al.*, “Compact single-mode silicon hybrid rib/strip waveguide with adiabatic bends”, *IEEE Photonics Journal*, vol. 3, no. 3, pp. 422–432, 2011 (cit. on p. 66).
- [25] Y. Chen, D. M. de Bruin, C. Kerbage, and J. F. de Boer, “Spectrally balanced detection for optical frequency domain imaging”, *Optics express*, vol. 15, no. 25, pp. 16 390–16 399, 2007 (cit. on p. 67).
- [26] L. B. Soldano and E. C. Pennings, “Optical multi-mode interference devices based on self-imaging: principles and applications”, *Lightwave Technology, Journal of*, vol. 13, no. 4, pp. 615–627, 1995 (cit. on p. 67).
- [27] R. Halir, I. Molina-Fern andez, J. Wang uemert-P erez, A. Ortega-Mo nux, J. de-Oliva-Rubio, and P. Cheben, “Characterization of integrated photonic devices with minimum phase technique”, *Optics express*, vol. 17, no. 10, pp. 8349–8361, 2009 (cit. on p. 67).
- [28] H. Yun, W. Shi, Y. Wang, L. Chrostowski, and N. A. Jaeger, “2x2 adiabatic 3-dB coupler on silicon-on-insulator rib waveguides”, in *Photonics North 2013*, International Society for Optics and Photonics, 2013, pp. 89150V–89150V (cit. on p. 67, 80).
- [29] M. R. Watts, J. Sun, C. DeRose, D. C. Trotter, R. W. Young, and G. N. Nielson, “Adiabatic thermo-optic Mach-Zehnder switch”, *Optics letters*, vol. 38, no. 5, pp. 733–735, 2013 (cit. on p. 67).
- [30] D. Taillaert, “Grating couplers as interface between optical fibres and nanophotonic waveguides”, PhD thesis, Ghent University, 2004 (cit. on p. 68).
- [31] A. M. Rollins and J. A. Izatt, “Optimal interferometer designs for optical coherence tomography”, *Optics letters*, vol. 24, no. 21, pp. 1484–1486, 1999 (cit. on p. 69).

- [32] G. Yurtsever, K. Komorowska, and R. Baets, “Low dispersion integrated michelson interferometer on silicon on insulator for optical coherence tomography”, in *European Conference on Biomedical Optics*, Optical Society of America, 2011, 80910T (cit. on p. 70).
- [33] Photon Design , 2015, <http://www.photond.com> (cit. on p. 70).
- [34] D. Vermeulen, Y. De Koninck, Y. Li, E. Lambert, W. Bogaerts, R. Baets, and G. Roelkens, “Reflectionless grating couplers for silicon-on-insulator photonic integrated circuits”, *Optics express*, vol. 20, no. 20, pp. 22 278–22 283, 2012 (cit. on p. 73).
- [35] M. Wojtkowski, V. Srinivasan, T. Ko, J. Fujimoto, A. Kowalczyk, and J. Duker, “Ultrahigh-resolution, high-speed, fourier domain optical coherence tomography and methods for dispersion compensation”, *Optics express*, vol. 12, no. 11, pp. 2404–2422, 2004 (cit. on p. 76).
- [36] N. Weiss, T. G. van Leeuwen, and J. Kalkman, “Localized measurement of longitudinal and transverse flow velocities in colloidal suspensions using optical coherence tomography”, *Physical Review E*, vol. 88, no. 4, p. 042 312, 2013 (cit. on p. 76).
- [37] T. Bajraszewski, M. Wojtkowski, M. Szkulmowski, A. Szkulmowska, R. Huber, and A. Kowalczyk, “Improved spectral optical coherence tomography using optical frequency comb”, *Optics express*, vol. 16, no. 6, pp. 4163–4176, 2008 (cit. on p. 76).
- [38] D. Vermeulen, S. Selvaraja, P. Verheyen, G. Lepage, W. Bogaerts, P. Absil, D. Van Thourhout, and G. Roelkens, “High-efficiency fiber-to-chip grating couplers realized using an advanced cmos-compatible silicon-on-insulator platform”, *Optics express*, vol. 18, no. 17, pp. 18 278–18 283, 2010 (cit. on p. 80).
- [39] B. Bakir *et al.*, “Low-loss (<1 db) and polarization-insensitive edge fiber couplers fabricated on 200-mm silicon-on-insulator wafers”, *IEEE Photonics Technology Letters*, vol. 22, no. 11, pp. 739–741, 2010 (cit. on p. 80).
- [40] K. Shiraishi, H. Yoda, and C. S. Tsai, “A two-port polarization-insensitive coupler module between single-mode fiber and silicon-wire waveguide”, *Optics express*, vol. 20, no. 22, pp. 24 370–24 375, 2012 (cit. on p. 80).
- [41] S. Assefa, F. Xia, W. M. Green, C. L. Schow, A. V. Rlyakov, and Y. A. Vlasov, “Cmos-integrated optical receivers for on-chip interconnects”, *Selected Topics in Quantum Electronics, IEEE Journal of*, vol. 16, no. 5, pp. 1376–1385, 2010 (cit. on p. 81).

# 4

## Si<sub>3</sub>N<sub>4</sub>/SiO<sub>2</sub> photonic integrated interferometer with an on-chip reference arm for spectral-domain optical coherence tomography

In this chapter, we present the design, characterization and application of a Mach-Zehnder interferometer based photonic integrated circuit for spectral-domain optical coherence tomography (SD-OCT). The design of the integrated interferometer is similar to the one in Chapter 3. However, it was designed and fabricated using silicon nitride (Si<sub>3</sub>N<sub>4</sub>) and silicon dioxide (SiO<sub>2</sub>) waveguides which are transparent from visible to mid-infrared wavelengths. The integrated photonic circuit consists of four splitters and a 190 mm long reference arm with a foot print of only 10 mm × 33 mm. It is used as the core of a spectral domain OCT system consisting of a superluminescent diode centered at 1320 nm with 100 nm bandwidth, a spectrometer with 1024 channels, and an x-y galvo scanner. The sensitivity of the system was measured to be 65 dB with 0.1 mW on the sample. Using the system, we imaged human skin *in vivo*.

In the first section, we will describe the waveguide design procedure and explain the OCT setup with the photonic integrated interferometer.

After that, we will present device characterization parameters such as axial resolution and sensitivity. Then, we will provide OCT images obtained from *in vivo* human skin. In section 3.4, we will discuss the potential improvement possibilities in the system and we will finalize the chapter with the conclusions.

The work in this chapter was done in collaboration with Dr. Boris Považay, Dr. Aneesh Alex, Behrooz Zabihian and Prof. Wolfgang Drexler from Center for Medical Physics and Biomedical Engineering, Medical University Vienna, Austria. The experiments were carried out in Prof. Drexler's lab under his supervision. Dr. Považay did the data processing, while Dr. Alex and Mr. Zabihian helped with building the setup and obtaining the images.

## 4.1 Design of the photonic integrated circuit and the OCT setup

### 4.1.1 Waveguide design

The waveguides used in our study are based on  $\text{Si}_3\text{N}_4$  and  $\text{SiO}_2$  waveguide technology called TriPleX<sup>TM</sup>, which was developed by LioniX BV (Enschede, The Netherlands) [1]. Unlike typical waveguides with high-index core surrounded by low-index cladding, these waveguides are box shaped, consisting of three layers. As illustrated in Figure 4.1, a low-index core ( $\text{SiO}_2$ ) is encapsulated in a box shaped high-index ( $\text{Si}_3\text{N}_4$ ) layer, which is buried in low-index material ( $\text{SiO}_2$ ). The refractive index

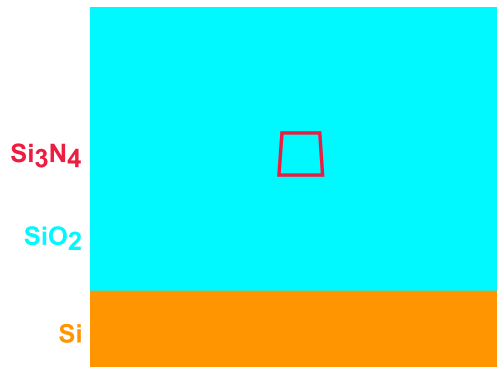


**Figure 4.1:** Illustration of a box shaped  $\text{Si}_3\text{N}_4$  waveguide embedded in  $\text{SiO}_2$  on Si-carrier.

contrast between  $\text{Si}_3\text{N}_4$  ( $n=1.98$ ) and  $\text{SiO}_2$  ( $n=1.45$ ) enables realization of smaller bends compared to doped silica waveguides, which results in smaller circuits.

The waveguides are fabricated on a silicon carrier wafer. Step by step fabrication process flow is given in Figure 4.2. The fabrication process starts with a 100 mm Si wafer, which is thermally oxidized to obtain a 8  $\mu\text{m}$  thick lower cladding layer (1-2). Next, 50 nm thick  $\text{Si}_3\text{N}_4$  is deposited on top of the wafer using low-pressure chemical vapor deposition (LPCVD) (3). Then, 1  $\mu\text{m}$  thick LPCVD  $\text{SiO}_2$  is deposited (4). After  $\text{SiO}_2$  deposition, comes the contact lithography step to define the waveguide geometry; the wafer is covered with photoresist by spin coating, the waveguide pattern from a photomask is transferred to the photoresist (5). Then, by dry etching of the  $\text{SiO}_2$  and  $\text{Si}_3\text{N}_4$  layers, the waveguide pattern is further transferred to the wafer (6). Subsequently, the remaining resist is removed (7) and followed by the second 50 nm

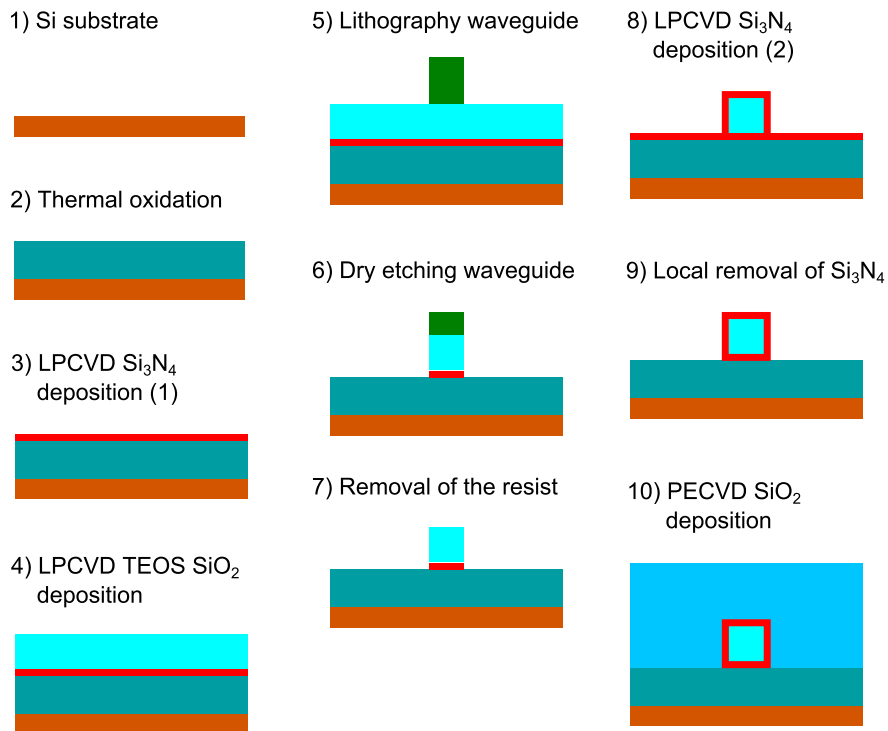


**Figure 4.2:** Process flow (cross-section) of the box-shaped TriPleX™ waveguides.

$\text{Si}_3\text{N}_4$  deposition with LPCVD (8). Part of the  $\text{Si}_3\text{N}_4$  layer is removed to form the box-shaped waveguide geometry. Finally, as a top cladding,  $> 5 \mu\text{m}$   $\text{SiO}_2$  is deposited using plasma-enhanced chemical vapor deposition (PECVD). After these fabrication steps, the wafer is annealed at  $1150^\circ\text{C}$ . Among these processes, LPCVD  $\text{SiO}_2$  layers have large compressive stress and LPCVD  $\text{Si}_3\text{N}_4$  layers have large tensile stress. By alternating both layers, a multilayer stack with largely reduced overall stress is achieved.

Interferometers for OCT require single-mode waveguides, as multi-mode interferences would degrade axial resolution, sensitivity and stability. To find the condition for single-mode operation, we simulated the effective index of the fundamental transverse-electric (TE) and transverse-magnetic (TM) modes for different waveguide widths. Although lithography allows for extremely low costs in mass production, the individual steps are very costly. Similar to the design of the silicon interferometer in Chapter 3, the design was fabricated in a multi-project-wafer run, where mask space and process costs are shared with other participants but compromises in the manufacturing technology have to be made. In this particular run, named LioniX MPW1, the height of the waveguides was fixed to  $1 \mu\text{m}$  and the  $\text{Si}_3\text{N}_4$  layer thickness was set to  $50 \text{ nm}$ . Due to the process constraints, only the width of the waveguide could be varied. During the simulations, these fabrication constraints, including the sloped sidewalls were considered. The effective index simulations were performed at  $1250 \text{ nm}$ , which is the lower spectral end of the superluminescent diode utilized in the OCT system. For the simulations we used the commercially available, fully vectorial mode solver software Fimmwave (Photon Design, Oxford, UK). The calculated TE and TM mode effective indices as a function of waveguide width are given in Figure 4.3. As seen in Figure 4.3, when the waveguide width is kept below  $1.58 \mu\text{m}$ , only the fundamental TE and TM modes can propagate. The cut-off line is determined by the effective refractive index ( $n_{eff} = 1.447$ ) of  $\text{SiO}_2$  at  $1250 \text{ nm}$ . For our design, we chose  $1 \mu\text{m}$  as waveguide width, which is far from the cut-off waveguide width and sufficiently wide for lithographic definition.

A scanning electron microscope cross-section image of a fabricated waveguide of the  $1 \mu\text{m} \times 1 \mu\text{m}$  design is shown in Figure 4.4. The  $\text{Si}_3\text{N}_4$  layer is visible in dark gray and  $\text{SiO}_2$  appears in light gray color, the thickness of the  $\text{Si}_3\text{N}_4$  layer is  $50 \text{ nm}$ . The dry etching process used in waveguide definition results in  $82^\circ$  sloped sidewalls rather than perpendicular sidewalls.

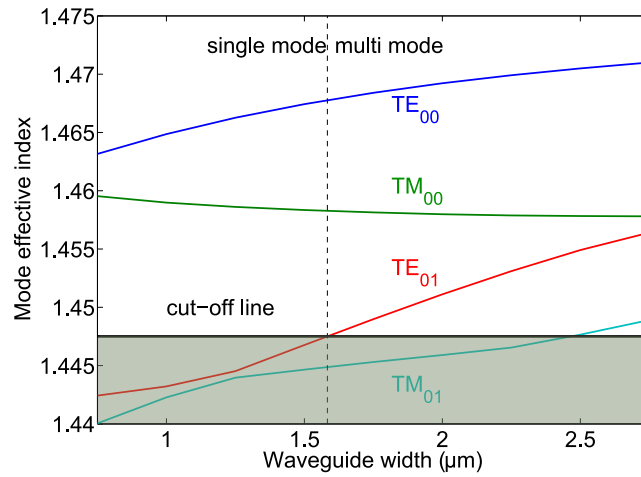


**Figure 4.3:** Calculated effective indices of the TE and TM modes of a box waveguide versus waveguide width at 1250 nm. Waveguide height: 1 μm, Si<sub>3</sub>N<sub>4</sub> layer thickness: 50 nm.

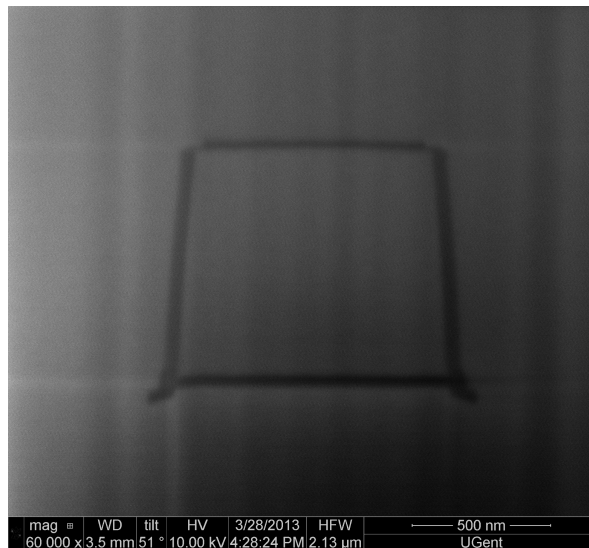


**Figure 4.4:** Scanning electron microscope image of Si<sub>3</sub>N<sub>4</sub> waveguide cross-section.

We also simulated the mode profiles for the fundamental TE and TM modes, as given in Figure 4.5a and 4.5b. Both mode profiles are nearly circular, however, the fundamental TE mode is more strongly confined in the parallel high-index layer, and the fundamental TM mode is more strongly confined in the vertical high-index layer. Due to the sloped sidewalls, the TE and TM modes are not completely symmetric, which results in different group indices and dispersion. From the simulations, we found the group indices and group velocity dispersions (GVDs) of  $TE_{00}$  and  $TM_{00}$  modes at 1320 nm to be  $(1.489, -347 \text{ ps}/(\text{nm km}))$  and  $(1.510, -205 \text{ ps}/(\text{nm km}))$  respectively. Since the propagation losses were specified as  $< 0.5 \text{ dB/cm}$  for both modes, we chose the  $TM_{00}$  mode because it has lower dispersion.

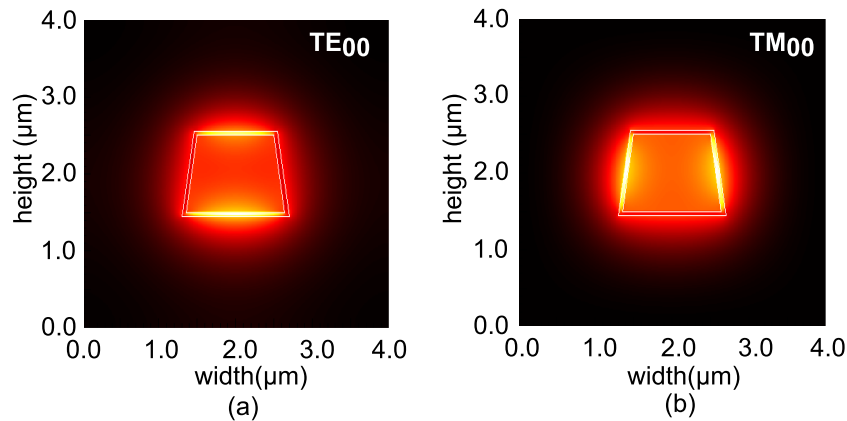


**Figure 4.5:** (a) Simulated  $TE_{00}$  mode electric field profile at 1250 nm for a waveguide  $1 \mu\text{m}$  wide and  $1 \mu\text{m}$  high. (b) Simulated  $TM_{00}$  mode electric field profile at 1250 nm for a waveguide  $1 \mu\text{m}$  wide and  $1 \mu\text{m}$  high.

The minimum bend radii of waveguides determine the size of a photonic integrated circuit. The higher the refractive index difference between the core and the cladding, the higher the confinement of the mode, which enables smaller bend radii. Box-shaped TriPleX<sup>TM</sup> waveguides have moderate size bend radii, which are larger than silicon waveguide bend radii but smaller than silica waveguide bend radii. An image of the mask file used to fabricate the mask for photolithography is shown in Figure 4.6a. In our design, the waveguides had minimum bend radius of  $2.5 \mu\text{m}$ . In this multi wafer project run, symmetric y-splitter and directional coupler designs were provided as building blocks by LioniX BV.

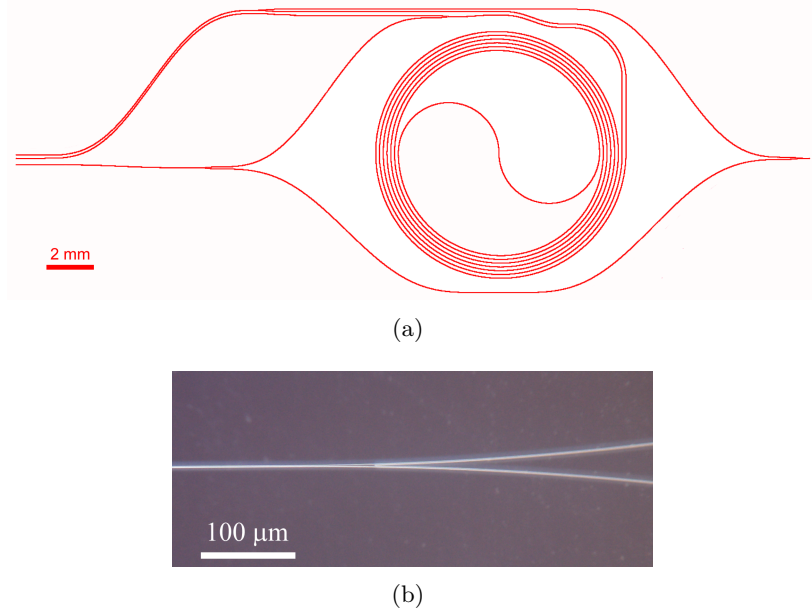
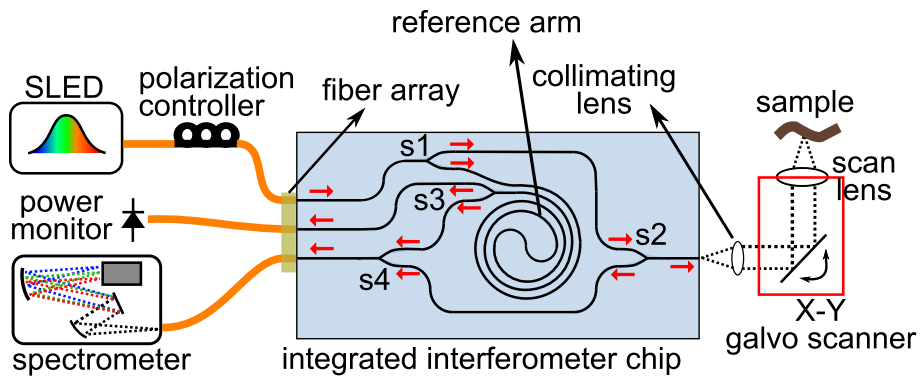


**Figure 4.6:** a) Screenshot of the mask used to fabricate the interferometer. b) A microscope image of a y-splitter that is used in the interferometer.

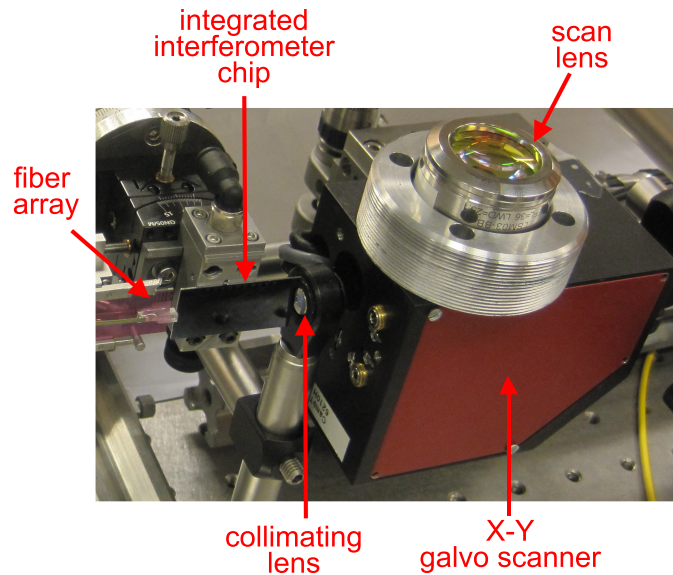
Both splitter designs were specified with 0.3 dB excess loss. Due to its wavelength independent splitting ratio, we chose to use y-splitters [2]. A microscope image of a y-splitter is given in Figure 4.6. Our decision not to design our own splitter was driven by the risks of fabrication process deviations.

#### 4.1.2 The OCT setup with the photonic integrated interferometer

Using  $1\ \mu\text{m} \times 1\ \mu\text{m}$  waveguides, we designed and fabricated a Mach-Zehnder interferometer based photonic integrated circuit for OCT. An illustration of the circuit and the OCT system is given in Figure 4.7a. The circuit has three waveguides on the left edge and one waveguide on the right edge for coupling the light in and out of the chip. The waveguides on the entry-side (Figure 4.7a left) were aligned with a fiber array that matched the pitch of the waveguides. The  $1\ \mu\text{m} \times 1\ \mu\text{m}$  waveguides have a mode-field diameter around  $2.7\ \mu\text{m}$ . To reduce the reflections at the waveguide ends, waveguides at both sides of the chip were angle polished at  $8^\circ$  to match the angle of the commercially available angle-



(a)



(b)

**Figure 4.7:** a) Schematic layout of the OCT setup with the integrated interferometer chip. b) Photograph of the setup, where the fiber array, the integrated interferometer chip and the scan lens are seen.

polished fiber arrays, which is typically  $8^\circ$ . However, the effect of  $8^\circ$  angle polish is not optimal; from simulations we find that without angle polishing the return loss for  $TM_{00}$  is 14 dB, while the return loss with  $8^\circ$  polish angle is 20 dB. To achieve a return loss level of 60 dB, which is typical for FC/APC connectors, a  $24^\circ$  polish angle is needed. The SLED

(Praevium/Thorlabs, Newton, USA) of the system has 1320 nm center wavelength, 100 nm full width half maximum (FWHM) bandwidth and 11.5 dBm power. The power of the SLED is reduced to 3.5 dBm to prevent saturation of the line scan camera of the spectrometer as the reference arm power in the current design cannot be adjusted. With this reduced input power level, the power at the sample was  $-10$  dBm ( $100 \mu\text{W}$ ). All splitters in the circuit are symmetric y-splitters and have 50/50 splitting ratio. As depicted in Figure 4.7a, light from the SLED is coupled to the chip via the fiber array and split on the chip by splitter s1. The upper waveguide after splitter s1 guides the light to splitter s2. From there the light exits the chip and is collimated by an achromatic lens ( $f = 2.97$  mm,  $\text{NA} = 0.6$ , C660TME-C, Thorlabs, Newton, USA). The collimated light is sent to an x-y scanner, which consists of a galvanometric x-y mirror pair (Thorlabs, Newton, USA) and a scan lens (LSM03, Thorlabs, Newton, USA).

Light reflected from the sample is collected via the same path and coupled back into the chip. Inside the chip, the light is split into two arms by splitter s2. Only the light in the lower arm is utilized and combined with the reference arm at combiner s4. The reference arm starts at the lower branch of splitter s1 and is comprised of a 190 mm long planar spiral. The length of the spiral was chosen considering the optical path length of the x-y scanner. After passing the spiral, via splitter s3, half of the light signal is sent to a power monitor and the other half is combined with light from the sample arm at combiner s4. The power monitor is used to monitor the alignment stability of the fiber array while setting up the system. After combiner s4, the interference of the reference and sample arms is sent to the spectrometer. The all-reflective Czerny-Turner spectrometer contains a 1024 pixel InGaAs line scan camera with 47 kHz line rate (SU1024LDH-1.7RT, Sensors Unlimited Inc., Princeton, USA). The spectrometer has 0.125 nm spectral resolution, maximum imaging range of 3.4 mm in air and  $-17$  dB fall-off over the entire imaging range. The x-y galvo scanner and the spectrometer camera are controlled with custom-built software implemented in LabVIEW (National Instruments, Austin, USA). An image of part of the setup, which contains the integrated interferometer chip, the fiber-array and the x-y scanner, is shown in Figure 4.7b. The standard die size in this fabrication run was  $16 \times 33$  mm<sup>2</sup>, which is the size of the chip seen in Figure 4.7b. The size of the integrated interferometer design on this chip is  $10$  mm  $\times$   $33$  mm.

## 4.2 Device characterization and *in vivo* human skin imaging

After aligning the setup, the polarization of the light from the SLED was adjusted by monitoring the OCT signal from a mirror. If the polarization is not properly adjusted, while measuring reflectance from a mirror, there would be two peaks corresponding to the fundamental TE and TM modes, designating the two polarization states with different group indices. As the  $TM_{00}$  mode would cause lower dispersion than  $TE_{00}$  mode, we chose the TM peak and maximized it by adjusting the polarization controller. Without dispersion compensation, the TM peak was sharper than the TE peak.

### 4.2.1 Axial resolution and sensitivity

To characterize the system's axial resolution and sensitivity, reflection from a mirror positioned at 0.25 mm far from the zero delay line was measured. The data processing consisted of background subtraction, re-sampling, spectral shaping (apodization) and dispersion compensation. For spectral shaping, the spectrum was corrected for the envelope and multiplied with a fitted 90 nm FWHM Gaussian window, which would yield 10  $\mu\text{m}$  theoretical resolution in air.

The dispersion mismatch between the two arms of the system was compensated in software by a dispersion search algorithm [3]. Together with the large difference of material dispersion in the two arms, the waveguide dispersion causes a non-linear spectral phase in the interference signal that can be modeled as a high-order polynomial. To overcome strong noise and large error with high-order optimization, the optimization algorithm was split into two independent steps. Step 1: the signal from a mirror was used to find an initial set of dispersion parameters. The search was guided using dispersion parameters obtained from simulated  $TM_{00}$  effective index values with respect to wavelength. Step 2: the obtained spectral phase was set as the starting point for dispersion optimization on the biological signal utilizing the image entropy as a sharpness measure [4]. The final dispersion parameter values were found within a factor of 3 to the parameters found from the simulations. The discrepancy can be attributed to numerical errors in simulations, differences between the simulated and fabricated waveguides and noise in the data. The measured axial resolution of the system was 14  $\mu\text{m}$  with conventional 3<sup>rd</sup> order dispersion correction and reached the theoretical

limit after 10<sup>th</sup> order correction.

For sensitivity estimation, first we measured the sensitivity of an OCT system with fiber-based splitters and a free-space reference arm. The spectrometer, the scanner and the software were the same. The spectrometer camera was operated at 47K A-scans/s. The sensitivities and losses of the fiber and chip-based systems are summarized in Table 4.1. The fiber setup was an OCT system for dermatological imaging operating with 2.5 mW power on the sample. The sensitivity of the system was calculated by the ratio of the peak to the standard deviation of the noise floor around the peak (see Eq. 2.28). The measured sensitivity of this system with 2.5 mW on the sample was 94 dB, while the shot noise limited, lossless system would have 111 dB sensitivity. For the calculation of the shot noise limited sensitivity we used the formula given in Eq. 2.27.

System	Ps ( $\mu$ W)	Sens. shot noise limited (dB)	Sens. meas. (dB)	Spectr. + scanner loss (dB)	Chip losses (dB)	Sens. degr. other (dB)
fiber-based	2500	111	94	7	-	10
fiber-based	100	97	73	7	-	17
with integrated interferometer	100	97	65	7	7.5	17.5

**Table 4.1:** Sensitivities and losses. Ps: power at the sample, Sens. meas. : Sensitivity measured, Sens. degr. : Sensitivity degradation, spectr.: spectrometer.

The setup had a total of 7 dB loss in the sample arm, due the losses at the scanner and the spectrometer. Thus, the system performance was degraded by 10 dB due to other noise sources such as intensity and readout noise. Then we measured the sensitivity of that fiber system at 100  $\mu$ W, which was the maximum power level on the sample achievable with the chip-based OCT system. The measured sensitivity was 73 dB, while shot noise limited sensitivity at that power level would be 97 dB. Taking the 7 dB spectrometer and scanner losses into account, we may conclude that other noise sources degraded the sensitivity by 17 dB. The sensitivity of the system with the integrated interferometer chip was also measured with 100  $\mu$ W on the sample. The sensitivity was 65 dB, which is 8 dB less than the sensitivity of the fiber system using the same

power level on the sample. Considering the 3 dB loss at splitter s2 and the 4.5 dB loss at the fiber-array-to-chip interface, the total loss in the sample arm was 7.5 dB. Here, for simplicity, we ignored the excess losses of the y-splitters ( $2 \times 0.3$  dB) and the propagation loss in the sample arm (0.7 dB) as the fiber splitter used in the fiber setup had around 1 dB excess loss. Thus, except the 7.5 dB extra loss in the sample arm, the sensitivity obtainable with the chip is comparable with the setup with fiber components.

### 4.2.2 *In vivo* human finger skin imaging

To evaluate the system, we imaged a human fingertip and finger mid-joint *in vivo*. The fingertip images shown below in Figure 4.8 are median projection of 100 OCT B-scans (cross-sectional images) to reduce speckle and increase sensitivity by  $\sim 10$  dB. In B-scan images, the axial direction is scaled by 1.33 to account for the refractive index of tissue. Different layers of fingertip such as the stratum corneum (SC), viable epidermis (VE), papillary dermis (PD) and reticular dermis (RD) can be differentiated in the image. The viable epidermis appears as a waved and brightly scattering layer because of the dermal papillae. The dermal-epidermal junction is not well demarcated due to its undulating nature (marked by the yellow dotted curve). The papillary dermis can be identified by the presence of dermal papillae. It is separated from the flat reticular dermis by the less scattering region of rete subpapillare. The dermis appeared as a bright scattering layer. Sweat ducts traversing to the epidermal surface are visible.

The comparison of the two subfigures 4.8a and 4.8b show that higher order dispersion correction is crucial in this system configuration with a highly dispersive reference arm. In the case where even very small values of the higher order coefficients are accounted for (Figure 4.8a), the tomogram appears more crisp and allows to follow the fine structure more precisely. It displays an improved sensitivity that is well evident as an improved visibility of the stratum corneum. The dark region following the reticular dermis is due to signal attenuation with depth as the signals at that depth are below the threshold level. Ideally, below that region we should not see any signal. However, the zero delay line was chosen to be inside the tissue and due to remaining DC and autocorrelation signals, which are dispersed, a bright band appears below the dark region.

Cross-sectional and en-face views of OCT images obtained from the finger mid-joint are shown in Figure 4.9. In the cross sectional image,

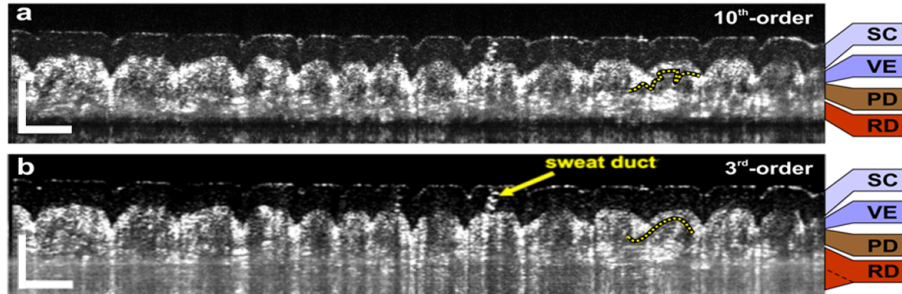


**Figure 4.8:** OCT cross section (sum projection of 100 B-scans) of a fingertip. SC: stratum corneum, VE: viable epidermis, PD: papillary dermis, RD: reticular dermis. The yellow dotted curve marks the dermal-epidermal junction. The scale bars represent  $500\ \mu\text{m}$  length. a) after  $10^{\text{th}}$  order and b) after  $3^{\text{rd}}$  order dispersion compensation.

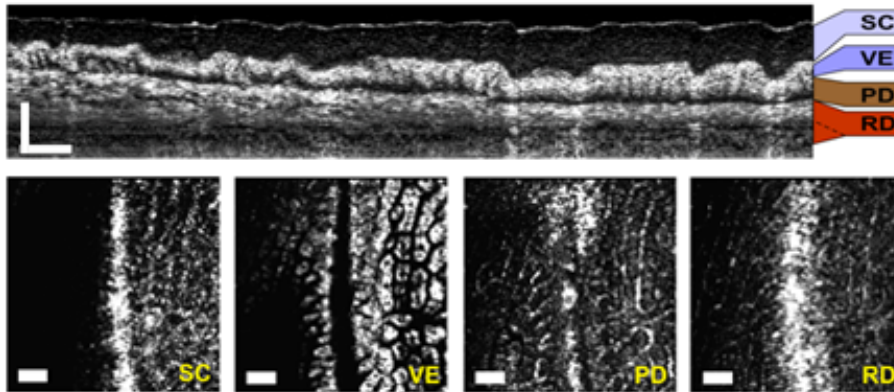


**Figure 4.9:** OCT cross-section (sum projection of 28 B-scans) and en-face views of a finger midjoint. SC: stratum corneum, VE: viable epidermis, PD: papillary dermis, RD: reticular dermis. The scale bars of the cross-sectional image represent  $500\ \mu\text{m}$  length, while the scale bars of the en-face images represent  $1\ \text{mm}$  length.

different epidermal and dermal sub-layers of thick skin are visible. The morphological variations of different skin layers can be seen in the en-face images. The characteristic nature of different layers such as the light-scattering nature of the stratum corneum layer, the epidermal rete ridges in the viable epidermis, dermal papilla in the papillary dermis

and the fiber-rich reticular dermis is seen in these OCT images.

### 4.3 Discussion

The characterization of the system and *in vivo* finger images suggest that  $\text{Si}_3\text{N}_4/\text{SiO}_2$  based box shaped waveguide technology is a viable platform for passive PICs for OCT. As demonstrated in this study, all splitters and the reference arm can be realized on a single substrate within a small area with high-volume manufacturing technology. Furthermore, a single wafer can accommodate tens of such interferometers for parallel OCT. Moreover, implementation on a single substrate will increase the stability of the interferometers. To further increase the appeal of this platform for OCT, there are several opportunities related to coupling efficiency, dispersion, reference arm power adjustment and integration with active components.

The 65 dB sensitivity of the system could be improved in several ways. As shown in Table 4.1, there is a 17 dB additional degradation of the sensitivity, likely to be due to intensity and readout noise. By changing the reference arm power and camera settings, 10 dB higher sensitivity might be obtainable. In an integrated interferometer, the reference arm power can be adjusted by incorporating an integrated broadband variable optical attenuator. Integrated optical attenuators usually consist of a small Mach-Zehnder interferometer with specially designed couplers and phase tuning mechanism [5]. Further reduction in noise can also be achieved by designing the PIC for SS-OCT with balanced detection. Using a Michelson configuration will eliminate the extra splitter (splitter s2) and provide additional 3 dB increase in sensitivity. Obviously, reducing the 4.5 dB fiber to chip coupling loss will also have a significant effect on the sensitivity.

Coupling the light beam efficiently from standard single-mode fibers to PICs is challenging, as the mode-field diameter of integrated waveguides are smaller than the mode-field diameter of the standard single-mode fiber. We used a standard single-mode SMF-28 fiber array that had 4.5 dB loss per coupling to the chip. However, there are options that can provide  $<0.5$  dB loss per coupling. One common solution used to couple light into integrated waveguides is to use lensed fibers where the tip of a standard fiber is shaped to provide a reduced beam waist that can match the mode size of the waveguides. A similar solution is to use ultra-high-numerical-aperture fibers such as UHNA fiber series from Nufern (East Granby, USA). Such fibers can provide mode sizes of few

microns and can be spliced to single-mode fibers with 0.12 dB splicing loss [6]. Another solution to increase the coupling efficiency is to implement spot size converters, which can adiabatically transform the small waveguide mode profile to a larger one [7].

Dispersion compensation is a challenge in an integrated interferometer which consists of dispersive waveguides and has large arm length mismatch. In addition to software compensation, waveguide dispersion minimization should be considered. If design flexibility is provided, dispersion of the waveguides can be further minimized by changing the geometry of the waveguides (e.g. width, height,  $\text{Si}_3\text{N}_4$  layer thickness). For example, simulations of GVD with varying  $\text{Si}_3\text{N}_4$  layer thicknesses, given in Figure 4.10, show that changing the  $\text{Si}_3\text{N}_4$  layer thicknesses from 50 nm to 45 nm, brings the GVD of  $\text{TM}_{00}$  from  $-205 \text{ ps}/(\text{nm km})$  to  $-75 \text{ ps}/(\text{nm km})$ . Further reducing the  $\text{Si}_3\text{N}_4$  layer thickness to 40 nm causes a sign change in the GVD and it becomes  $22 \text{ ps}/(\text{nm km})$ . If  $\text{Si}_3\text{N}_4$  layer thickness can be reproducibly controlled within few nanometers, the GVD can be significantly reduced.

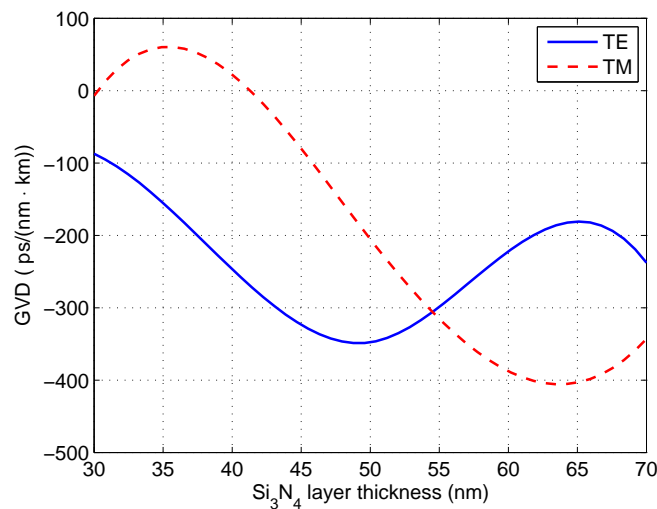


**Figure 4.10:** Simulation of GVD for fundamental TE and TM modes with respect to change in  $\text{Si}_3\text{N}_4$  layer thickness.

To achieve high resolution in OCT, in addition to a broadband source, splitters need to be sufficiently broadband. Y-splitters are broadband, however, they are known to have higher excess loss than direc-

tional couplers. The excess loss of y-splitters is mainly due to the fabrication limited blunt at the junction, which also causes some back reflection. Although directional couplers have smaller bandwidths compared to y-splitters and are more prone to fabrication tolerances, they usually have lower insertion losses than y-splitters and do not have back reflection. Ideally, directional couplers are lossless. Their insertion losses can result due to fabrication related phenomena such as incomplete gap opening during etching or presence of more sidewall roughness inside the gap than outside the gap. As discussed in Chapter 3, an attractive splitter design for OCT is the adiabatic coupler, which is a modified directional coupler consisting of waveguides of varying widths rather than conventional uniform waveguides. Although such couplers are several times longer than general directional couplers, they can be designed to have  $> 200$  nm bandwidth [8].

The box shaped waveguides utilized in this work are birefringent and provide the advantages of polarization maintenance such as improved polarization stability of the interferometer and elimination of the polarization controllers in the sample and reference arms. However, in a birefringent interferometer, light should be coupled to only one of the polarization states. Otherwise, for a single reflector two peaks at different locations would appear, corresponding to each polarization state. In our setup, we optimized the polarization using a paddle based fiber polarization controller to couple the light to the mode with lower GVD; the peak corresponding to the lower GVD mode was sharper and we maximized that peak by adjusting the polarization.

In general, interferometers in OCT systems are Michelson type. The interferometer type does not significantly affect the SNR, as long as it is made from ideal waveguides and is power conserving [9]. However, integrated waveguides are not ideal and have significantly higher loss compared to fibers due to sidewall roughness imposed by current fabrication techniques. As the resolution of lithographic processes improves, the sidewall roughness reduces. The optical loss within waveguides fabricated in this study is  $< 0.14$  dB/cm, while typical fiber loss is  $< 0.35$  dB/km. The roughness on the sidewall of a waveguide scatters the light in all directions and is mostly radiated away, but some of it will scatter backward in the waveguide. In Michelson configuration, backscattering due to the sidewall roughness in the sample and reference arm waveguides can degrade the system performance in high-refractive-index-contrast waveguides, as we demonstrated previously in silicon [10]. In the multi-project wafer run used for this manufacturing step, we had

limited mask space, which was sufficient only for one interferometer and we chose to design a Mach-Zehnder type interferometer, in case sidewall roughness effects are significant. Ideally, different types of interferometers can be fabricated on the same chip and their performances can be compared.

In principle, the waveguide technology employed in this study can be used to design an integrated spectrometer similar to the one demonstrated by Akca et. al [8]. Combining such a spectrometer with an integrated interferometer with an on-chip reference arm will be an important step towards OCT on-a-chip. For a complete integrated OCT system, hybrid integration [11] of an SLED and a photodetector array with this waveguide technology can be investigated.

#### 4.4 Conclusion

We have demonstrated an OCT system that uses a photonic integrated circuit consisting of waveguides, splitters and a reference arm. The system shows a potential of the  $\text{Si}_3\text{N}_4/\text{SiO}_2$  TriPleX<sup>TM</sup> platform for further integration of other OCT components and parallelization. Although we were able to obtain *in vivo* images from a human finger, the sensitivity is 8 dB less than a fiber-based system. Thus, in order to proceed with more complex PICs for OCT using this material system, further optimization is necessary in fiber-to-chip coupling efficiency. Integration approaches of active devices such as light sources and detectors will open a road towards fully integrated OCT systems.



# References

- [1] F. Morichetti, A. Melloni, M. Martinelli, R. G. Heideman, A. Leinse, D. H. Geuzebroek, and A. Borreman, “Box-shaped dielectric waveguides: a new concept in integrated optics?”, *Lightwave Technology, Journal of*, vol. 25, no. 9, pp. 2579–2589, 2007 (cit. on p. 88).
- [2] M. Izutsu, Y. Nakai, and T. Sueta, “Operation mechanism of the single-mode optical-waveguide y junction”, *Optics letters*, vol. 7, no. 3, pp. 136–138, 1982 (cit. on p. 93).
- [3] B. Hofer, B. Považay, B. Hermann, A. Unterhuber, G. Matz, and W. Drexler, “Dispersion encoded full range frequency domain optical coherence tomography”, *Optics express*, vol. 17, no. 1, pp. 7–24, 2009 (cit. on p. 96).
- [4] Y. Yasuno, Y. Hong, S. Makita, M. Yamanari, M. Akiba, M. Miura, and T. Yatagai, “In vivo high-contrast imaging of deep posterior eye by 1-um swept source optical coherence tomography and scattering optical coherence angiography”, *Optics express*, vol. 15, no. 10, pp. 6121–6139, 2007 (cit. on p. 96).
- [5] T. Mizuno, Y. Hashizume, M. Yanagisawa, T. Kitoh, A. Kaneko, and H. Takahashi, “Wideband planar lightwave circuit type variable optical attenuator using phase-generating coupler”, *Electronics Letters*, vol. 42, no. 11, pp. 636–638, 2006 (cit. on p. 100).
- [6] M. Tse, H. Tam, L. Fu, B. Thomas, L. Dong, C. Lu, and P. Wai, “Fusion splicing holey fibers and single-mode fibers: a simple method to reduce loss and increase strength”, *Photonics Technology Letters, IEEE*, vol. 21, no. 3, pp. 164–166, 2009 (cit. on p. 101).
- [7] I. Moerman, P. P. Van Daele, and P. M. Demeester, “A review on fabrication technologies for the monolithic integration of tapers with iii-v semiconductor devices”, *Selected Topics in Quantum Electronics, IEEE Journal of*, vol. 3, no. 6, pp. 1308–1320, 1998 (cit. on p. 101).
- [8] B. Akca, B. Považay, A. Alex, K. Wörhoff, R. de Ridder, W. Drexler, and M. Pollnau, “Miniature spectrometer and beam splitter for an optical coherence tomography on a silicon chip”, *Optics express*, vol. 21, no. 14, pp. 16 648–16 656, 2013 (cit. on pp. 102–103).

- [9] A. M. Rollins and J. A. Izatt, “Optimal interferometer designs for optical coherence tomography”, *Optics letters*, vol. 24, no. 21, pp. 1484–1486, 1999 (cit. on p. 102).
- [10] G. Yurtsever, K. Komorowska, and R. Baets, “Low dispersion integrated michelson interferometer on silicon on insulator for optical coherence tomography”, in *European Conference on Biomedical Optics*, Optical Society of America, 2011, 80910T (cit. on p. 102).
- [11] K. Kato and Y. Tohmori, “Plc hybrid integration technology and its application to photonic components”, *Selected Topics in Quantum Electronics, IEEE Journal of*, vol. 6, no. 1, pp. 4–13, 2000 (cit. on p. 103).

# 5

## Integrated spectrometer based on cascaded ring resonators and arrayed waveguide gratings

Integrated photonics offers several possibilities for miniaturized, low-cost spectrometers. In this chapter, we present the design and characterization of an integrated spectrometer that is based on cascaded ring resonators and arrayed waveguide gratings (AWGs). The spectrometer combines the functionalities of ring resonators and AWGs to provide more output channels and smaller channel spacing compared to what is possible using only a single AWG. It was implemented using silicon-on-insulator (SOI) technology and has 208 channels with 0.15 nm channel spacing. The device has 15-25 dB insertion loss, 20 dB neighbour channel crosstalk and its size is only 1.1 mm  $\times$  5.5 mm.

We will start the chapter with a brief overview of AWGs, ring resonators and cascaded spectrometers. In the second section, we will explain the spectrometer architecture and provide its design parameters. Next, we will present the characterization of the device. Then, we will discuss the possible reasons for some discrepancies between the measurement results and the simulations. Finally, we will close the chapter with conclusions.

The work in this chapter was done in collaboration with Dr. Andrea Trita when he was a postdoctoral researcher in our research group. I designed the spectrometer and Dr. Andrea Trita constructed the measurement setup. We also used an in-house AWG simulation software which was written by Dr. Shibnath Pathak during his PhD studies.

## 5.1 Introduction

High-resolution, multichannel spectrometers are essential for spectroscopic applications and fiber-optic communication systems. Integrated spectrometers are advantageous for mass production, low-cost, small size and integration with other optical components. On-chip spectrometers would enable cheap, miniature devices for chemical sensing [1], medical diagnosis [2] and spectral-domain optical coherence tomography [3].

Integrated wavelength-selective devices have been developed over many years for multiplexing and demultiplexing optical signals in fiber-optic communication systems to increase their transmission capacity. Specifically, the arrayed waveguide grating (AWG), a phased-array-like spectrometer termed as multiplexer/demultiplexer in telecommunication applications, has gained much attention. Another type of wavelength selective device is the ring resonator, which has frequently been investigated for add-drop filters in optical communications [4] and sensing applications [5]. A ring resonator is similar to a Fabry-Perot resonator; however, it has a circular cavity rather than a straight one. Like a Fabry-Perot resonator, its transmission spectrum exhibits peaks corresponding to the resonances of the ring cavity. The working principles of the AWG and the ring resonator are briefly presented in the next subsections. We also review how cascades of multiple wavelength-selective components have been used to enhance the properties of integrated spectrometers.

### 5.1.1 AWG

A schematic of an AWG is given in Figure 5.1. An AWG consists of an input waveguide, a diffraction region, an array of waveguides, a refocusing region and output waveguides. The diffraction and the refocusing regions are slabs and light propagates in the slab. The light from the input waveguide diffracts in the diffraction region and at the input aperture couples into the waveguide array. The waveguides guide the light to the output aperture and have a constant length increment between each other. When the light in the individual waveguides arrives at the

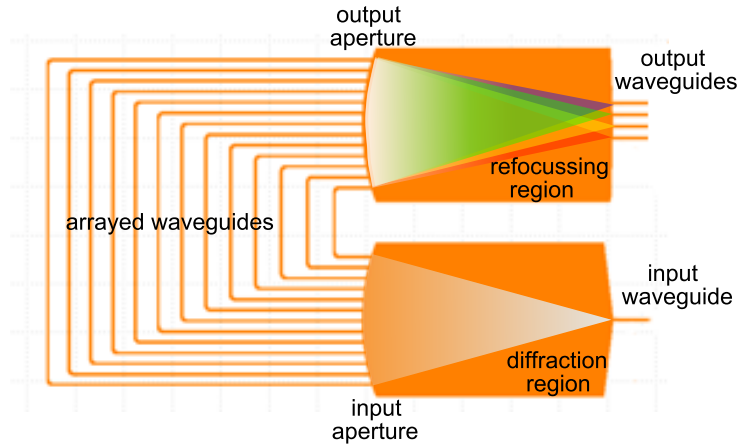


**Figure 5.1:** Illustration of an AWG.

output aperture, the constant length difference between the waveguides results in a constant phase difference. Thus, the waveguide array acts similar to a phased array antenna and the phase difference is a function of wavelength. The output aperture focuses the light into the output waveguides. As a result of the wavelength dependence of the phase difference, different wavelengths are focused to different positions at the focus plane. The output waveguides are placed at the focus plane and constitute the output channels.

The wavelength span between different diffraction orders of an AWG, namely the free spectral range (FSR), depends on the path length difference between consecutive waveguides and is given by

$$FSR_{AWG} = \frac{\lambda_c^2}{\Delta L n_g} \quad (5.1)$$

where  $\lambda_c$  is the center wavelength,  $\Delta L$  is the length difference between two successive waveguides and  $n_g$  is the group index of the waveguides.

AWGs with best performance parameters are fabricated using silica waveguides [6]. An AWG in silica at 1550 nm center wavelength with 400 channels and 25 GHz (0.2 nm) channel spacing has been fabricated by Hida et al. [7]. Fabricating AWGs on high-index-contrast material systems such as silicon-on-insulator (SOI), can reduce their size almost by two decades. However, at smaller dimensions AWGs are prone to fabrication-related deviations from the design geometry. Small changes in waveguide dimensions cause significant phase errors. Current AWGs

demonstrated in SOI have much smaller number of output channels and their channel spacing is larger than the silica ones. Recently, Pathak et al. reported on a 16 channel AWG with 200 GHz channel spacing in SOI [8]. Using only a single AWG for implementing spectrometers with large channel-count and small channel-spacing in SOI is not feasible yet due to fabrication limitations.

### 5.1.2 Ring resonator

A ring resonator consists of a circular optical cavity which is coupled to one or two access waveguides. An illustration of a ring resonator with two access waveguides is shown in Figure 5.2. Light from the input port of the bottom access waveguide couples to the ring cavity and the wavelengths satisfying the resonance condition interfere constructively in the ring cavity. A portion of the light resonating in the cavity couples to the top access waveguide and leaves the resonator from the drop port. Non-resonant wavelengths coming from the input port leave the resonator at the through port. At resonance, the optical path length of the ring resonator is an integer multiple of the resonance wavelengths. The resonance condition for a ring resonator is given by

$$n_{eff}L = m\lambda_r \quad (5.2)$$

where  $n_{eff}$  is the effective refractive-index of a guided mode in the ring waveguide,  $L$  is the round-trip length of the ring,  $m$  is the resonance order and  $\lambda_r$  is the resonance wavelength.

The separation between two consecutive resonance orders, FSR, at  $\lambda_o$  is given by

$$FSR_{ring} = \frac{\lambda_o^2}{n_g L} \quad (5.3)$$

where  $n_g$  is the group index of the guided mode and  $L$  is the round-trip length of the ring.

The quality factor (Q) of a ring resonator is expressed as the ratio of the resonance wavelength  $\lambda_r$  and the full width at half maximum (FWHM) of the resonance,  $\delta\lambda_{res}$ . In order to obtain high-Q resonances, it is necessary to reduce the losses in the resonator; such as round-trip losses in the cavity and coupling losses in the directional couplers.

The resonance width of SOI ring resonators is limited by resonance-peak splitting. This resonance-peak splitting phenomenon is due to backscattering caused by sidewall roughness [9]. From our research

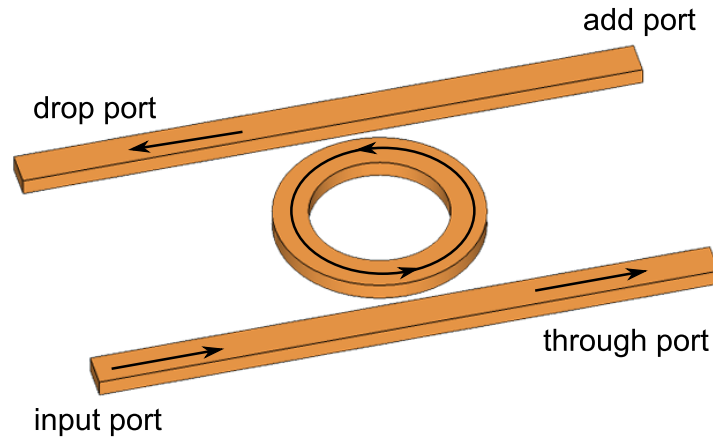


**Figure 5.2:** Illustration of a ring resonator. The arrows indicate the direction of the light in resonance condition, when light is injected from the input port.

group, De Heyn et al. demonstrated that by using shallow-etched rib waveguides rather than ridge waveguides, the  $Q$  of ring resonators can be improved [10]. Using shallow-etched rib waveguides, he fabricated ring resonators which have  $< 0.085$  nm FWHM resonance peaks [11].

### 5.1.3 Cascaded spectrometers

Integrated spectrometers have also been designed by combining several frequency-selective components. Takada et al. used multiple AWGs to design a spectrometer with increased number of channels and a broader spectrum of operation. Using silica waveguides, they realized a spectrometer with more than 1000 channels and 10 GHz channel spacing [12]. This impressive result was achieved by cascading a coarse-resolution AWG with five channels as a primary filter and five 10 GHz spaced AWGs with 288 channels as secondary filters in a tandem configuration.

Kyotoku et al. implemented a spectrometer in SOI by cascading a ring resonator and a planar diffraction grating (termed also as planar concave grating or echelle grating in the literature). In their design, the ring resonator had a high- $Q$  and was the primary filter, while the planar diffraction grating was used as the secondary filter [13]. The schematic of their design is depicted in Figure 5.3a. The ring resonator prefilters the light and the diffraction grating spectrometer separates the resonances of the ring resonator; the FSR of the ring resonator and the channel spacing of the diffraction grating spectrometer are matched. The spec-

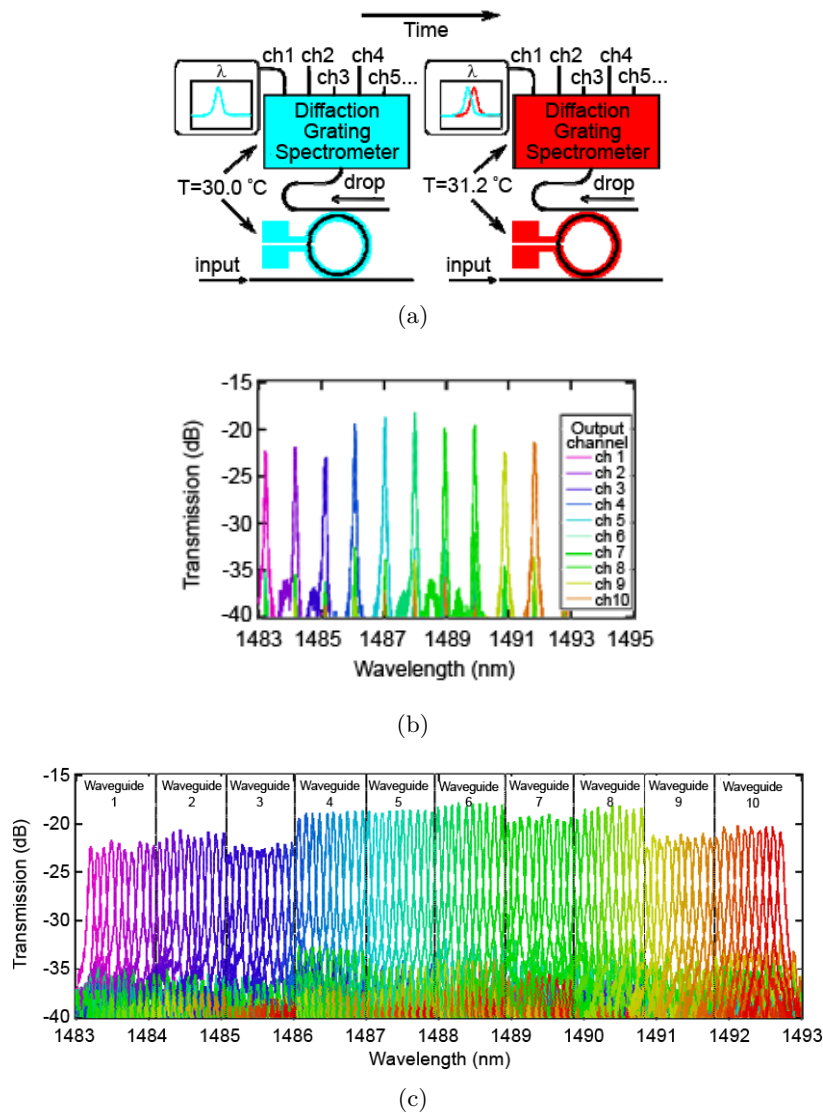


**Figure 5.3:** Figures from the study by Kyotoku et al. [13]. a) Schematic of the spectrometer and its operational principle based on thermal tuning. Transmission spectrum for the combined ring and diffraction grating spectrometer b) without thermal tuning. c) with thermal tuning.

tral response of their device is plotted in Figure 5.3b. Their planar diffraction grating had 10 channels with channel spacing of 1 nm, the FWHM resonance width of the ring resonator was 0.05 nm. In order to

sample the whole spectrum supported by the device, the ring resonator was thermally tuned using a metal heater deposited on top of the ring resonator. The transmission spectrum obtained by thermally shifting the resonance peaks of the ring resonator is given in Figure 5.3c.

We designed a cascaded spectrometer based on the ideas mentioned in the previous paragraphs; a spectrometer with primary and secondary filters. More specifically, we extended the work reported by Kyotoku et al. [13]. Rather than using a single pair of filters, we used 13 ring resonator - AWG pairs. This parallel architecture eliminates the need of continuous tuning of the ring resonator to measure the spectrum and can enable faster read-out rate. In the following section, we explain the design of our spectrometer.

## 5.2 Design

The architecture of our spectrometer is based on cascaded ring resonators and AWGs. An illustration of the proposed spectrometer is given in Figure 5.4. The spectrometer consists of the 13 ring resonators with sharp resonances and 13 AWGs with coarse channels. To understand the operation of the spectrometer, let's consider initially only the first ring resonator - AWG pair in the figure. For light with a broadband spectrum coming from the input port, only resonance wavelengths will couple constructively into the ring cavity and exit at the drop port, while non-resonant wavelengths will go to the through port. The light at the drop port, before entering the AWG, will have a comb-like spectrum. The peaks in this spectrum correspond to the resonance wavelengths of the ring. If the ring resonator FSR and the AWG channel spacing are matched and aligned with each other, each AWG channel will output a peak from the comb-like spectrum. Simulated transmission spectra of a ring resonator and an AWG are given in Figure 5.5a; the ring resonator transmission curve is plotted in black and the AWG channels are indicated in color. The AWG was simulated using a semi-analytical model and the ring resonator was simulated using a frequency domain simulation package (Caphe) [14]; both simulation tools are available in the IPKISS integrated photonics design software (Luceda Photonics, Belgium) [15]. The transmission spectrum of their cascade is given in Figure 5.5b. The spectral resolution at the output channels, which is normally defined by the AWG, is now determined by the resonance width of the ring resonator.

By using only one ring resonator - AWG pair, the spectrum is sam-

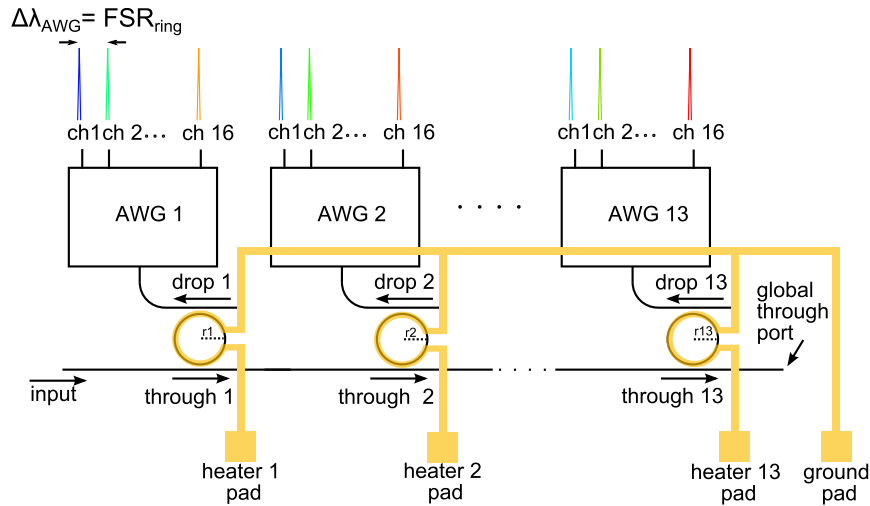


**Figure 5.4:** Schematic of the spectrometer consisting of 13 cascaded ring resonators and 13 AWGs. Each ring resonator - AWG pair measures a comb-like spectrum which is slightly red-shifted with respect to a previous pair.  $\Delta\lambda_{AWG}$ : AWG channel spacing,  $\delta\lambda_{res}$ : 3 dB resonance width of the ring resonators.

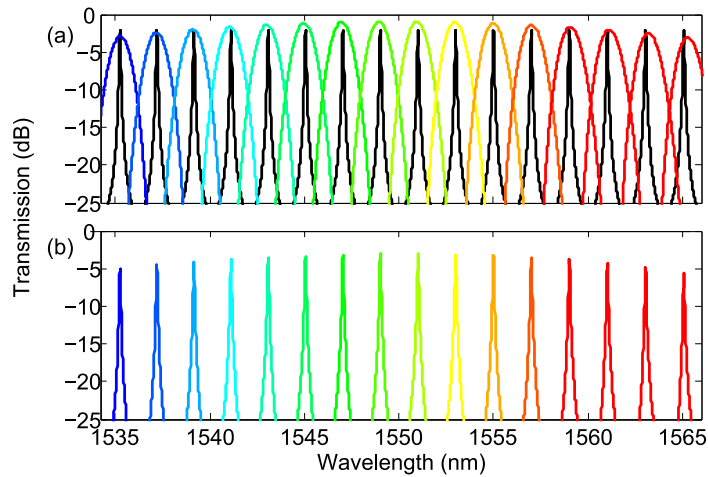


**Figure 5.5:** a) Simulated transmission spectra of a ring resonator (black) and a 16 channel AWG (color). The ring resonator FSR and the AWG channel spacing are matched, b) Transmission spectrum of the cascade of the ring resonator and the AWG in (a).

pled with a comb-like function; the spectral range between the resonance peaks remains unsampled. Using multiple ring resonator - AWG pairs, we can sample the whole spectrum provided that consecutive pairs have shifted comb-like transmission spectra. The shift between the peaks of consecutive ring resonators will be the channel spacing of the spectrometer. In our design, to shift the spectral responses of consecutive rings, their radius is slightly increased. However, due to fabrication limitations, the position of the ring resonator peaks usually deviates from the design. To align the peak positions of the rings and have a certain shift between them, metal heaters are deposited above the ring resonators. The refractive index of silicon has a large temperature dependent coefficient and increasing the temperature of the cavity waveguide causes a red-shift in the spectral response of a ring resonator [16]. Once the alignment of the ring resonance positions is done, the current provided to the heaters is kept constant.

Let's denote AWG channel spacing as  $\Delta\lambda_{AWG}$  and the desired channel spacing of the spectrometer (the shift between the resonances of two consecutive rings) as  $\delta\lambda_{spec}$ . The channel spacing of all AWGs is designed as 243.5 GHz; for wavelengths around 1550 nm it corresponds to  $\Delta\lambda_{AWG} = 1.95$  nm. The ring resonator peaks are shifted by  $\delta\lambda_{spec} = 0.15$  nm with respect to each other. If  $\Delta\lambda_{AWG} = N\delta\lambda_{spec}$ ,  $N$  being an integer, we can evenly sample the spectrum using  $N$  ring resonator - AWG pairs. In our design  $N$  is  $1.95 \text{ nm}/0.15 \text{ nm} = 13$ , thus we need 13 ring resonator - AWG pairs. Each AWG has 16 channels and with these parameters we obtain a 208 (13x16) channel spectrometer with 0.15 nm channel spacing. The resolution of the spectrometer depends on the resonance widths of the rings. The ring resonators are designed to have FWHM resonance widths of  $\delta\lambda_{res} = 0.05$  nm. By having the resolution much smaller than channel spacing, neighbour channel crosstalk is reduced.

In our design, the center wavelength of the AWG in the middle of the spectrometer (AWG number 7) is set to 1550 nm and consecutive AWGs have a center wavelength difference by  $\delta\lambda_{spec} = 0.15$  nm. The resonance peak positions of the consecutive ring resonators are also shifted by  $\delta\lambda_{spec}$ . The FSR of the ring resonators are matched to AWG channel spacing  $\Delta\lambda_{AWG}$ . The radius of ring-resonator number 7 (the middle one) was set to 52.15  $\mu\text{m}$  to achieve 1.95 nm FSR. The radius of consecutive rings differ by 10 nm to shift their resonance peak positions by 0.15 nm. Changing the radius of a ring also changes its FSR, but it is insignificant. The waveguides of the ring resonators and the access waveguides are

shallow-etched rib waveguides, with 220 nm height, 70 nm shallow etch, and 450 nm width. The gap between the ring and both access waveguides is 600 nm. In the next section, we explain how the spectrometer was fabricated and present measurement results.

## 5.3 Fabrication and characterization

### 5.3.1 Fabrication

The device was fabricated on a 200 mm SOI wafer with 220 nm thick Si top layer using 193 nm deep-UV lithography. The waveguide structures were covered with 0.8  $\mu\text{m}$  planarized oxide. The fabrication was done through the ePIXfab silicon photonics platform [17]. The name of the specific ePIXfab multi-project-wafer run was SIPP07. An image of the fabricated spectrometer is shown in Figure 5.6a. The figure shows all 13 ring resonator - AWG pairs. The metal lines of the heaters are also visible in the image (gold color). The size of the spectrometer is only 1.1 mm  $\times$  5.5 mm. A more detailed image of the second ring resonator - AWG pair is given in Figure 5.6b. All input and output waveguides are connected to grating couplers. We also included a second input to the AWGs to test their spectral response. A magnified image of the first ring resonator is presented in Figure 5.6c. The top and bottom access waveguides, the ring and the heater are clearly visible; the heater sits on top of the ring cavity. The heaters were fabricated in our cleanroom using contact-mask lithography. The top planarized oxide layer acts as a spacer between the waveguide and the metal, so that the evanescent fields are not absorbed by the metal. Metal heaters are deposited in two steps: first a 100 nm thick Ti (titanium) layer and then a 20 nm gold layer. The Ti layer acts as a resistance and the gold layer prevents oxidation of the Ti. More details on heater fabrication on SOI can be found in the PhD thesis of Karel Van Acoleyen [18].

### 5.3.2 Characterization

First, we characterized the grating couplers. The grating couplers were designed to have 1550 nm peak transmission with air-cladding; however, they should have been designed by considering the top oxide layer. The oxide layer on top of the grating couplers shifted the peak transmission to 1527 nm. A similar shift is also observed when index-matching liquid is used between the fiber and the chip [19]. Because of this shift we did the measurements around 1527 nm rather than 1550 nm. The insertion

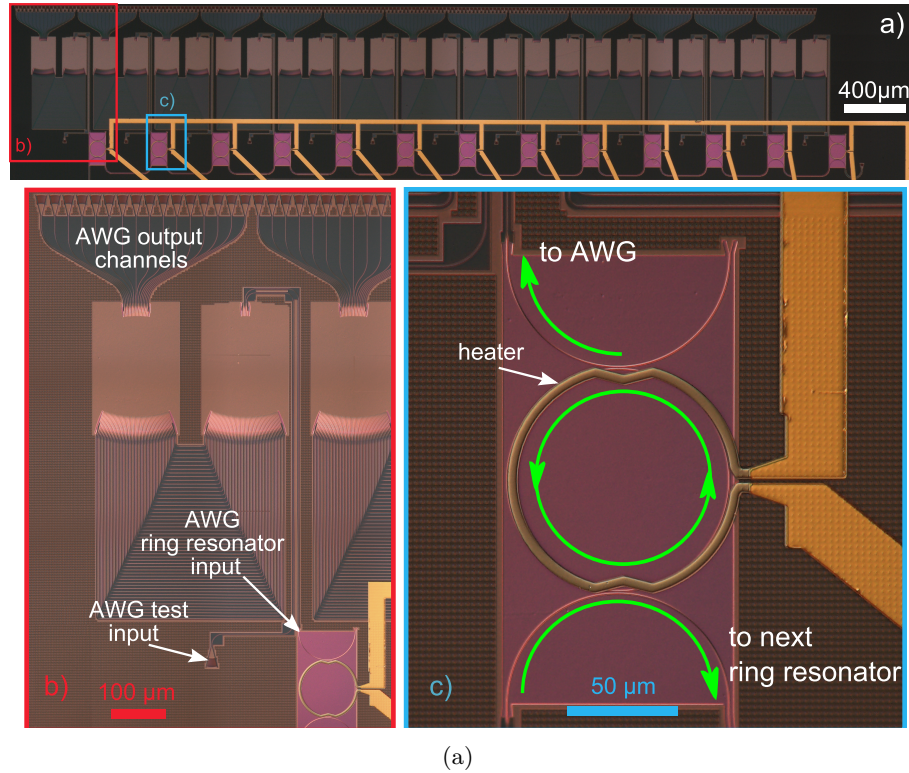
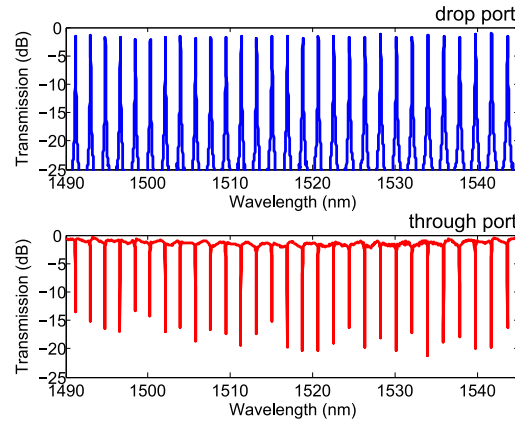


**Figure 5.6:** A microscope image of the fabricated spectrometer. a) All 13 ring resonator - AWG pairs. b) The first ring resonator - AWG pair. c) Magnified image of the second ring-resonator. The green arrow indicate the propagation direction of the light.

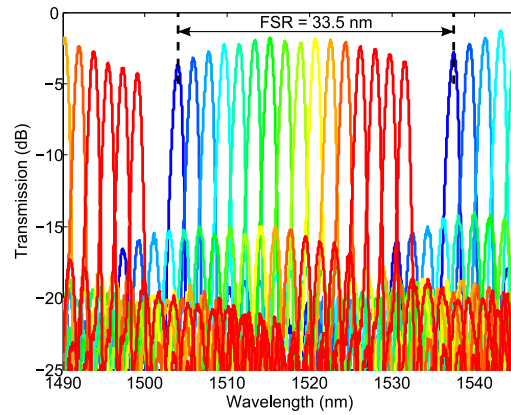
loss of the grating couplers was 5.5 dB and they had a 3 dB bandwidth of 40 nm. The transmission spectra of structures presented in this section are all normalized to grating coupling losses.

Before characterizing the whole spectrometer, we measured the transmission spectrum of a ring resonator test structure and an AWG test structure. The transmission spectrum of the drop and through ports of the ring-resonator is plotted in Figure 5.7a. The insertion loss at the drop port was 1.8 dB and FWHM of the resonance peaks was 0.06 nm. The transmission spectrum of the AWG is plotted in Figure 5.7b. The AWG had 1.8 dB insertion loss, 20 dB neighbour channel crosstalk and 33.5 nm FSR. The 3 dB bandwidth of the AWG channels was 1 nm. The channel spacing of the AWG was 1.84 nm and the FSR of the ring res-

onator was 1.88 nm; matching quite closely. The difference of 0.04 nm corresponds to 0.6 nm shift over 16 channels (15 intervals). That would cause additional 1 dB loss for the channels at the very edges as they would be 0.3 nm shifted from the corresponding AWG peaks.



(a)



(b)

**Figure 5.7:** Measured transmission spectra of a ring resonator and an AWG test structures.(a) Ring resonator transmission spectrum for drop port (top) and through port (bottom). (b) AWG transmission spectrum.

We measured the transmission spectrum of the spectrometer by using a tunable laser and measuring the transmission of each channel as a function of wavelength. The measurement setup devised to characterize the integrated spectrometer is sketched in Figure 5.8. Light generated from a tunable laser source was coupled to the integrated spectrome-

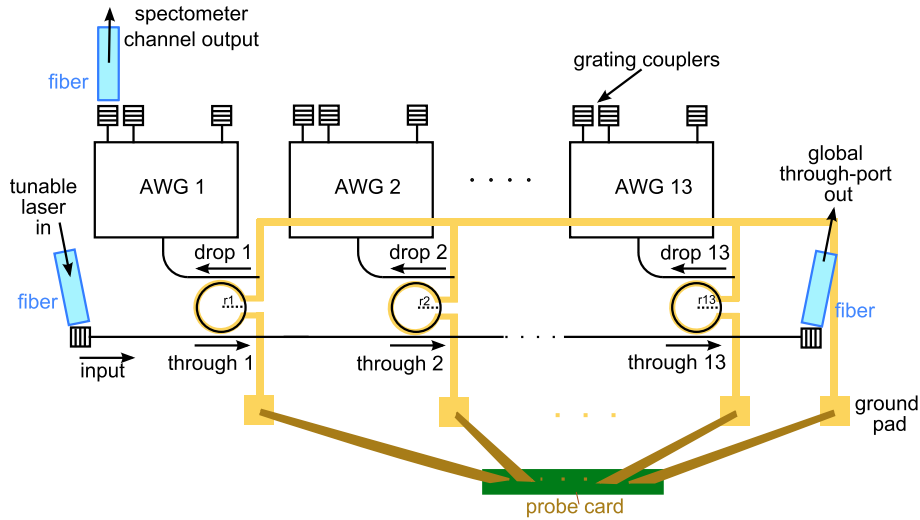
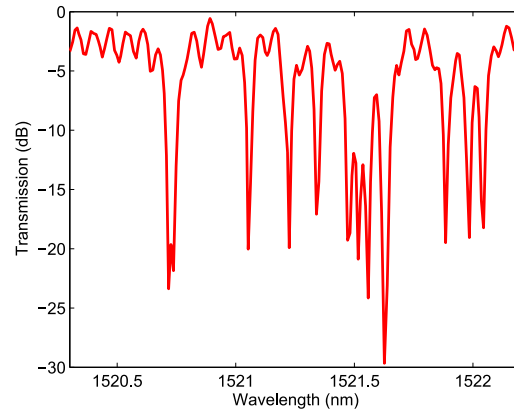


**Figure 5.8:** Measurement set-up. For simplicity only three ring resonator - AWG pairs are depicted.

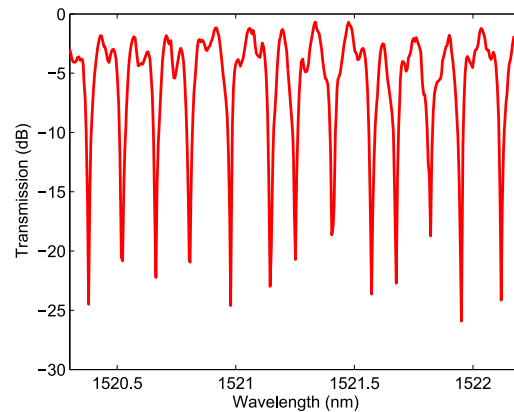
ter using a grating coupler. The wavelength of the tunable laser was swept and the corresponding power transmitted by each spectrometer channel was recorded. Before starting the optical characterization of the device, the spectral response of the ring resonators had to be tuned. Due to fabrication related imperfections, the resonance wavelength positions of consecutive ring resonators differed from the design. To this aim, integrated heaters fabricated on top of the ring resonators were individually thermally tuned. Thermal tuning was achieved via a custom software that controls a multiple-channel voltage/current analog output card. We monitored the power transmitted from the global through-port and provided current to each heater until the peaks were shifted to the desired positions. The transmission spectra of the global through-port of the ring resonators, before and after tuning the ring resonators, are presented in Figure 5.9.

After thermally tuning the ring resonators, we characterized the transmission spectrum of the spectrometer by measuring the individual AWG channel outputs, total of 208 outputs. Figure 5.10a shows the device transmission for all channels. The transmission is normalized for fiber-to-chip coupling losses. In Figure 5.10b, the central channels are plotted to show more detail.

The insertion loss of the channels, excluding grating couplers losses,



(a)



(b)

**Figure 5.9:** Ring resonator global pass-port response. (a) Before thermal tuning of the ring resonators. (b) After thermal tuning of the ring resonators.

varies mainly between 4 dB-15 dB. The insertion loss non-uniformity become worse towards the right edge of the spectrum. One reason is the inherent insertion loss of the AWGs at the edges. Other reasons are probably the sub-optimal positions of the ring resonances with respect to AWG channels and the mismatch of the AWG channel spacings and ring resonator FSRs. From Figure 5.10b, we see that the ring resonances are not tuned perfectly and the spacing between them varies. In this figure, the resonance of the ring 12 is missing. An experiment to measure all 208 channels took around 5 hours, and it seems that during this specific experiment the contact to heater 12 had a problem after the initial

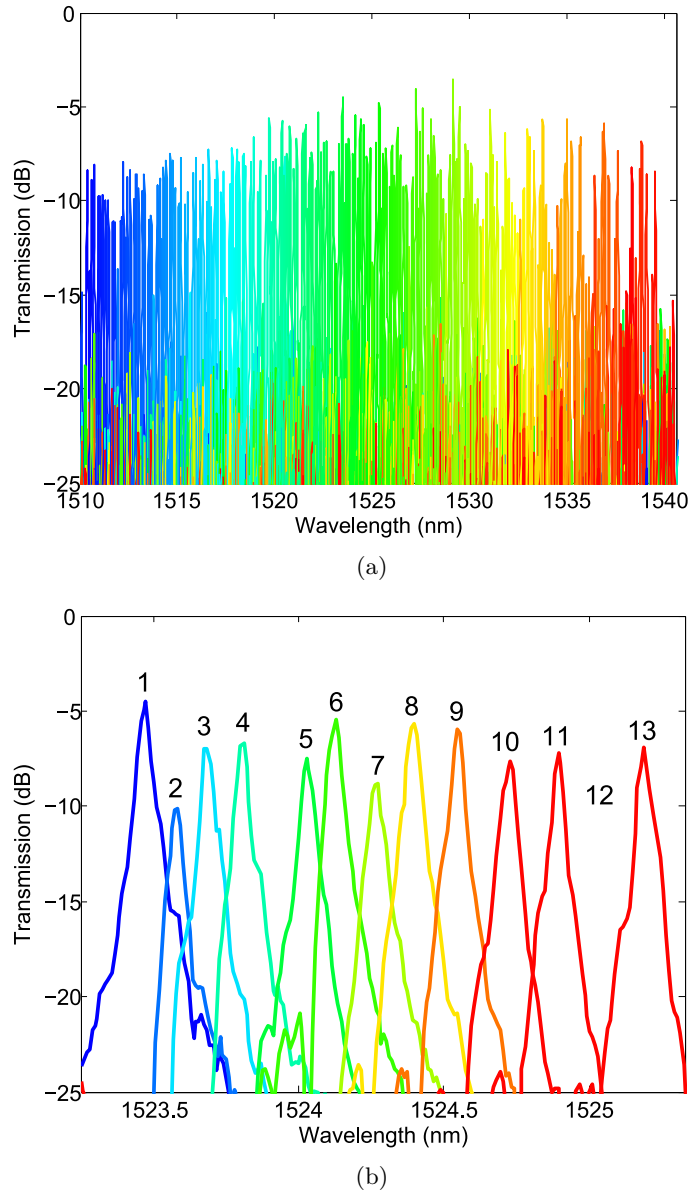


**Figure 5.10:** a) Superposition of 208 transmission spectra of the spectrometer. (b) Transmission spectra of the mid channels only, to show more detail.

alignment. We realized the problem only after analyzing the whole data set. In another data set, the resonance of ring 12 was observed. The

FWHM of the resonances is 0.06 nm.

## 5.4 Discussion

Although silicon photonics technology is constantly improving, we are still far away from fabricating a high-resolution multi-channel spectrometer using a single AWG in SOI. Due to imperfect waveguides (e.g. local width and thickness variations), optical path lengths deviate from the design and this deviation translates into phase errors. Phase errors enlarge the spot sizes at the focus plane and channel crosstalk increases. Rather than using an AWG, structures with sharp resonances in combination with AWGs can be a solution to realize high-resolution spectrometers. However, the resonance positions of cavities such as ring resonators are extremely sensitive to fabrication related variations. For that reason, the resonance positions of cavity-based structures need to be tuned. A permanent solution to the resonance shift of a cavity is to trim its optical path length by varying the effective index of the guided mode in permanent ways such as electron beam induced compaction of oxide [20] and nanomilling using a femtosecond laser [21].

A small mismatch between the ring-resonator FSR and the AWG channel spacing cause a misalignment between the resonance peaks and the AWG channels. This mismatch builds up from one channel to the next in a Vernier effect, increasing the insertion loss. Thus, while cascading devices, such possible mismatches need to be taken into account.

Optimal tuning of the ring resonators is difficult without monitoring the spectrometer outputs in parallel and real time. After measuring the spectrometer output channels one by one, we realized that the positions of some of the ring resonance peaks are not matching well with the corresponding AWG channels. By imaging the output channels to a photodetector array, a more precise tuning can be done. Moreover, by integrating a photodetector array on top of the grating couplers, a more practical spectrometer can be realized. With such a fixed read-out, the variability in the insertion losses can be easily compensated in software. In the context of the SmartFiber project, integration of a photodetector array on AWG outputs was demonstrated [22], [23].

## 5.5 Conclusion

We demonstrated that by using cascaded ring resonators and AWGs, it is possible to design a spectrometer which benefits from spectral filter-

---

ing properties of both devices. The spectrometer resolution is decoupled from the channel width of the AWGs and is determined by the resonance widths of the ring resonators. By using 13 cascaded ring resonator - AWG pairs, we demonstrated a spectrometer with 0.06 nm resolution and 208 channels. To the best of our knowledge, this is the spectrometer with most number of channels implemented in SOI. We anticipate that the combination of different, wavelength selective components in SOI can enable low-cost, compact, high resolution spectrometers. For a spectrometer operating in the visible region, the concept can also be used with other material systems such as  $\text{Si}_3\text{N}_4$ .



## References

- [1] M. N. Fiddler, I. Begashaw, M. A. Mickens, M. S. Collingwood, Z. Assefa, and S. Bililign, “Laser spectroscopy for atmospheric and environmental sensing”, *Sensors*, vol. 9, no. 12, pp. 10 447–10 512, 2009 (cit. on p. 108).
- [2] I. J. Bigio and S. G. Bown, “Spectroscopic sensing of cancer and cancer therapy: current status of translational research”, *Cancer biology & therapy*, vol. 3, no. 3, pp. 259–267, 2004 (cit. on p. 108).
- [3] J. de Boer, “Spectral/fourier domain optical coherence tomography”, in *Optical coherence tomography: technology and applications*, W. Drexler and J. G. Fujimoto, Eds., Springer Science & Business Media, 2008 (cit. on p. 108).
- [4] P. D. Heyn, J. Luo, S. Di Lucente, N. Calabretta, H. J. Dorren, and D. Van Thourhout, “In-band label extractor based on cascaded si ring resonators enabling 160 gb/s optical packet switching modules”, *Journal of Lightwave Technology*, vol. 32, no. 9, pp. 1647–1653, 2014 (cit. on p. 108).
- [5] K. De Vos, I. Bartolozzi, E. Schacht, P. Bienstman, and R. Baets, “Silicon-insulator microring resonator for sensitive and label-free biosensing”, *Optics express*, vol. 15, no. 12, pp. 7610–7615, 2007 (cit. on p. 108).
- [6] C. R. Doerr and K. Okamoto, “Advances in silica planar lightwave circuits”, *Journal of lightwave technology*, vol. 24, no. 12, pp. 4763–4789, 2006 (cit. on p. 109).
- [7] Y. Hida, Y. Hibino, T. Kitoh, Y. Inoue, M. Itoh, T. Shibata, A. Sugita, and A. Himeno, “400-channel arrayed-waveguide grating with 25 ghz spacing using 1.5 - delta waveguides on 6-inch si wafer”, *Electronics Letters*, vol. 37, no. 9, pp. 576–577, 2001 (cit. on p. 109).
- [8] S. Pathak, M. Vanslebrouck, P. Dumon, D. Van Thourhout, P. Verheyen, G. Lepage, P. Absil, and W. Bogaerts, “Effect of mask discretization on performance of silicon arrayed waveguide gratings”, *IEEE Photon. Technol. Lett*, vol. 26, no. 7, pp. 718–721, 2014 (cit. on p. 110).
- [9] B. E. Little, J.-P. Laine, and S. T. Chu, “Surface-roughness-induced contradirectional coupling in ring and disk resonators”, *Optics letters*, vol. 22, no. 1, pp. 4–6, 1997 (cit. on p. 110).

- 
- [10] P. De Heyn, D. Vermeulen, T. Van Vaerenbergh, B. Kuyken, and D. Van Thourhout, “Ultra-high  $q$  and finesse all-pass microring resonators on silicon-on-insulator using rib waveguides”, *Proc. ECIO2012, Florence*, 2012 (cit. on p. 111).
- [11] P. D. Heyn, “Receivers based on silicon ring resonators for multi-wavelength optical interconnects”, PhD thesis, Ghent University, 2014 (cit. on p. 111).
- [12] K. Takada, M. Abe, T. Shibata, and K. Okamoto, “Low-loss 10-ghz-spaced tandem multi/demultiplexer with more than 1000 channels using a  $1 \times 5$  interference multi/demultiplexer as a primary filter”, *Photonics Technology Letters, IEEE*, vol. 14, no. 1, pp. 59–61, 2002 (cit. on p. 111).
- [13] B. B. Kyotoku, L. Chen, and M. Lipson, “Sub-nm resolution cavity enhanced microspectrometer”, *Optics express*, vol. 18, no. 1, pp. 102–107, 2010 (cit. on pp. 111–113).
- [14] M. Fiers, T. Van Vaerenbergh, K. Caluwaerts, D. Vande Ginste, B. Schrauwen, J. Dambre, and P. Bienstman, “Time-domain and frequency-domain modeling of nonlinear optical components at the circuit-level using a node-based approach”, *JOSA B*, vol. 29, no. 5, pp. 896–900, 2012 (cit. on p. 113).
- [15] W. Bogaerts, P. Dumon, E. Lambert, M. Fiers, S. Pathak, and A. Ribeiro, “Ipkiss: a parametric design and simulation framework for silicon photonics”, in *Proc. 9th IEEE Int. Conf. Group IV Photonics*, 2012, pp. 30–32 (cit. on p. 113).
- [16] D. Dai, L. Yang, and S. He, “Ultrasmall thermally tunable microring resonator with a submicrometer heater on si nanowires”, *Journal of Lightwave Technology*, vol. 26, no. 6, pp. 704–709, 2008 (cit. on p. 115).
- [17] ePIXfab - The silicon photonics platform, 2015, <http://www.epixfab.eu> (cit. on p. 116).
- [18] K. V. Acoleyen, “Nanophotonic beamsteering elements using silicon technology for wireless optical applications”, PhD thesis, Ghent University, 2012 (cit. on p. 116).
- [19] D. Taillaert, “Grating couplers as interface between optical fibres and nanophotonic waveguides”, PhD thesis, Ghent University, 2004 (cit. on p. 116).
- [20] J. Schrauwen, D. Van Thourhout, and R. Baets, “Trimming of silicon ring resonator by electron beam induced compaction and strain”, *Optics express*, vol. 16, no. 6, pp. 3738–3743, 2008 (cit. on p. 122).
- [21] D. Bachman, Z. Chen, A. M. Prabhu, R. Fedosejevs, Y. Y. Tsui, and V. Van, “Femtosecond laser tuning of silicon microring resonators”, *Optics letters*, vol. 36, no. 23, pp. 4695–4697, 2011 (cit. on p. 122).

- 
- [22] SMARTFIBER - Miniaturized structural monitoring system with autonomous readout micro-technology and fiber sensor, 2015, <http://www.smartfiber-fp7.eu> (cit. on p. 122).
- [23] A. Trita, E. Voet, J. Vermeiren, D. Delbeke, P. Dumon, S. Pathak, and D. Van Thourhout, "Simultaneous interrogation of multiple fiber bragg grating sensors using an arrayed waveguide grating filter fabricated in soi platform", *to be submitted*, (cit. on p. 122).



# 6

## Conclusions and perspectives

### 6.1 Conclusions

In this work we investigated the use of passive integrated photonics components to miniaturize Fourier Domain OCT (FD-OCT) systems. More specifically, we used silicon-on-insulator (SOI) and TriPleX<sup>TM</sup> platforms to design Mach-Zehnder interferometers with on-chip reference arms for FD-OCT operating around 1300 nm. Using these interferometers we were able to demonstrate OCT imaging. In addition to the interferometers, we report on a 208 channel spectrometer based on cascaded ring resonators and arrayed waveguide gratings (AWGs) in SOI.

The Mach-Zehnder interferometer fabricated in SOI consists of waveguides, grating couplers, three  $2 \times 2$  splitters, a 130 mm on-chip reference arm with 13 cm length. Thanks to the compact SOI waveguides with small bend radii, the size of the integrated interferometer is only  $5 \text{ mm} \times 0.75 \text{ mm}$ . In our design, we preferred shallow-etched rib waveguides over ridge waveguides as they have lower sidewall scattering and propagation loss. The grating couplers are used to couple light in and out of the chip. In order to reduce the effect of back-reflections at the waveguide and grating coupler interfaces, we used tilted grating couplers. These grating couplers have 7.5 dB insertion loss and a 45 nm 3 dB bandwidth. The grating couplers were designed to transmit

only TE polarization and the waveguides were polarization maintaining. Splitters used in OCT interferometers need to have a flat splitting ratio over a large bandwidth (typically 100 nm). Adiabatic couplers split the light with a fairly flat splitting ratio over several hundred nanometers. Moreover, they do not have internal reflections as multi-mode interference splitters. For our interferometer, we designed  $2 \times 2$  adiabatic couplers which have a splitting ratio of 45:55 at 1266 nm and 30:70 at 1356 nm. Even though our adiabatic couplers have a flatter splitting ratio than directional couplers, they can be further improved by optimizing the design parameters. There are several advantages of using an on-chip reference arm: it eliminates the need of an external reference arm, reduces the size of the optical setup and improves the stability of the interferometer. However, the dispersion introduced in the reference arm needs to be compensated numerically in software. For numerical dispersion compensation, we measured the reflection from a mirror in the sample arm to obtain a clean interference signal. From the measured interference fringes, we found the dispersion coefficients by fitting a third order polynomial to its phase and used them for dispersion compensation. Using the integrated interferometer together with a swept-source laser centered at 1312 nm with 92 nm tuning range, balanced photodetectors and an x-y scanner, we build a swept-source OCT (SS-OCT) system. The SS-OCT system with the chip had 25.5  $\mu\text{m}$  axial resolution, which was limited by the bandwidth of the grating couplers (3 dB bandwidth: 45 nm). We measured the sensitivity of the system as  $-62$  dB with 115  $\mu\text{W}$  power delivered to the sample. The sensitivity can be significantly ( $\sim 20$  dB) improved by using grating couplers or spot size converters with low insertion loss. Using the system, we demonstrated cross-sectional OCT imaging of a layered tissue-mimicking material.

We also investigated TriPleX<sup>TM</sup> waveguides, developed by LioniX BV (Enschede, The Netherlands), by designing a similar Mach-Zehnder interferometer. TriPleX<sup>TM</sup> waveguides that we used have a low-index core ( $\text{SiO}_2$ ) which is encapsulated in a box shaped high-index ( $\text{Si}_3\text{N}_4$ ) layer. They have lower loss and dispersion compared to SOI waveguides, but require much larger bend radius. The interferometer chip consists of waveguides, four splitters and a 19 cm long reference arm. The footprint of the interferometer is 10 mm  $\times$  33 mm. The waveguides were designed to support only fundamental TE and TM modes. The coupling of the light in and out of the chip was done horizontally. To reduce the reflections at the waveguide ends, waveguides at both sides of the chip were angle polished. As splitters, we used symmetric y-splitters

which are wavelength independent and were provided as building blocks by LioniX BV. The interferometer was used as the core of a spectral-domain OCT (SD-OCT) system consisting of a superluminescent diode centered at 1320 nm with 100 nm bandwidth, a spectrometer with 1024 channels, and an x-y scanner. The  $TM_{00}$  mode of these waveguides has lower dispersion than the  $TE_{00}$  mode, thus the input light to the waveguides was adjusted to  $TM_{00}$  mode. The dispersion of the system, mainly caused by the on-chip reference arm, was numerically compensated in software. The dispersion parameters were found by using an iterative algorithm that maximizes the sharpness of the OCT images. After dispersion compensation, the axial resolution of the system was measured as 10  $\mu\text{m}$ . The sensitivity of the system was measured to be 65 dB with 100  $\mu\text{W}$  on the sample. The low sensitivity can be attributed to the horizontal coupling losses. Using the system, we imaged human finger skin *in vivo*. In the cross-sectional images that we obtained, different epidermal and dermal sub-layers of the skin could be seen. By using a set of cross-sectional images, we also obtained *en-face* (top view) images of the skin. In these images, we could also see the morphological variations of different skin layers.

For a complete on-chip SD-OCT system, it is necessary to have an integrated spectrometer. Spectrometers in SD-OCT systems have high resolution ( $\sim 0.15$  nm) and hundreds of channels ( $>512$ ). We explored a spectrometer architecture based on cascaded ring resonators and AWGs in SOI. The spectrometer consists of the 13 ring resonator - AWG pairs. In front of each AWG there is a ring resonator that acts as a pre-filter. A comb-like spectrum from each ring is sent to its corresponding AWG. The AWG channel spacings and ring resonator free-spectral ranges are matched and each AWG channel outputs a peak from the comb-like spectrum. In this architecture, the spectral resolution at the output channels, which is normally defined by the AWG, is determined by the resonance width of the rings. The ring resonators have 0.06 nm resonance width and consecutive rings are shifted by 0.15 nm from one another. Thus, the spectrometer have 0.15 nm channel spacing with 0.06 nm resolution. Each AWG has 16 channels which results in a spectrometer with a total of 208 ( $13 \times 16$ ) channels. However, due to fabrication related errors, it was necessary to adjust the peak positions of the ring resonators so that they coincide with the channels of the AWGs. To this aim, we deposited metal heaters on the ring resonator to thermally tune their spectral response.

## 6.2 Perspectives

We demonstrated OCT imaging using integrated interferometers fabricated in two different material systems. However, the sensitivities of the OCT systems with the integrated interferometers were relatively low compared to state-of-the-art OCT systems. For OCT systems it holds that the better the sensitivity, the deeper the imaging depth. In both designs, the reason for low sensitivity stems from the fiber-to-chip coupling losses. In the SOI interferometer, the axial resolution was also limited by the bandwidth of the grating couplers. An ideal solution to the fiber-to-chip coupling problem is to develop low-loss, broadband spot-size converters which can couple light from standard single-mode fibers (SMFs). Ben Bakir et al. demonstrated  $3\ \mu\text{m} \times 3\ \mu\text{m}$  spot size converters with  $>200\ \text{nm}$  bandwidth and 1 dB insertion loss [1]. Shiraishi et al. demonstrated a spot size converter with 2.8 dB coupling loss to a standard SMF [2]. Spot size converters to SMF have larger alignment tolerances compared to the ones to lensed fibers. Interfacing to SMF also enables the use of off-the-shelf fibers and fiber arrays and can reduce packaging costs.

Compared to SMFs, integrated photonic waveguides enable optical systems with very small footprint. Such miniaturization can also enable faster, parallel OCT systems. In general, integrated waveguides are more dispersive than SMFs. However, by changing the cross-sectional size and shape of the waveguides or the cladding material, dispersion can be tailored. Depending on the material system used for the waveguides, even close-to-zero group velocity dispersion can be obtained [3]. Besides, the dispersion in the long reference arm could be matched by using a short highly dispersive waveguide in the sample arm.

Even though the length of the waveguides in an integrated interferometer is quite small, minimizing the waveguide loss can improve the sensitivity by a few dBs. Another advantage of a low-loss waveguide is that there will be less sidewall roughness which may scatter the light back into the waveguide. Thanks to low scattering, low-loss waveguides can also be used to design Michelson interferometers. It could be useful to model the effect of scattering on the noise floor of the OCT signal. For SOI waveguides, the propagation loss can be reduced by defining the waveguides using selective oxidation rather than etching. Although this technique could be useful for waveguide definitions, it might not be suitable for the definition of components such as adiabatic splitters which have small critical dimensions. Using higher resolution lithogra-

phy reduces the side wall roughness and seems to be a viable solution for low-loss SOI waveguides [4].

Internal reflections within the interferometer may appear as a residual background in the OCT images, masking useful information. The return loss of fiber components, which are connected to each other with fibers much longer than the coherence length of the light source, may not present a significant problem. While, reflections within small components like lenses and splitters could be seen in the OCT images. Such background signals in the system could ideally be removed by background subtraction. However, due to light source power and phase fluctuations between each A-line, such signals could not be completely removed. The distances between individual components in a photonic integrated chip are in the order of the coherence length of OCT light sources. Thus, fringes resulting from reflections within the chip may appear as spurious background signals in the OCT signal. To avoid this, individual components should minimize internal reflections and the transitions between different photonic integrated components need to be sufficiently smooth.

The signal-to-noise ratio (SNR) of an OCT system can be optimized by using an unbalanced splitter to deliver different amounts of light to sample and reference arms [5]. Broadband splitters other than 50:50 splitting ratios can be investigated. Moreover, active tuning of the splitting ratio can be very useful. Some light sources may not have a built-in attenuator to adjust the amount of light coupled into the interferometer. A broadband integrated attenuator could also be valuable in such situations. A variable attenuator can also be used to adjust the power in the reference arm, since too much power in the reference arm may saturate the photodetectors and even decrease the SNR [6]. Another improvement to SNR can be achieved by developing an integrated optical circulator to be used in the sample arm. By using a circulator, all of the backscattered light from the sample can be interfered with the light in the reference arm [5].

In this thesis, we worked with two waveguide platforms: SOI and TriPleX<sup>TM</sup>. Selection of a waveguide platform for integrated OCT depends on many factors. One of them is the operating wavelength range. Both core and cladding materials need to be transparent in the spectrum of operation. Silicon is transparent from 1.1  $\mu\text{m}$  to 8  $\mu\text{m}$  wavelengths and is opaque in the visible range. On the other hand, a  $\text{SiO}_2$  buried oxide layer starts to absorb significantly at a wavelength of about 4  $\mu\text{m}$ , thereby limiting the operation range of SOI from 1.1  $\mu\text{m}$  to 4  $\mu\text{m}$  [7], [8].

$\text{Si}_3\text{N}_4$  is transparent over a wavelength range spanning the entire visible to mid IR wavelengths [9]. The waveguide loss does not only stem from absorption of the core and cladding materials but also from sidewall roughness, specifically in high-index-contrast waveguides.  $\text{Si}_3\text{N}_4$  waveguides deposited with low-pressure chemical vapor deposition exhibit low surface roughness. High-aspect-ratio core geometry  $\text{Si}_3\text{N}_4$  waveguides with 0.09 dB/cm loss have been demonstrated [10]. On the contrary, SOI waveguides with 0.45 dB/cm loss have been fabricated by using high resolution lithography [4]. Actually, the major loss in our studies was due to fiber-to-chip coupling losses. As we discussed in Chapters 3 and 4, tapering the mode of the waveguides to match the mode of the fibers is a feasible solution to this problem. OCT has always benefited from optical components for telecom applications. It is likely that the need for high-speed interconnects in data centers will push the industry to develop at least one integrated photonics platform which provides low-loss waveguides with low-loss fiber-to-chip coupling interfaces and easy integration with active components. Currently silicon seems to have good momentum towards such a platform; however, the interest in  $\text{Si}_3\text{N}_4$  is also growing.

For a complete on-chip OCT system, the integration of photodetectors and light sources with the passive structures is needed. In addition to advantages in size, stability and cost, integrating the photodetectors and light sources will also eliminate the related chip-to-fiber losses. Integration of passive structures with active components such as photodetectors, laser diodes and semiconductor optical amplifiers have been demonstrated following two different approaches: 1) Hybrid integration, where prefabricated devices are bonded on top of the passive structures [11]. 2) Heterogeneous integration, where active material epitaxial layers are bonded on top of the passive waveguides and then processed to realize active components [12]. It would probably be more practical to use the hybrid approach for the integration of semiconductor and MEMS light sources as their fabrication is quite complex for heterogeneous integration. On the other hand, the heterogeneous approach is more feasible for the integration of photodetectors and photodetector arrays as their fabrication is simpler compared to the fabrication of light sources. With further progress in semiconductor and MEMS swept-source lasers and improvement in integrated spectrometers, it would be possible to realize on-chip FD-OCT systems.

Clearly, on-chip systems can have a very small form factor. Fabricating such systems on wafer scale brings the possibility to significantly

reduce the price as well. One point that needs to be considered here is that in wafer-scale fabrication the factor of price reduction depends on production volume. According to a market research report by Tematys (Paris, France), OCT market for healthcare and life science sectors is expected to grow from €600 million in 2015 to around €1 billion in 2019 [13]. Assuming a €100,000 average price per OCT system, it means that 10,000 OCT systems per year will be sold in 2019. It is likely that this number is based on the projection of the current growth rate of the OCT market. However, a breakthrough, such as OCT-on-a-chip, can significantly change the number of OCTs sold per year. If the price drops to €10,000 price levels, even small hospitals, clinics and private practices can afford an OCT. With such price drop, OCT can also rapidly diffuse in other medical areas such as dermatology, endoscopy, pathology and dentistry. Additionally, OCT has also the potential to enable early detection of some diseases in primary care office settings. An on-chip-OCT can be integrated with a digital microscope in a hand-held scanner with interchangeable tips. Such device can provide real-time microscopic assessment of tissue sites commonly examined in primary care, including the ears, eyes, skin, oral mucosa, and teeth. Such device has the potential to be an efficient point-of-care imaging tool in primary care medicine.

We hope that the studies presented in this thesis can help other researchers to develop portable, low-cost OCT systems in the near future.



# References

- [1] B. Bakir *et al.*, “Low-loss ( $<1$  db) and polarization-insensitive edge fiber couplers fabricated on 200-mm silicon-on-insulator wafers”, *IEEE Photonics Technology Letters*, vol. 22, no. 11, pp. 739–741, 2010 (cit. on p. 132).
- [2] K. Shiraishi, H. Yoda, and C. S. Tsai, “A two-port polarization-insensitive coupler module between single-mode fiber and silicon-wire waveguide”, *Optics express*, vol. 20, no. 22, pp. 24 370–24 375, 2012 (cit. on p. 132).
- [3] A. C. Turner, C. Manolatou, B. S. Schmidt, M. Lipson, M. A. Foster, J. E. Sharping, and A. L. Gaeta, “Tailored anomalous group-velocity dispersion in silicon channel waveguides”, *Optics Express*, vol. 14, no. 10, pp. 4357–4362, 2006 (cit. on p. 132).
- [4] S. K. Selvaraja, P. De Heyn, G. Winroth, P. Ong, G. Lepage, C. Cailler, A. Rigny, K. Bourdelle, D. VanThourhout, J. Van Campenhout, *et al.*, “Highly uniform and low-loss passive silicon photonics devices using a 300mm cmos platform”, in *Optical Fiber Communication Conference*, Optical Society of America, 2014, Th2A–33 (cit. on pp. 133–134).
- [5] A. M. Rollins and J. A. Izatt, “Optimal interferometer designs for optical coherence tomography”, *Optics letters*, vol. 24, no. 21, pp. 1484–1486, 1999 (cit. on p. 133).
- [6] W. V. Sorin and D. M. Baney, “A simple intensity noise reduction technique for optical low-coherence reflectometry”, *Photonics Technology Letters, IEEE*, vol. 4, no. 12, pp. 1404–1406, 1992 (cit. on p. 133).
- [7] G. Z. Mashanovich, M. M. Milošević, M. Nedeljkovic, N. Owens, B. Xiong, E. J. Teo, and Y. Hu, “Low loss silicon waveguides for the mid-infrared”, *Optics Express*, vol. 19, no. 8, pp. 7112–7119, 2011 (cit. on p. 133).
- [8] G. Roelkens, U. Dave, A. Gassenq, N. Hattasan, C. Hu, B. Kuyken, F. Leo, A. Malik, M. Muneeb, E. Ryckeboer, *et al.*, “Silicon-based heterogeneous photonic integrated circuits for the mid-infrared”, *Optical Materials Express*, vol. 3, no. 9, pp. 1523–1536, 2013 (cit. on p. 133).
- [9] F. Morichetti, A. Melloni, M. Martinelli, R. G. Heideman, A. Leinse, D. H. Geuzebroek, and A. Borreman, “Box-shaped dielectric waveguides: a new concept in integrated optics?”, *Lightwave Technology, Journal of*, vol. 25, no. 9, pp. 2579–2589, 2007 (cit. on p. 134).

- 
- [10] J. F. Bauters, M. J. Heck, D. John, D. Dai, M.-C. Tien, J. S. Barton, A. Leinse, R. G. Heideman, D. J. Blumenthal, and J. E. Bowers, “Ultra-low-loss high-aspect-ratio  $\text{Si}_3\text{N}_4$  waveguides”, *Optics express*, vol. 19, no. 4, pp. 3163–3174, 2011 (cit. on p. 134).
- [11] S. Stankovic, R. Jones, M. N. Sysak, J. M. Heck, G. Roelkens, and D. Van Thourhout, “Hybrid  $\text{III-V/Si}$  distributed-feedback laser based on adhesive bonding”, *Photonics Technology Letters, IEEE*, vol. 24, no. 23, pp. 2155–2158, 2012 (cit. on p. 134).
- [12] M. Piels, J. F. Bauters, M. L. Davenport, M. J. Heck, and J. E. Bowers, “Low-loss silicon nitride awg demultiplexer heterogeneously integrated with hybrid  $\text{III-V/Si}$  photodetectors”, *Lightwave Technology, Journal of*, vol. 32, no. 4, pp. 817–823, 2014 (cit. on p. 134).
- [13] Tematys, 2015, <http://tematys.fr/Publications/en> (cit. on p. 135).

# A

## Effect of dispersion in OCT

Below we derive in detail the formulas given in Chapter 2, for broadening and amplitude degradation of the OCT point spread function due to dispersion mismatch. We begin by writing the interference of light coming from sample and reference arms.

$$\begin{aligned} S(\omega) &= |r_S E_0(\omega) \exp [i k_S(\omega) z_S] + r_R E_0(\omega) \exp [i k_R(\omega) z_R]|^2 \\ &= r_S^2 |E_0(\omega)|^2 + r_R^2 |E_0(\omega)|^2 + 2 r_S r_R |E_0(\omega)|^2 \cos [k_S(\omega) z_S - k_R(\omega) z_R] \\ &= r_S^2 |E_0(\omega)|^2 + r_R^2 |E_0(\omega)|^2 + 2 r_S r_R |E_0(\omega)|^2 \cos [\Delta \Phi(\omega)] \\ &= r_S^2 S_0(\omega) + r_R^2 S_0(\omega) + 2 r_S r_R S_0(\omega) \cos [\Delta \Phi(\omega)] \end{aligned} \tag{A.1}$$

In OCT, the phase mismatch between the reference and sample arms is

$$\Delta \Phi(\omega) = k_S(\omega) z_S - k_R(\omega) z_R \tag{A.2}$$

we can expand the propagation constants in Taylor series as

$$\begin{aligned} \Delta\Phi(\omega) = & \left[ k_S(\omega_0) + k'_S(\omega - \omega_0) + \frac{1}{2}k''_S(\omega - \omega_0)^2 \right] z_S \\ & - \left[ k_R(\omega_0) + k'_R(\omega - \omega_0) + \frac{1}{2}k''_R(\omega - \omega_0)^2 \right] z_R \end{aligned} \quad (\text{A.3})$$

if we write  $k_S$  and  $k_R$  as  $k_S = n_S \frac{\omega}{c}$  and  $k_R = n_R \frac{\omega}{c}$  we obtain

$$\begin{aligned} \Delta\Phi(\omega) = & \left[ n_S \frac{\omega_0}{c} + \frac{n_{gS}}{c}(\omega - \omega_0) + \frac{1}{2}k''_S(\omega - \omega_0)^2 \right] z_S \\ & - \left[ n_R \frac{\omega_0}{c} + \frac{n_{gR}}{c}(\omega - \omega_0) + \frac{1}{2}k''_R(\omega - \omega_0)^2 \right] z_R \end{aligned} \quad (\text{A.4})$$

after ordering the common terms,  $\Delta\Phi(\omega)$  can be expressed as

$$\begin{aligned} \Delta\Phi(\omega) = & (n_S z_S - n_R z_R) \frac{\omega_0}{c} + (n_{gS} z_S - n_{gR} z_R) \frac{(\omega - \omega_0)}{c} \\ & + (k''_S z_S - k''_R z_R) \frac{(\omega - \omega_0)^2}{2} \end{aligned} \quad (\text{A.5})$$

If we define path length differences as

$$\begin{aligned} \Delta z_p &= n_S z_S - n_R z_R \\ \Delta z_g &= n_{gS} z_S - n_{gR} z_R \\ \Delta k'' &= k''_S z_S - k''_R z_R \end{aligned}$$

where the subscript  $p$  denotes phase and the subscript  $g$  denotes group. Then, we can write  $\Delta\Phi(\omega)$  as

$$\Delta\Phi(\omega) = \Delta z_p \frac{\omega_0}{c} + \Delta z_g \frac{(\omega - \omega_0)}{c} + \Delta k'' \frac{(\omega - \omega_0)^2}{2} \quad (\text{A.6})$$

Let the spectrum of the light source be Gaussian as

$$S_0(\omega) = \exp \left[ \frac{-(\omega - \omega_0)^2}{2\sigma_\omega^2} \right] \quad (\text{A.7})$$

To obtain the depth-resolved reflectivity profile we need to Fourier transform the interference term  $I(\omega) = S_0(\omega) \exp[i\Delta\Phi(\omega)]$ , given at the

end of Eq. (A.1).

$$F \{I(\omega)\} (z) = \int_{-\infty}^{-\infty} S_0(\omega) \exp [i\Delta\Phi(\omega)] \exp(-ikz) dk \quad (\text{A.8})$$

after substituting  $\Delta\Phi(\omega)$  from Eq. (A.6) in Eq. (A.8) and writing  $k$  in terms of  $\omega$ , we obtain

$$F \{I(\omega)\} (z) = \exp \left( i \frac{\omega_0}{c} \Delta z_p \right) \int_{-\infty}^{-\infty} S_0(\omega) \exp \left( i \left[ \frac{\Delta z_g}{c} (\omega - \omega_0) + \frac{\Delta k''}{2} (\omega - \omega_0)^2 \right] \right) \exp \left( -i \frac{\omega}{c} z \right) d \left( \frac{\omega}{c} \right) \quad (\text{A.9})$$

after change of variables by  $\Omega = (\omega - \omega_0)/c$ ,  $d\Omega = d\omega/c$  we can express the integral as

$$F \{I(\omega)\} (z) = \exp(ik_0 \Delta z_p) \int_{-\infty}^{-\infty} \exp \left( \frac{-c^2}{2\sigma_\omega^2} \Omega^2 \right) \exp \left( i \left[ \Delta z_g \Omega + \frac{c^2 \Delta k''}{2} \Omega^2 \right] \right) \exp \left( -i\Omega z - i \frac{\omega_0}{c} z \right) d\Omega \quad (\text{A.10})$$

We can evaluate this integral using Siegman's Lemma:

$$\int_{-\infty}^{+\infty} e^{-Ay^2 - 2By} dy = \sqrt{\frac{\pi}{A}} e^{B^2/A}, \text{Re}[A] > 0 \quad (\text{A.11})$$

after ordering the terms in the integral to make it similar to the terms in Siegman's Lemma, we obtain

$$F \{I(\omega)\} (z) = \exp(ik_0 \Delta z_p - ik_0 z) \int_{-\infty}^{-\infty} \exp \left( - \left[ \frac{c^2}{2\sigma_\omega^2} - i \frac{\Delta k'' c^2}{2} \right] \Omega^2 - 2 \left[ i \frac{z - \Delta z_g}{2} \right] \Omega \right) d\Omega \quad (\text{A.12})$$

To use Siegman's Lemma, let's define two terms,  $A$  and  $B$  as

$$A \equiv \frac{c^2}{2\sigma_\omega^2} - i\frac{\Delta k'' c^2}{2} \quad (\text{A.13})$$

$$B \equiv i\frac{z - \Delta z_g}{2} \quad (\text{A.14})$$

and finally, the integration yields the following expression

$$F\{I(\omega)\}(z) = \exp(ik_0\Delta z_p - ik_0z) \sqrt{\frac{\pi}{A}} \exp\left(-\frac{(z - \Delta z_g)^2}{4A}\right) \quad (\text{A.15})$$

We can express  $\frac{1}{4A}$ , the denominator of the exponential term in Eq. (A.15), explicitly as

$$\begin{aligned} \frac{1}{4A} &= \frac{1}{4\left(\frac{c^2}{2\sigma_\omega^2} - i\frac{\Delta k'' c^2}{2}\right)} \\ &= \frac{\sigma_\omega^2}{2c^2(1 - i\Delta k'' \sigma_\omega^2)} \\ &= \frac{\sigma_\omega^2}{2c^2} \left[ \frac{1}{1 + (\Delta k'' \sigma_\omega^2)^2} + i\frac{\Delta k'' \sigma_\omega^2}{1 + (\Delta k'' \sigma_\omega^2)^2} \right] \end{aligned} \quad (\text{A.16})$$

From here, we can deduce the standard deviation of axial width in  $z$ ,  $\sigma_z$

$$\frac{1}{2\sigma_z^2} = \frac{\sigma_\omega^2}{2c^2} \frac{1}{1 + (\Delta k'' \sigma_\omega^2)^2} \quad (\text{A.17})$$

$$\sigma_z = \frac{c\sqrt{1 + (\Delta k'' \sigma_\omega^2)^2}}{\sigma_\omega} \quad (\text{A.18})$$

Thus, the axial resolution is broadened by a factor of

$$\sqrt{1 + (\Delta k'' \sigma_\omega^2)^2} \quad (\text{A.19})$$

The amplitude of the pulse is decreased due to dispersion. We can express  $|\sqrt{\frac{\pi}{A}}|$ , the magnitude of the multiplicative term in front of the exponential term in Eq. (A.15), explicitly as

$$\begin{aligned}
\left| \sqrt{\frac{\pi}{A}} \right| &= \frac{\sqrt{\pi}}{\sqrt{|A|}} = \sqrt{\pi} \frac{1}{\left[ \left( \frac{c^2}{2\sigma_\omega^2} \right)^2 + \left( \frac{\Delta k'' c^2}{2} \right)^2 \right]^{1/4}} \\
&= \sqrt{\pi} \frac{1}{\left[ \frac{c^4}{4\sigma_\omega^4} \left( 1 + (\Delta k'' \sigma_\omega^2)^2 \right) \right]^{1/4}} \quad (\text{A.20}) \\
&= \frac{\sqrt{2\pi}\sigma_\omega}{c} \frac{1}{\left[ 1 + (\Delta k'' \sigma_\omega^2)^2 \right]^{1/4}}
\end{aligned}$$

Thus, the degradation of the amplitude is the following multiplicative factor

$$\frac{1}{\left[ 1 + (\Delta k'' \sigma_\omega^2)^2 \right]^{1/4}} \quad (\text{A.21})$$



# B

## Matlab code for cross-sectional image generation from SS-OCT data

Below we provide two matlab scripts used in Chapter 3. The first script finds dispersion parameters using reflection measurement from a mirror in the sample arm. The second script uses the dispersion parameters from the first script and generates a cross-sectional image (B-scan).

---

```
1 % findDispersionParameters.m
2 % Description:
3 % The program finds the polynomial coefficients for a
4 % polynomial fit to the phase of fringe data. The fringe
5 % data (A-lines) is obtained by measuring reflection from a
6 % mirror placed in the sample arm.
7 % Summary:
8 % 1. Initialize parameters
9 % 2. Read A-line and background data from files
10 % 3. Substract background
11 % 4. Find the phase using Hilbert transform
12 % 5. Fit a polynomial to the phase
13 %
14 % Authors: Gunay Yurtsever and Nicolas Weiss - 2014
```

```

15
16 clear all
17 close all;
18 %%%%%%%%%%%%%%%%%%%%%%%%%%%%%%%%%%%%%%%%%%%%%%%%%%%%%%%%%%%%%%%%%%%%%%%%%
19 %% Initialize parameters
20
21 polynomialOrder = 3; % polynomial order for fitting the phase
22
23 SamplesPerAline = 544*2; % each A-line has 1088 data points
24 AlinesPerBscan = 1000; % number of A-lines in the file
25
26 % directory path, where the data is stored
27 pathname = 'C:\OCTdata\Aline\';
28 cd(pathname);
29
30 % A-line file for reflection from a mirror in the sample arm
31 filename_Alines = 'aline1500um.dat';
32 fname_Aline = strcat(pathname, filename_Alines);
33
34 % background file for A-line with a mirror in the sample arm
35 filename_bgnd = 'aline1500um-b.dat';
36 fname_bgnd = strcat(pathname, filename_bgnd)
37
38 %%%%%%%%%%%%%%%%%%%%%%%%%%%%%%%%%%%%%%%%%%%%%%%%%%%%%%%%%%%%%%%%%%%%%%%%%
39 %% Read A-line and background data from files
40
41 % open and read data file containing the A-lines
42 fid = fopen(filename_Alines); %open binary file
43 Alines = fread(fid, [SamplesPerAline,AlinesPerBscan], ...
44     'uint16=>uint16','b'); %read binary file
45 fclose(fid); %close binary file
46 Alines = double(Alines); % convert uint16 formatted data to dou
47
48 % open and read background file
49 fid = fopen(fname_bgnd); % open binary file
50 bgnd = fread(fid, [SamplesPerAline,AlinesPerBscan], ...
51     'uint16=>uint16','b'); %read binary file
52 fclose(fid); % close binary file
53 bgnd = double(bgnd); % convert uint16 formatted data to double
54
55 %%%%%%%%%%%%%%%%%%%%%%%%%%%%%%%%%%%%%%%%%%%%%%%%%%%%%%%%%%%%%%%%%%%%%%%%%
56 %% Subtract background
57
58 avg_bgnd = mean(bgnd,2); % average background
59 Alines = Alines - avg_bgnd(:,ones(1,size(Alines,2)));
60
61 [row, col] = size(Alines);
62 xAxis = 1:row; % x-axis is the indices of the samples points
63

```

---

```
62 %%%%%%%%%%%%%%%%%%%%%%%%%%%%%%%%%%%%%%%%%%%%%%%%%%%%%%%%%%%%%%%%%%%%%%%%%%
63 %% Find the phase using Hilbert transform
64
65 % remove the mean value from each column of the matrix. It is
66 % necessary before Hilbert transform
67 Alines = detrend(Alines, 'constant');
68 Ah = hilbert(Alines); % Hilbert transform
69 phaseA = unwrap(angle(Ah));
70 figure;
71 plot(xAxis, phaseA); hold on;
72 xlabel('sample points'); ylabel('phase (radians)');
73
74 %%%%%%%%%%%%%%%%%%%%%%%%%%%%%%%%%%%%%%%%%%%%%%%%%%%%%%%%%%%%%%%%%%%%%%%%%%
75 %% Fit a polynomial to the phase
76
77 dataRange = 100:750; % data range with good SNR
78 phase_avg = mean(phaseA(dataRange, :), 2);
79 plot(xAxis(dataRange), phase_avg, '-b', 'LineWidth', 2)
80
81 n = length(phase_avg); % number samples points
82 w = linspace(-n/2, n/2, n)'; % frequency axis is centered ...
    around zero. Centering improves the numerical ...
    properties of the fitting algorithm.
83
84 p = polyfit(w, phase_avg, polynomialOrder); % polynomial fit ...
    to the average phase. p(x) = p(1)*x^n + p(2)*x^{n-1} + ...
    .... + p(n+1)*x + p(n+1)
85
86 % save the polynomial coefficients
87 fid = fopen('dispersion_coefficients.txt', 'w');
88 fprintf(fid, '%1.6e\r\n', p);
89 fid = fclose(fid);
90
91 % evaluate and plot the polynomial
92 polynomialFit = polyval(p, w);
93 h1 = plot(xAxis(dataRange), polynomialFit, '-r', 'LineWidth', 2);
94 legend(h1, 'polynomial fit');
```

---

---

```

1  %               createCrossSectionalImage.m
2  % Description:
3  % This program makes a cross-sectional image(B-scan) from raw
4  % SS-OCT data acquired at Amsterdam Medical Center.
5  % Summary:
6  % 1. Initialize parameters
7  % 2. Read B-scan and background data from files
8  % 3. Compensate dispersion
9  % 4. Fourier transform and subtract background
10 % 5. Create cross-sectional image
11 %
12 % Authors: Gunay Yurtsever and Nicolas Weiss - 2014
13
14 clear all
15 close all;
16 %%%%%%%%%%%%%%%%%%%%%%%%%%%%%%%%%%%%%%%%%%%%%%%%%%%%%%%%%%%%%%%%%%%%%%%%%
17 %% Initialize parameters
18
19 % polynomial coefficients for dispersion compensation, obtained
20 % using findDispersionParameters.m
21 p = [6.728834e-008 1.067473e-003 6.529707e-001 1.135437e+002];
22
23 SamplesPerAline = 544*2; % related to the data acquisition card
24 AlinesPerBscan = 5e4; % number of A-lines in a B-scan
25
26 % directory path to where the data is stored
27 pathname = 'C:\OCTdata\Bscan\';
28 cd(pathname);
29
30 % B-scan (cross-sectional image) data file
31 filename_Bscan = 'DucPhantom-2000-4200-3-e5.dat';
32 fname_Bscan = strcat(pathname,filename_Bscan);
33
34 % background file for B-scan without the sample
35 filename_bgnd = 'DucPhantom-2000-4200-3-e5-bgnd.dat';
36 fname_bgnd = strcat(pathname,filename_bgnd);
37
38 %%%%%%%%%%%%%%%%%%%%%%%%%%%%%%%%%%%%%%%%%%%%%%%%%%%%%%%%%%%%%%%%%%%%%%%%%
39 %% Read B-scan and background data from files
40
41 % open and read data file
42 fid = fopen(fname_Bscan); % open binary file
43 B = fread(fid, [SamplesPerAline,AlinesPerBscan], ...
44           'uint16=>uint16','b'); % read binary file
44 fclose(fid); % close binary file
45 B = double(B); % convert uint16 formatted data to double
46
47 % open and read background file
48 fid = fopen(fname_bgnd); %open binary file

```

---

```

49 bgnd = fread(fid, [SamplesPerAline,AlinesPerBscan], ...
    'uint16=>uint16','b'); % read binary file
50 fclose(fid); % close binary file
51 bgnd = double(bgnd); % convert uint16 formatted data to double
52
53 %%%%%%%%%%%%%%%%%%%%%%%%%%%%%%%%%%%%%%%%%%%%%%%%%%%%%%%%%%%%%%%%%%%%%%%%%
54 %% Compensate dispersion
55
56 po = length(p)-1; % polynomial order
57 newDataRange = [1:850]'; % data from 850:end is very noisy.
58 n = length(newDataRange);
59 w = linspace(-n/2,n/2,n)'; % frequency vector
60
61 % initialize the nonlinear phase vector
62 nonlinearPhase = zeros(size(newDataRange));
63
64 %construct the nonlinear phase from the polynomial coefficients
65 for i = 1:po-1
66     nonlinearPhase = nonlinearPhase + p(i)*w.^(po+1-i);
67 end
68
69 nonlinearPhaseExp = exp(-1i*nonlinearPhase);
70 nColumn = size(B,2); % number of columns in matrix B
71 % create a matrix by replicating the nonlinearPhaseExp ...
    vector nColumn times
72 dispersionCorrectionMatrix=nonlinearPhaseExp(:,ones(1,nColumn));
73
74 % multiply the data and the background with the dispersion ...
    correction matrix
75 B = hilbert(B(newDataRange,:)).* dispersionCorrectionMatrix;
76 bgnd =hilbert(bgnd(newDataRange,:)).*dispersionCorrectionMatrix;
77
78 %%%%%%%%%%%%%%%%%%%%%%%%%%%%%%%%%%%%%%%%%%%%%%%%%%%%%%%%%%%%%%%%%%%%%%%%%
79 %% Fourier transform and subtract background
80
81 BF = abs(fft(B,1088));
82 [row,col] = size(BF);
83 BF = BF(1:row/2,:);
84
85 bgndF = abs(fft(bgnd,1088));
86 bgndF = bgndF(1:row/2,:);
87 Bavg = mean(bgndF,2);
88
89 BF = BF - Bavg(:,ones(1,col)); % subtract background
90
91 %%%%%%%%%%%%%%%%%%%%%%%%%%%%%%%%%%%%%%%%%%%%%%%%%%%%%%%%%%%%%%%%%%%%%%%%%
92 %% Create cross-sectional image
93
94 % create a 3D matrix form the 2D matrix containing all B-scans

```

---

```

95 Bscans = reshape(BF,544,1000,AlinesPerBscan/1000);
96 Bimage = mean(Bscans,3); % average all B-scans
97
98 % scale image data
99 Bimage = Bimage/max(max(Bimage)); % normalize the B-scan
100
101 % set all values smaller than lowThreshold to lowThreshold
102 lowThreshold = 0.01;
103 Bimage(Bimage < lowThreshold) = lowThreshold;
104 Bimage = Bimage - min(min(Bimage)) + 1/256; % add a small
105 % term such as 1/256, so that we do not have a zero term.
106 % Because, next we will take its log
107 % display image in log scale to see small signals
108 Bimage = 20*log10(Bimage);
109 % map image data to a range of 0 - 256 (2^8)
110 bits = 8;
111 Bimage =2^bits*( Bimage-min(min(Bimage)) ) / ( ...
      max(max(Bimage)) - min(min(Bimage)) );
112
113 % ignore the data between columns 479-528 and swap 528:end
114 % and 1:479 data ranges. This is due to a synchronization bug
115 % in the data acquisition software
116 Bimage = [Bimage(:,528:end) Bimage(:,1:479)];
117
118 % create x,y coordinates
119 [row,col] = size(Bimage);
120 % A-lines are 1.7 micron away from each other.
121 x = linspace(0,1.7*col,col);
122 y = linspace(0,5087,row); % max depth is 5087 micron
123
124 % display image and set labels
125 figure;
126 imagesc(x,y,Bimage)
127 colormap('gray');
128
129 set(gca,'FontName','Arial')
130 set(gca,'FontSize',10)
131 set(gca,'linewidth',2)
132 set(gca,'FontName','Arial')
133 xlabel('Lateral distance (\mum)','FontName','Arial')
134 ylabel('Optical path length (\mum)','FontName','Arial')
135
136 % save image
137 imwrite(Bimage,[filename_Bscan(1:end-4) '.png'],'png');

```

---



